# A Microfluidic Platform for Combinatorial Experiments

by

## Anthony Benjamin Kulesa

B.S. Biomedical Engineering
Rutgers University 2012

Submitted to the Department of Biological Engineering
in partial fulfillment of the requirements for the degree of

Doctor of Philosophy in Biological Engineering

at the

MASSACHUSETTS INSTITUTE OF TECHNOLOGY

September 2018

**Signature redacted**

Signature of Author...........................................    ....
Department of Biological Engineering
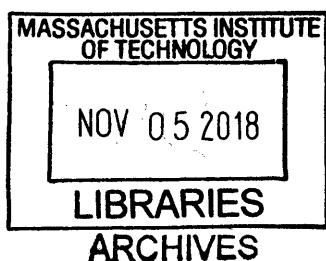July 16, 2018

**Signature redacted**

Certified by.........................................
Paul C. Blainey
Associate Professor of Biological Engineering
Thesis Supervisor

**Signature redacted**

Accepted by.................................
Forest White
Professor of Biological Engineering
Chair of Graduate Program, Department of Biological Engineering

# Thesis committee members

Mark Bathe, Ph.D. (Chair)
Associate Professor of Biological Engineering
Massachusetts Institute of Technology

Jeff Gore, Ph.D.
Associate Professor of Physics
Massachusetts Institute of Technology

Angela Koehler, Ph.D.
Assistant Professor of Biological Engineering
Massachusetts Institute of Technology

# A Microfluidic Platform for Combinatorial Experiments

by

# Anthony Benjamin Kulesa

Submitted to the Department of Biological Engineering
on August 10, 2018 in partial fulfillment of the
requirements for the degree of
Doctor of Philosophy in Biological Engineering

# Abstract

Experiments in biology are often combinatorial in nature and require analysis of large multi-dimensional spaces, but the scales of these experiments are limited by logistical complexity, cost, and reagent consumption. By miniaturizing experiments across nanoliter-scale emulsions that can be processed at large scales, droplet microfluidic platforms are poised to attack these challenges.

Here we describe a droplet microfluidic platform for combinatorial experiments that automates the assembly of reagent combinations, with order-of-magnitude improvements over conventional liquid handling. Moreover, our design is accessible, requiring only standard lab equipment such as micropipettes, and improves the chemical compatibility of droplet microfluidic platforms for small molecules.

We applied our platform to two experimental problems: combinatorial drug screening and microbial ecology. First, we used our platform to enable screening of pairwise combinations of a panel of antibiotics and 4,000+ investigational and approved drugs to overcome intrinsic antibiotic resistance in the model Gram-negative bacterial pathogen *E. coli*. This screen processed 4+ million droplet-level assays by hand in just 10 days to discover more than 10 combinations of antibiotics and non-antibiotic drugs for further study.

We then applied our platform to microbial ecology, where the interactions between microbes in communities can dictate functions important for both basic science and biotechnology. As a proof of concept, we used our platform to survey 960 pairwise interactions of microbes isolated from soil, and deconstruct higher-order interactions in a 4-strain community.

Altogether, we expect that our platform can be used to efficiently attack combinatorial problems across molecular and cellular biology.

Thesis Supervisor: Paul C. Blainey
Title: Associate Professor of Biological Engineering

# Acknowledgments

This experience has been a time of remarkable growth cultivated by many friends and mentors.

None of this would have been possible without my wife, Amy. Her personal strength shouldered me through countless scientific and personal failures for which we always found a path forward, and she was always first – as in, before me – to celebrate my successes. I am also enormously grateful to my family. My parents and grandparents encouraged my love of science and engineering from an early age, and I merely follow their examples of hard work and intellectual curiosity. In particular, I was always inspired by my grandfather's boundless curiosity about the nature of consciousness, and the origins of life and the universe.

I owe many thanks to the Blainey Lab community. Paul Blainey is unparalleled in his optimism, cooperative spirit, and willingness to challenge assumptions and orthodoxy, all traits that I hope I channel in my future work. He also empowered me to discover my own research directions, collaborators, and working style, to learn from failure, and to be confident in success. The Blainey Lab community was an eclectic mix of personalities, all of whom I thank for their friendship and mentorship. I was incredibly lucky to work with Jared Kehe, and I was inspired daily by his enthusiasm, meticulous project organization, and engineering talent. David Feldman and Nav Ranu got me on my feet in the lab. Nav blazed a trail in microbiology and microfluidics that he patiently helped me follow. David's intellectual force, constant re-invention, and push for excellence greatly shaped our work. Soohong Kim generously taught me many skills that became essential throughout my experience, and guided me scientifically early on. Jacob Borrajo brought stunning creativity to every project, both in the weeds of problem solving and in big picture directions. Georgia Lagoudas helped me navigate strategically through science and life. Lily Xu inspired us all with her fearlessness. Hudy Brody and Ankur Kulshreshtha brightened the lab with their optimism and curiosity. Francis McCarthy stabilized our community, and we are all greatly indebted to him for his leadership. I profoundly thank my undergraduate students Juan Hurtado, Prianca Tawde, Jameson Kief, and Allen Lee; and to my collaborators Jonathan Friedman and Anthony Ortiz. Last, I thank the new members of our lab, especially Avtar Singh and Cheri Ackerman, who I have learned greatly from already.

I found an incredible mix of scientific mentors throughout the extended MIT community. Since my first few weeks at MIT, Mark Bathe went above and beyond to help guide me, generously providing research ideas, project management tools, and personal advice. Angela Koehler patiently taught me about chemical biology, drug discovery, and translation, and always left me encouraged and excited. Jeff Gore inspired new directions of our work presented in Chapter 4, and generously opened his lab to us to pursue them. Moreover, Jeff spearheaded efforts to build the incredible biophysics community at MIT, where I found many friends and opportunities. I have been very lucky to have Mark, Angela, and Jeff as my thesis committee. I am also grateful to Jeremy Gunawardena, Pankaj Mehta, Wally Mangel, Stew Fisher, AJ Campbell, and Jonathan Friedman, all who generously engaged me scientifically and philosophically throughout the past six years.

Outside the lab, I am also greatly indebted to friends and mentors that gave me the tools to succeed both personally and professionally. Jaime Goldstein taught me how to manage people and projects, how to craft and execute high-level strategies, and how to communicate. Lori Pressman helped me see clearly, and not to follow the herd. Alex K. Chen introduced me to a great number of diverse people across all areas of science and technology. Together, Jaime, Lori, and Alex helped me find new paths through life that I would have never discovered otherwise. I also made many friends along the way that I wish to thank: MIT Biotech Group, Synapse, the BE Comm Lab, the Biophysics GSC, and the BiomedStartup team, the Biomakerspace team and MIT BioMakers, the BE-2012 cohort, and many collaborators.

I am deeply grateful to my funding sources, the NSF Graduate Research Fellowship Program, and Eran Broshy and the IMES Broshy Fellowship, and the MIT Deshpande Center, for giving me the opportunities to pursue this work.

Last, thank you to George Sun, Jared Kehe, and Manu Kumar for commenting on drafts of this thesis.

# Contents

# Chapter 1

# Introduction

## 1.1 The development of biology follows the invention of new interfaces to measure and manipulate biological systems

Scientific progress is gated by our ability to measure and manipulate the world around us. "Measure" because progress relies on our ability to observe new phenomena, and see where our models no longer match reality. "Manipulate" because we push systems outside of the regimes where models were constructed to generate new phenomena and recognize new patterns. Sets of technologies that join these capacities are an "interface": the point where two systems meet and interact; the first system being us, and the second, being the physical world. New techniques and technologies add new interfaces between us and physical systems. Put simply by a quote attributed to the biologist Sydney Brenner, "progress in science depends on new techniques, new discoveries and new ideas, probably in that order" [1].

This suggests a lens through which we can view the history of modern biology. Humanity's first interface to biological systems were merely the unaided human eyes (detailed anatomical observations of the diverse life populating Earth) and hands (selective breeding of plants and animals). Perhaps amazingly, with these tools alone we developed the theories of evolution by natural selection [2], and Mendelian inheritance of traits [3].

As the tools of analytical and physical chemistry matured in the 19th and 20th centuries, we gained new interfaces with biological systems. The principle discoveries that spawned the fields of biochemistry and molecular biology stemmed from new chemical methods for labeling (measurement) and purifying (manipulation) the molecular components of biology. For example, separating cytoplasm from cells distinguished enzymatic activity as a chemical property independent from life itself [4]. Chemical

techniques to further fractionate cytoplasm and purify its components finally assigned this activity to specific proteins [5]. Coupled with the development of radio-isotope labeling, these purification techniques ultimately provided the tools used by the famous Hershey-Chase experiment to demonstrate DNA as the hereditary material [6]. New means of measurement afforded by x-ray crystallography brought the discovery of the structure of DNA and the molecular basis of genetics [7]. Finally, the maturing of molecular biology as a science created powerful new interfaces to biological systems, built on the ability to sequence, synthesize, and recombine DNA, RNA, or protein that can be purified from or inserted into cells and organisms.

Today's understanding of biological systems considers the hierarchical multiscale nature of their components, perhaps ranging more than 10 orders of magnitude in length scale (Figure 1-1). To create means of measurement and manipulation that span this whole spectrum, we leverage the convergence of physics, chemistry, and biology (Figure 1-1). Below the nanoscale ($< 10^{-9}$ m) are the "small molecule" chemical components, and our interface is naturally composed of tools from physics and chemistry (measurement: structure determination by nuclear magnetic resonance, analysis by mass spectrometry; manipulation: synthetic chemistry and enzymatic biochemistry). These tools have broadly enabled the mapping of the chemistry of biological systems, such as metabolic pathways.
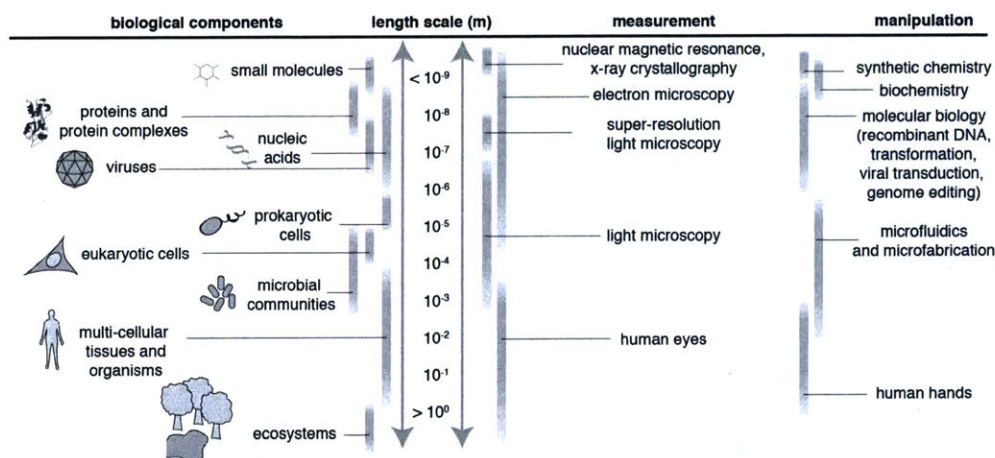


**Figure 1-1. Examples of biological system components and corresponding interfaces.** Note that length scales given here are not exact, and the lists of components and means to measure and manipulate them are not exhaustive.

Most biomolecules, such as proteins and nucleic acids, exist at the nanoscale ($10^{-9}$ – $10^{-8}$ m), where we leverage the convergence of these chemical methods with molecular biology. For example, the field of chemical genetics develops tools to make targeted, reversible, and temporally precise chemical changes to proteins — such as inhibition or activation — to investigate their function. Chemical methods also enabled the direct synthesis of bio-polymers such as peptides and nucleic acids. The tools of molecular biology give us the means to recombine these polymers and insert them into cells and organisms to code new genetic instructions.

However, many of the components of biological systems lie well above these length scales, such as prokaryotic cells ($\sim10^{-6}$ m), eukaryotic cells ($\sim10^{-5}$ m), microbial communities ($\sim10^{-4}$ m), and multicellular tissues ($\sim10^{-2}$ m), requiring an interface of a different nature. These components all exist in fluids, and technologies that precisely control fluids on these length scales ($10^{-6}$-$10^{-2}$ m) provide a generalizable interface to manipulate them. Together these technologies have become known as "microfluidics." The development of this interface has only taken place in the past few decades, but already microfluidic technologies have been used across a wide span of applications to achieve microscale control of temperatures [8], chemicals [9], cells [10], [11], and even tissues [8], [12], and the impacts across the field of biology are only just beginning.

# 1.2 Microfluidic platforms provide an interface to length scales important for molecular and cellular biology

## 1.2.1 Microfluidic platforms manipulate biology at the microscale

To provide an interface to molecular and cellular biology, microfluidic platforms need to *(i)* control fluids on the relevant length scales of $\sim10^{-6}$-$10^{-2}$ m; *(ii)* be biocompatible; and *(iii)* permit a means of measurement at the relevant length scales (for example, light microscopy). Microfluidic platforms quickly proliferated following the introduction of poly(dimethylsiloxane) (PDMS) as the basic material and a suite of relatively

fast (< 1 week) and easy lithographic microfabrication methods to construct features at the ~$10^{-6}$-$10^{-2}$ m length scales [13], [14]. PDMS is also largely bio-compatible and supports culture of a wide range of organisms and cell lines. Light microscopy is easily integrated with these devices as a means of measurement, as PDMS is optically transparent.

Simple microfluidic platforms composed of a single layer of fluid channels can leverage the physics of fluids at these length scales to provide many useful ways to interact with biological systems. The predictable laminar flow profiles and diffusive mixing make it simple to manipulate chemical or temperature gradients [15]. For example, Luchetta and colleagues probed the robustness of *Drosophila melanogaster* development by locally heating embryos based on their placement in two converging aqueous streams of different temperatures [8]. Chemical gradients can also be used to study chemotaxis [9], for example how *E. coli* tracks carbon sources based on fold-change gradients rather than changes in absolute levels [16]. Laminar flow profiles also allow for precise application of forces from fluid shear stress, such as to extend DNA polymers along a surface to allow the imaging of protein-DNA interactions [17].

Other forms of spatial control of biology are afforded by the ability of lithographic microfabrication methods to chemically and geometrically pattern surfaces on micrometer length scales. A technique called microcontact printing creates a microfabricated PDMS pattern that can be "inked" with a reactive chemical and "stamped" onto a surface. Using this technique, Chen and colleagues showed that cells can be triggered to both grow or activate apoptosis based on their shape by patterning cell adhesion proteins in progressively smaller areas [10], [11]. Geometric patterning of PDMS can also be used to create microchannels and microwells to easily capture and isolate single cells [18]. Due to its simplicity and generality, this technique has been used in a wide variety of applications including following *E. coli* divisions for 200 generations [19], or capturing mRNA from single-cells to obtain single-cell gene expression profiles [20], [21].

Microfluidic platforms have also translated many conventional methods in biology to the microscale, with the enhanced abilities to manipulate sample volumes down to single cells and molecules, reduce reagent consumption, and automate processing. This translation was catalyzed by the introduction of monolithic microfabricated valves and multi-layer soft lithography [22]. These valves can be used in a variety of architectures to create peristaltic pumps for mixing reagents, filters for separations, and multiplexed input/output control of reagents [23]. Microfluidic devices have now been developed to miniaturize and automate processing for a plethora of applications, including protein crystallography [24], multiplexed

10

polymerase chain reactions (PCR) [25], extraction of DNA and RNA from single cells [26], and sample processing for next-generation sequencing [27].

## 1.2.2 Droplet microfluidic platforms enable high throughput biological experiments across microscale fluidic compartments

By miniaturizing biological experiments into microscale compartments and automating fluid handling, microfluidic platforms also promised gains in throughput by processing samples simultaneously and integrating multiple assays [28]. Further improving throughput can be achieved by adding more and more miniature compartments, but a different strategy is provided by microfluidics for multi-phase fluids, or "droplet" microfluidics. These systems disperse an aqueous solution across many fluidic "compartments" divided by a gas or immiscible fluid, stabilized by a surfactant to prevent coalescence. By operating with large numbers of aqueous compartments in parallel or high speed serial streams, assays can be multiplexed at large scales.

This concept was brought to fruition by several key technical developments. First, it needed to be possible to quickly emulsify a sample into emulsions of tunable uniform volumes (*e.g.* a single cell, or a number of molecules depending on their density/concentration). Second, the emulsion chemistry (*i.e.* the choice of the continuous phase and stabilizing surfactant) needed to be compatible with biological systems (*i.e.* low toxicity to cells), and prevent cross-contamination of contents between droplets. Last, analogs of conventional liquid-handling operations (*e.g.* mixing and sampling) and means of measurement needed to be developed.

Technologies for dispersing aqueous solutions into large numbers of uniformly-sized emulsions on the microscale were developed by a number of groups in the early 2000's. The most widely used techniques are the "flow-focusing" and "T-junction" architectures, in which a microscale aqueous fluid stream collides with an immiscible oil stream to break up flow into a discontinuous stream of water droplets [29], [30]. These techniques leverage the deterministic microscale fluid dynamics to reliably create droplets with sizes ranging <1-pL to 1-nL with low-variance (diameter shows <5% coefficient of variation) at high speeds (production rates of millions of droplets per hour). Moreover, including a surfactant stabilizes the droplets against coalescence, allowing their long term manipulation or storage.

Droplet microfluidic devices were first demonstrated using hydrocarbon (*e.g.* decane, tetradecane, and hexadecane) [29] and silicone [30] oil continuous phases, however many components of biological systems are soluble in these oils, both diluting and possibly cross-contaminating the contents of droplets [31]. In order to prevent this issue, it was noted that perfluorocarbon oils are both hydrophobic and lipophobic, and a perfluorocarbon oil continuous phase could prevent the leakage of molecules from the aqueous phase out of the fluidic compartments [32]. Biocompatible fluorosurfactants consisting of polyethylene glycol (PEG) and perfluoropolyether (PFPE) di- and tri-block copolymers were found to both stabilize emulsions, and be biologically inert [33]. Perfluorocarbon oils and surfactants have since become commonplace for droplet microfluidic applications in biology.

The translation of conventional biological assays to droplet microfluidic platforms necessitated the development of droplet-level operations as microscale analogs of conventional liquid handling operations, such as the ability to select and mix samples. In order to be useful, these operations must operate identically on each droplet at high frequency such that all droplets — which could number millions — are processed on the standard timescales of biological assays (*e.g.* hours).

Mixing reagents requires bringing the desired set of droplets to be mixed into physical contact, and then disrupting the surfactant boundary between them. Droplets can be physically co-localized using a variety of hydrodynamic trap architectures [34], and many creative solutions have emerged to coalesce droplets by perturbing the surfactant molecules using electric fields [34], freeze-thawing [35], local heating [36], mechanical disruption by surface acoustic waves [37], and chemical disruption [38]. Electro-coalescence has emerged as the most general and scalable, as pairs of droplets can be hydrodynamically trapped and merged by microfabricated electrodes at high speeds in serial streams [34].

Methods to select or sort droplets rely on similar physical means as coalescence, often by triggering the movement of droplets of interest into a diverging flow channel as they arrive at a forked junction. For example, groups have demonstrated the use of both dielectrophoresis [39] and surface acoustic waves [40] to successfully sort droplets at high flow rates (>100 Hz). Sampling droplets, *i.e.* taking a fraction of the volume for input into a new reaction can also be accomplished by splitting droplets. This can be done by subjecting the droplet to enough fluid shear to overcome the interfacial tension, such as by colliding the droplet with a physical barrier [41].

By integrating these modules together, droplet microfluidic platforms have found many applications across molecular and cellular biology. Examples include testing drug dose response testing across cells [42] or

12

enzymes [43], screening libraries of enzymes for a desired activity in directed evolution experiments [44], screening cells for production of high-value metabolites [45] or antibodies [46], and enabling single cell transcriptomics [47].

# 1.3 Considering microfluidic platforms as an interface suggests factors to broaden adoption

Despite the clear technological potential of microfluidics, broader translation outside of specialized labs has been limited [48]. In a meta-analysis of the biomedical literature, Sackmann *et al* showed that although the number of microfluidics publications grew dramatically from 2000-2012, this growth was seen primarily in engineering journals with little permeation into biology and medicine journals [48].

I believe this slow uptake can be explained by considering a holistic description of microfluidic platforms as interfaces that connect two systems: humans, and fluids at the $10^{-6}$-$10^{-2}$ m length scale. Considering each side of the interface, we can describe how humans interact with the platform ("accessibility"), and also, how the platform supports or interacts with the biological system of interest ("generalizability"). Last, we can consider the "scalability" of the interface, *i.e.* its robustness and capacity to practically scale to large numbers of operations. Taken together, these three factors of accessibility, generalizability, and scalability suggest design principles to widen the translation of microfluidic platforms.

## 1.3.1 Three design principles can improve translation

First, a platform is accessible if it minimizes the usage barriers experienced by most life scientists. This concept includes access to materials, access to necessary instruments to operate the platform, and a shallow learning curve. Through analyzing a case study of microfluidic platforms to study chemotaxis, Sackmann and colleagues suggested that a barrier to translation stemmed from the lack of consideration for these usability requirements: users lacked the necessary instruments (*e.g.* syringe pumps, pneumatic controllers), infrastructure (fabrication), and expertise assumed in common microfluidic designs [48]. Figure 1-2 provides a coarse scale for the accessibility of instruments. The most accessible platforms make use of common equipment found in most life sciences laboratories that most scientists already know how to use,

such as micropipettes and microscopes. The least accessible instruments are those that must be custom built by a specialist, such as an electrophysiology workstation. If components are not commercially available and must be made in-house, there should be good existing evidence for adoption in life science fields.
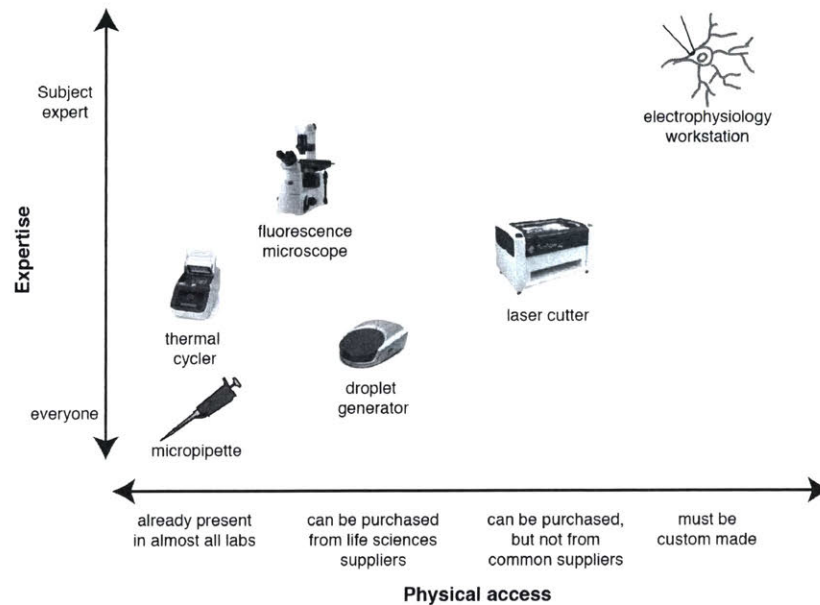


**Figure 1-2. Coarse accessibility scale.** The most accessible instruments are those that are already present in life sciences labs, and that most scientists know how use. The least accessible are those that must be custom built by an expert.

Second, a platform is generalizable if it easily extends to new biological problems and settings. We can abstract an experiment as *(i)* a set of input samples: *e.g.* a set of microbes and a set of antibiotics; *(ii)* performing some kind of processing: *e.g.* mixing together each microbe and antibiotic; and finally, *(iii)* making a measurement: *e.g.* measuring the growth rate of the microbe in each condition. To analyze a platform's generalizability, we can consider both the inputs and the measurement, or assay. "Input scope" describes a platform's capacity to generalize to new inputs, *e.g.* a human cell instead of a microbe; or media conditions rather than antibiotics. "Assay scope" describes the platform's capacity to generalize to new measurements, or the degree to which new assays need to be altered in order to be compatible with the platform, *e.g.* measuring gene expression instead of growth rate. Broad translation of platforms with limited

input or assay scope is difficult because specialists are required to build new solutions whenever experimental needs exceed the supported inputs or measurements.

As a platform, conventional 96-well plates have very broad input scope, as they accept almost any input used in molecular and cellular biology. However, many microfluidic platforms have limited input scope, such as limited support for long term cell cultures due to media evaporation [49], or material incompatibility with small-molecule compounds and media components [50], [51]. Conventional 96-well plates also have broad assay scope, as they are the formats for which instruments in the life sciences are standardized (*e.g.* microscopes or rt-qPCR). In contrast, microfluidic platforms must either *(i)* integrate a means of measurement with the device, or *(ii)* output samples that can be transferred back to a standard format (the so called, "world to chip interface problem" [25]).

Last, a platform is scalable if it can straightforwardly grow to larger numbers of experiments. This considers constraints on the number of inputs and throughput, ease of parallelization, and robustness of the platform. For example, most applications scale easily in 96-well plates. On this platform, there is very low well-well and plate-plate variability so experiments can be parallelized across many plates. Additionally, the regular spacing of wells facilitates the parallelization of liquid handling with multi-channel micropipettes. On the other hand, microfluidic platforms can be difficult to scale for many applications. For example, the high probability of microfabrication defects can limit the complexity of practically achievable fluidic circuits. Microchannels also often easily and irreversibly become clogged with debris. Requirements for active control elements like pneumatic controllers also hinder parallelization.

By improving microfluidic designs along each of these principles, I expect that microfluidic platforms will successfully achieve broader translation across molecular and cellular biology.

## 1.3.2 Limitations of droplet microfluidics indicated by these principles

These design principles illuminate both strengths and areas of improvement of common droplet microfluidic platforms (Table 1-1). While droplet microfluidics have been demonstrated in many diverse applications, the best translated systems are notably those that leverage only molecular biology assays, such as PCR, or cell lysis and nucleic acid capture from cells [47], and only require the single microfluidic-level

operation of droplet production (Table 1-1 left column). Moreover, commercial instruments (Bio-Rad, 10X Genomics, Dolomite) have made these operations even more accessible to scientists. However, many of the more complex cell-biology based applications such as screening drugs [52], [53], or measuring interactions between cells [54], [55] have not seen nearly as much success, with few examples of users outside of specialized labs. This likely due to limitations described in the right column of Table 1-1.

**Table 1-1. Strengths and limitations of common droplet microfluidic platforms.** Starred items are areas addressed by the technology in this thesis.

| Design Principle | Strengths | Limitations<br>*Addressed by this thesis |
|---|---|---|
| **Generalizability - input scope** | **Broad scope for molecular biology reagents**<br><br>Droplet microfluidic platforms support a wide range of nucleic acid- and enzyme-based operations used for molecular biology [56] .<br><br>**Strong support for microbial cell culture**<br><br>Droplet based cell culture has been successfully demonstrated for many microbial species [57], [58]. | ***Restricted scope of small molecule chemical reagents**<br><br>Droplets are not solid compartments and can small molecule contents, depending on chemical properties [56], [59], [60].<br><br>**Restricted scope for eukaryotic systems and long term cultures**<br><br>Mammalian cells – especially those requiring adherent culture show limited viability in droplets [53]. Across any system, nutrient consumption and waste removal are problems for long term culture [61]. |
| **Generalizability - assay scope** | **Strong support for nucleic acid-based assays**<br><br>Owing to strong support of molecular biology reagents, nucleic acid-based assays such as qPCR and sample preparation for sequencing also work with droplet-based systems. For example, recent advances introduced nucleic acid capture on co-emulsified beads, enabling the later sequencing of thousands of single cell transcriptomes [47]. | ***Optical assays must be high-frequency**<br><br>High speed, serial stream processing demands that assays be detected optically at $\sim 10^{-3}$ s / droplet, requiring specialized development of assays [56]. For example, time lapse imaging of droplets requires serial back-and-forth flow over a sensor [62]. |
| **Accessibility** | **Accessible means of droplet production**<br><br>Commercial instruments sold by companies like Bio-Rad and 10X Genomics are becoming widely available. Oil and surfactant necessary for emulsions are commercially available.<br><br>**Materials are widely accessible**<br><br>Microfluidic devices can be easily made from PDMS by soft lithography [13], and designs are often open-source [63]. | ***Limited accessibility of advanced operations**<br><br>Operations such as droplet contents decoding, or droplet merging, sorting, and selection can require microfabricated electrodes, optical sensors, and instrumentation designed by specialists [52], [53], [56].<br><br>**Custom fabrication of devices requires expertise**<br><br>Although materials and designs are accessible, many scientists lack expertise for fabrication. |
| **Scalability** | **High throughput processing of droplets**<br><br>Droplet microfluidic platforms process droplets at $\sim 0.1$-1 kHz frequency, scaling to 100,000+ droplets linearly with time of operation [56].<br><br>**Nucleic acid assay scope enables scalable encoding of reagents**<br><br>In conventional 96-well plates, reagents are encoded by their well address (*e.g.* A1, E3). Droplets must also maintain some information encoding their contents. If droplet contents can be decoded by nucleic acid-based assays, the high information density of nucleic acids provides a very large encoding space (1+ million codes) [47]. | ***Poor robustness of serial operations**<br><br>Serial designs for processing of droplets are vulnerable to any interruption of the serial stream, for example, clogging of microfluidic channels with debris.<br><br>**Optical assay scope limits encoding of reagents**<br><br>Unlike nucleic acid-based assays, optical assays are restricted by the requirement for high-frequency readout and integration with optical sensors. To my knowledge, no study has demonstrated more than 10 codes per fluorescence channel ([52] constructs 8, and [53] constructs 8-10). |

# 1.4 A microfluidic platform for combinatorial experiments

A distinguishing feature of biological systems is not just that the components (*e.g.* biomolecules, cells, tissues, and organisms) span such a broad range of length scales (Figure 1-1), but that these components are also assembled in hierarchical sets. Each layer of the hierarchy features its own properties, often described in terms of a set of the components from the previous layer. For example, we describe a genome by a set of genes, and each gene is in turn an ordered set of nucleotides. We likewise describe a tissue by a set of different cell types, including their spatial organization and functional interactions.

Because we study biology by varying the components of these sets, biological experiments are inherently combinatorial in nature. Combinatorics induce explosive experimental complexity that quickly limits feasibility, requiring the development of new means of measurement and manipulation. These technologies have been well developed at biomolecular length scales, but not at larger length scales. For example, at the length scale of small molecules and biomolecules (Figure 1-1), combinatorics can be efficiently generated by split-and-pool strategies for diversity-oriented synthesis of small molecules [64] and solid-phase synthesis of DNA and peptides [65]. Similarly, at the length scale of genes (Figure 1-1), combinations of genetic material (*e.g.* genes, CRISPR gRNAs or RNAi) are easily generated in plasmids with clever uses of standard recombinant DNA assembly methods like CombiGEM [66] and MoClo [67].

At larger length scales ($10^{-6}$-$10^{-2}$ m) ranging prokaryotic cells to microbial communities and eukaryotic tissues and where microfluidic platforms are a common means of manipulation, few technologies efficiently address combinatorics. As a result, cell-based combinatorial experiments such combinatorial drug screening and microbial community assembly are commonly performed in conventional 96-well plate formats, and are strongly limited by the complex liquid handling needed to assemble combinations, consumption of large volumes of reagents, and high costs.

This thesis introduces a new droplet microfluidic platform to attack the challenges of these combinatorial experiments. Our platform *(i)* produces nanoliter scale droplets from a set of $n$ input reagents; *(ii)* mixes random sets of $k$ droplets; and *(iii)* measures the resulting $\binom{n}{k}$ data points using an optical assay (*e.g.* fluorescence microscopy). This design considerably reduces logistical complexity of these experiments from $\binom{n}{k}$ to roughly $n$ liquid handling steps; and reduces reagent consumption and costs due to its nanoliter

volumes and high experimental throughput. Moreover, the design of our platform addresses several design limitations to improve the accessibility, generalizability, and scalability of droplet microfluidic platforms (Table 1-1, starred items).

Chapter 2 provides an overview of the design of our platform and critically evaluates performance. I discuss how our design choices specifically manage various challenges in droplet microfluidics (Table 1-1, starred items), and show that our design make order of magnitude or greater improvements over approaches using conventional liquid handling in 96-well plates.

Chapters 3 and 4 describe applications of our technology to two separate but related cell-based combinatorial experiments. In Chapter 3, we use our platform to enable screening of pairwise combinations of antibiotics and non-antibacterial drugs to overcome intrinsic antibiotic resistance in the model Gram-negative bacterial pathogen *E. coli*. This screen demonstrates the scalability and accessibility of our design, as we process 4+ million droplet-level assays by hand in just 10 days to discover more than 10 combinations of drugs for further study.

Chapter 4 describes the expansion of our platform to microbial ecology, in which the interactions between microbes in communities can dictate functions important for both basic science and biotechnology. We use our platform to analyze both pairwise interactions between microbes, and deconstruct higher-order interactions in a 4-strain community.

Finally, in Chapter 5, I discuss proof of concept for several technical advancements of our platform to expand the generalizability and scalability. Additionally, I explain how the bio-inspired concept of "self-assembly" underlies many of the design advantages our platform, and comment on how this principle might further impact the field of microfluidics.

# Chapter 2

# A microfluidic platform for combinatorial experiments

*This chapter provides an overview of our platform, with applications appearing separately in Chapters 3 and 4. Additionally, as we continued to develop the platform throughout work in this thesis, I divide two iterations of the platform as "Generation 1" and "Generation 2." Generation 1 was used in Chapter 3, while Chapter 4 uses Generation 2.*

*Much of this chapter appears in Kulesa, Kehe, et al.* Proceedings of the National Academy of Sciences, 2018 [68]. *However, Generation 2 designs will be published separately with Chapter 4.*

*This work was in collaboration with Jared Kehe, including the microwell designs, fabrication, and design of the loading assemblies. Additionally, many of the original concepts behind the microfluidic and fluorescence encoding approaches were developed in collaboration with David Feldman and Navpreet Ranu.*

## 2.1 Abstract

Experiments in biology are often combinatorial in nature and require analysis of large multi-dimensional spaces, but the scales of these experiments are limited by logistical complexity, cost, and reagent consumption. By miniaturizing experiments across nanoliter-scale emulsions that can be processed at large scales, droplet microfluidic platforms are poised to attack these challenges. Here we describe a droplet microfluidic platform for combinatorial experiments that automates the assembly of reagent combinations, with order-of-magnitude improvements over conventional liquid handling. Moreover, our design is accessible, requiring only standard lab equipment such as micropipettes, and improves the chemical compatibility of droplet microfluidic platforms for small molecules.

## 2.2 Introduction

Biological systems are made up of many components (*e.g.* genes, proteins, cells, and organisms), that each have their own multiple degrees of freedom. Hence, many experiments require the analysis of large, combinatorial spaces. However, these experiments can be as intractable as they are ubiquitous, and the systems-level understanding needed to advance biology demands new methods to analyze these combinatorial spaces. For example, combinations of drugs show promise for many different therapeutic uses ranging from cancer to viral infections [69]–[73], but the search spaces for new combinations quickly exceed the capacity of conventional drug discovery methods [74]. To test all pairwise combinations of the ~2000 drugs currently approved by the FDA would require ~2 million assays, and to test three way combinations requires ~1.3 billion. Another example is given by efforts to unravel or engineer interactions between the many microbial species that constitute the microbiomes of soil or the human gut [75]–[78] .

Experiments on these systems are limited not only by the cost created by such explosive scales, but also by the logistical complexity and reagent consumption necessary to explore many combinations. As a result, the ability to carry out these experiments are limited to highly specialized labs, often with access and the required expertise to use complex robotic systems. To directly address the difficulties of combinatorial experiments, a new platform should make order-of-magnitude reductions in logistical complexity (*i.e.* the number of liquid handling steps), costs, and reagent consumption.

Droplet microfluidic platforms provide a natural starting place to attack the challenges of combinatorial experiments. Recent advances in droplet microfluidics have made broad impacts across the life sciences by allowing common well-plate benchtop processes to be performed in a high speed serial streams of 100,000+ water-in-oil emulsion droplets [56]. By performing operations over a set of droplets, logistical complexity can be effectively hidden from the user. The sketch of a system to construct pairwise combinations of reagents illustrates the simplicity: *(i)* emulsify each reagent; *(ii)* pool the droplets carrying each reagent; and *(iii)* randomly pair and merge droplets in a serial stream in effectively a single operation. The nanoliter-scale volume of individual droplets also promises to reduce reagent costs. However, reviewing droplet microfluidic platforms in light of the earlier design principles described in Chapter 1 suggests a number of other issues with this design sketch that should be addressed to improve this approach (see Section 1.3.1 and Table 1-1).

In this chapter, we introduce a droplet microfluidic platform for combinatorial experiments that automates the assembly of reagent combinations, with order-of-magnitude improvements over conventional liquid handling in 96-well plates. Moreover, our design addresses the considerations of accessibility, generalizability, and scalability (Chapter 1, Table 1-1 starred items) by requiring only standard lab equipment such as micropipettes and a fluorescence microscope, improving the chemical compatibility of droplet microfluidic platforms for small molecules, and processing droplets in parallel rather than in series to improve robustness. We provide an overview of the methodology, describe how it aligns with these design principles, and then critically evaluate the technical performance. An operational manual is also provided at the end of this chapter to guide future experiments (Section 2.6). Taken together, we expect that this provides a generalizable platform for combinatorial experiments in molecular and cellular biology.
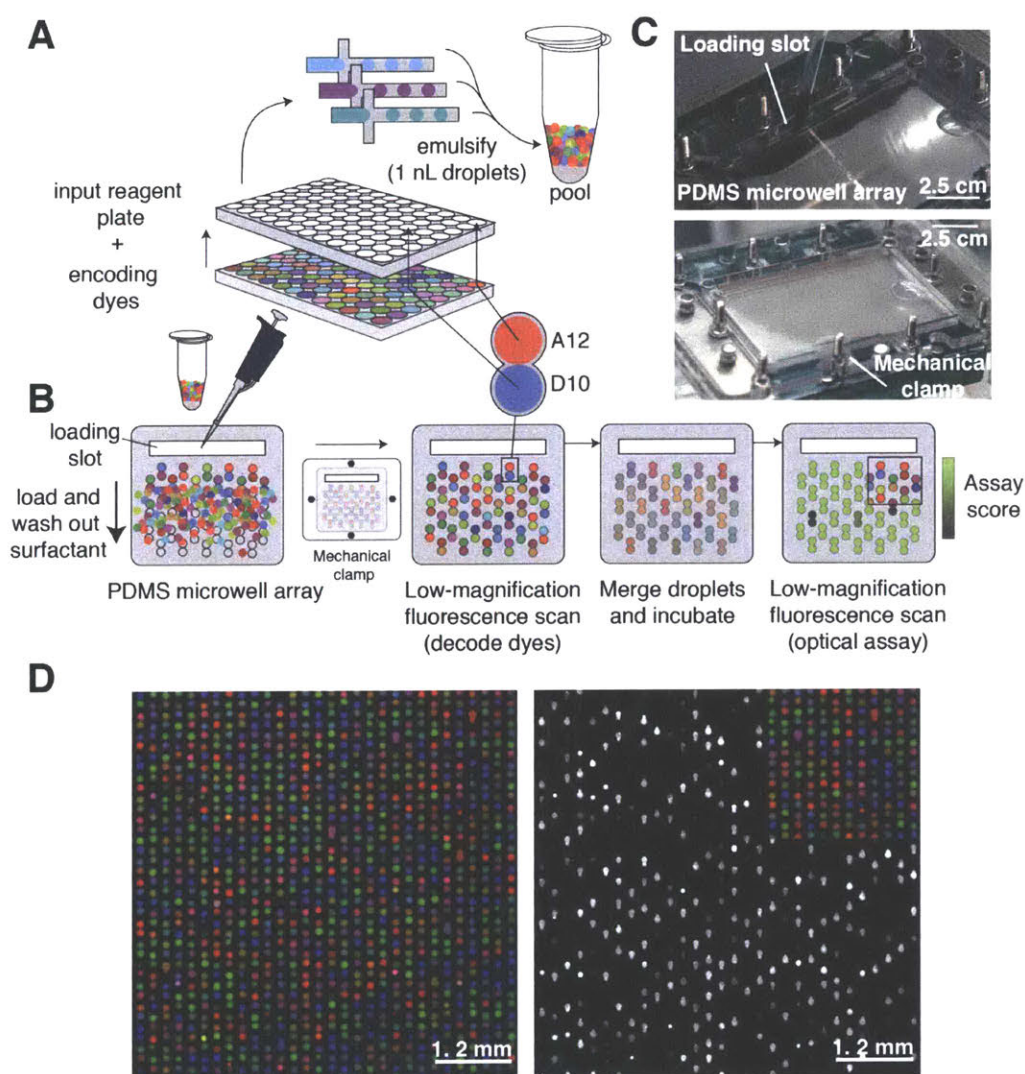
# 2.3 Results



**Figure 2-1. Platform overview.** As a proof of concept, we developed our first design for assembly of pairwise combinations of reagents, termed "Generation 1." (**A**) Reagent inputs and encoding dyes are emulsified into nanoliter droplets and subsequently pooled. (**B**) A microwell array randomly captures droplets. Once loaded, free surfactant is depleted by washing to limit chemical exchange between droplets. Low-magnification epifluorescence microscopy decodes the reagent carried by each droplet. Sets of droplets in each microwell are merged and incubated. A second optical scan reads out an optical assay (*e.g.* cell growth inhibition). (**C**) Photographs of the microwell array during loading. Scale bars are approximate due to perspective effect. (**D**) Three-color fluorescence micrograph of droplets in microwell array paired with a subsequent assay of growth inhibition of *E. coli* cells, monitored by fluorescence from constitutively

expressed GFP. Only 50% of droplet inputs contained cells, therefore a fraction of microwells do not show GFP fluorescence.

## 2.3.1 Platform overview

Figure 2-1 sketches a simple description of how our platform automatically constructs and assays all combinations of a set of input reagents, such as cells, media conditions, or compounds (Figure 2-1). We combine reagents in well plates with encoding dyes, and emulsify a sample from each well into 20,000 1-nanoliter aqueous droplets in a surrounding fluorocarbon oil and stabilizing surfactant (Figure 2-1A). We use standard micropipettes to pool and load the droplets into a microwell array such that each microwell captures droplets at random, and then seal the array to the glass bottom using a mechanical clamp (Figure 2-1B). The microwells can be designed to reliably capture a specific number of droplets ($k$). Figure 2-1B shows our first proof of concept, "Generation 1," where microwells were designed to capture sets of two droplets, but we generalize this design to $k$ droplets in Section 2.3.2.

The contents of each droplet are encoded by a ratio of fluorescent dyes, such that we can use a low-magnification fluorescence microscope to identify the reagent in each droplet (Figure 2-1D) [52], [53]. To merge the sets of droplets in each microwell, we apply a high voltage, high frequency alternating electric field to induce droplet fusion [79], and then incubate the array for the time necessary for the assay to take place. The array can be subsequently imaged to measure an optical signal such as GFP fluorescence of cells or fluorogenic enzyme activity, and these measurements can be assigned to the set of input reagents carried by the droplets present in each microwell (Figure 2-1D).

This design enables combinatorial experiments by considerably reducing liquid handling complexity, costs, and reagent consumption. Only the droplets must be produced ($\sim 3n$ steps, see Section 2.6.10) to automatically construct $\binom{n}{k}$ combinations, reducing liquid handling complexity. To reduce baseline materials costs, microwells can be packed at $\sim$1000-fold higher densities than conventional 96-well plates. Last, the minute volumes required also reduce reagent consumption.

Moreover, the microwell-based design improves upon many of the limitations of current droplet microfluidic platforms along the specific design principles described earlier (Table 2-1). In the following sections, we will develop each point and quantitatively evaluate performance.

**Table 2-1. Outline of results sections and corresponding design principles.**

| Results section | Impact | Design principle |
|---|---|---|
| **2.3.2 Microwells assemble reagent combinations in parallel and without active microfluidic components** | **Improved accessibility of merging operation**<br><br>Our microwell design is operated by conventional micropipettes using only passive microfluidic components. | Accessibility |
| | **Improved robustness from parallelization rather than serialization**<br><br>The parallel nature of the droplet processing by passive microwells is robust to errors that would normally disrupt serial processing. Fabrication defects and debris have only a local impact on the large array. | Scalability |
| **2.3.3 Microwells allow decoding of droplet contents prior to merging by low-magnification microscopy** | **Improved accessibility of droplet decoding method**<br><br>Our simple fluorescence encoding strategy uses only low magnification (2X or 4X) fluorescence microscopy available to most labs. This stems from the fact that droplets can be decoded prior to merging and remain in fixed positions. In common droplet microfluidic platforms, the set of droplets merged to would need to be decoded from the merged droplet [52], a much harder encoding challenge. | Accessibility |
| **2.3.4 Microwells extend compatibility for small molecules by limiting chemical cross-contamination between droplets after loading** | **Extended input scope of small molecule chemical reagents**<br><br>Our microwell design limits the exchange of droplet contents, an issue which has restricted the chemical combability of droplet microfluidics for small molecules (such as in drug screening applications) [56], [59], [60]. The extent of compound exchange is limited by loading droplets rapidly into solid microwell compartments, and by depleting the free surfactant that mediates exchange [59], [80]. As a result, the opportunity for exchange is restricted to the much shorter pooling and loading phases. This extends the chemical compatibility of our platform to a broader range of small molecules. | Generalizability - input scope |

26
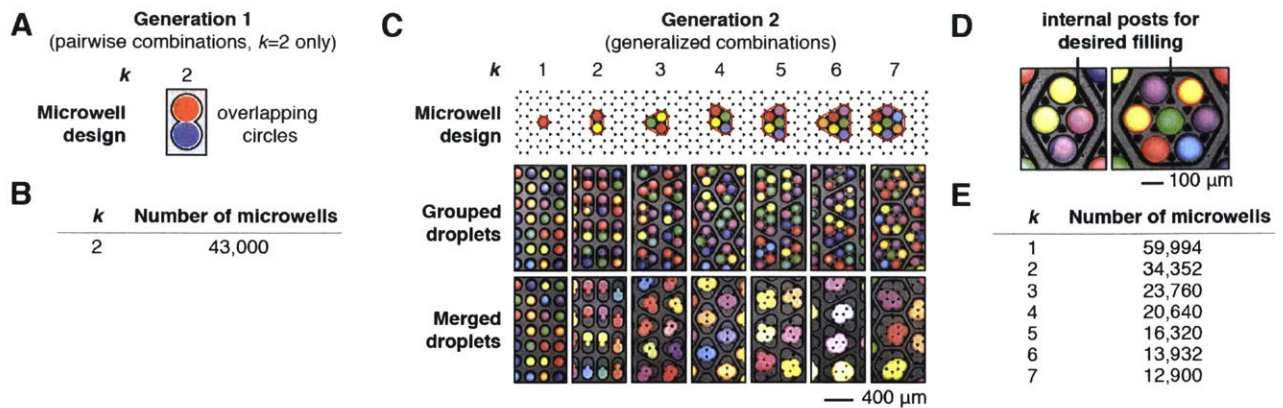
**Figure 2-2. A simple design rule for assembling combinations of droplets.** (**A**) As a proof of concept for assembling pairwise combinations, "Generation 1" microwells were designed with two overlapping circles. (**B**) Generation 1 microwell array chips had 43,000 microwells on a 6.2 cm × 7.2 cm chip area. (**C**) Generation 2 designs derive $k$-wise merging microwell designs from a hexagonal lattice of droplets (**D**) Internal posts position droplets to achieve high efficiency loading. (**E**) The number of microwells on a 6.2 cm × 7.2 cm chip area for Generation 2 chips and different values of $k$. As microwells for larger values of $k$ haver larger footprints, lower microwell densities are achieved.

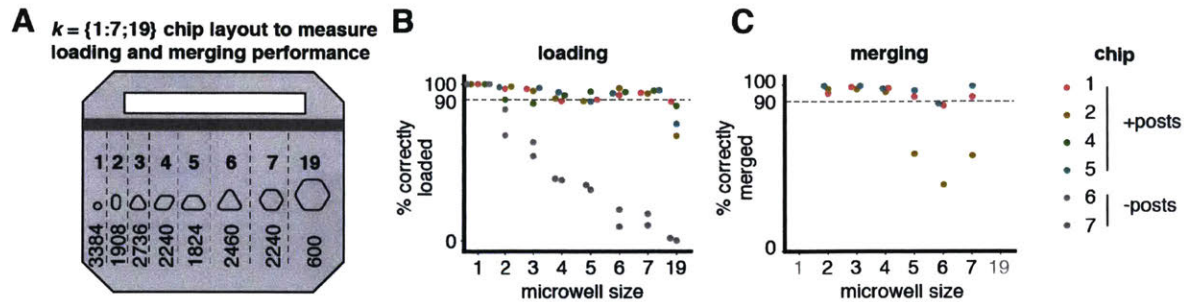**Figure 2-3. Microwell loading and merging performance.** (A) To test each microwell design, we constructed a microwell array chip composed of columns of microwells designed for $k = 1, 2, …, 7$, and 19 droplets. The columns within the chip show the number of microwells corresponding to each value of $k$. (B) For each microwell size, the percentage of microwells that were loaded with the desired number of droplets is shown for each replicate chip (colored dots, with legend shown at right). To determine the effect of internal post features on loading performance, chips containing microwells without posts were also loaded (gray dots). (C) The percentage of correctly loaded microwells that showed complete merging of droplets. Merging was not measured for $k=1$ microwells (by definition) and $k=19$ microwells due to limitations of data analysis methods (see Section 2.6.8). Chip 4 was also not merged due to an experimental error.

## 2.3.2 Microwells assemble reagent combinations in parallel and without active microfluidic components

Microwells provide a simple, passive mechanism for assembling reagent combinations by merging of random sets of droplets, as the buoyancy of the aqueous droplets in the denser fluorous oil continuous phase automatically assorts the droplets into microwells [81], [82]. This design addresses accessibility and scalability. First, the user only pools and injects the droplets underneath the microwell array using a standard micropipette, and no active fluidics are required (*e.g.* syringe pumps and pneumatically actuated valves). Additionally, the parallel nature of the microwells makes it robust to any debris or microfabrication defects that commonly afflict microfluidic platforms.

As a proof of concept, we designed our "Generation 1" devices to construct pairwise combinations of the input droplets (Figure 2-1, Figure 2-2A). In "Generation 2," we made subsequent improvements to (*i*)

generalize microwell designs to $k$-wise merging; and *(ii)* improve loading efficiency through size selection of droplets.

We hypothesized a design scheme could be generalized to load and merge any number of droplets using iteratively larger microwell shapes ( Figure 2-2C). The observation that two-dimensional arrays of droplets can be packed in the hexagonal lattice sphere-packing configuration suggested that microwell designs to load $k$ droplets could be derived from the convex hull of $k$ circles. However, we found that droplets did not naturally self-organize to optimally fill the microwell, and many microwells did not receive the expected number of droplets. We hypothesized that the placement of triangular posts at the voids in the lattice would improve loading performance ( Figure 2-2D).

Additionally, to achieve precise loading of larger wells it became critical to filter out smaller droplets. Though droplets are fairly uniform in size, the process of pooling and injecting the droplets can shear droplets into smaller volumes. Naturally, these smaller droplets can over-load microwells. To remove these droplets, we placed a line of narrow trenches at the inlet of the microwell array. Droplets in the expected size range are too large and pass over the trenches, but small droplets are trapped.

To test our design strategy, we created arrays comprised of microwells designed for 1, 2, ... , 7 droplets (Figure 2-3A). As a more stringent test of the generalizability, we also included microwells designed to receive 19 droplets. We found that most microwell designs robustly achieved 90+% loading efficiency, defined as the fraction of microwells that received the desired number of droplets (Figure 2-3B). As expected, the performance of microwells without interior posts also steadily declined with increasing size.

To measure merging performance, after loading we exposed each chip to the high voltage, high frequency alternating electric field to induce electro-coalescence of the set of droplets in each microwell. We found that for 2/3 chips tested, >90% of microwells showed complete merging for most values of $k$ (Figure 2-3C).
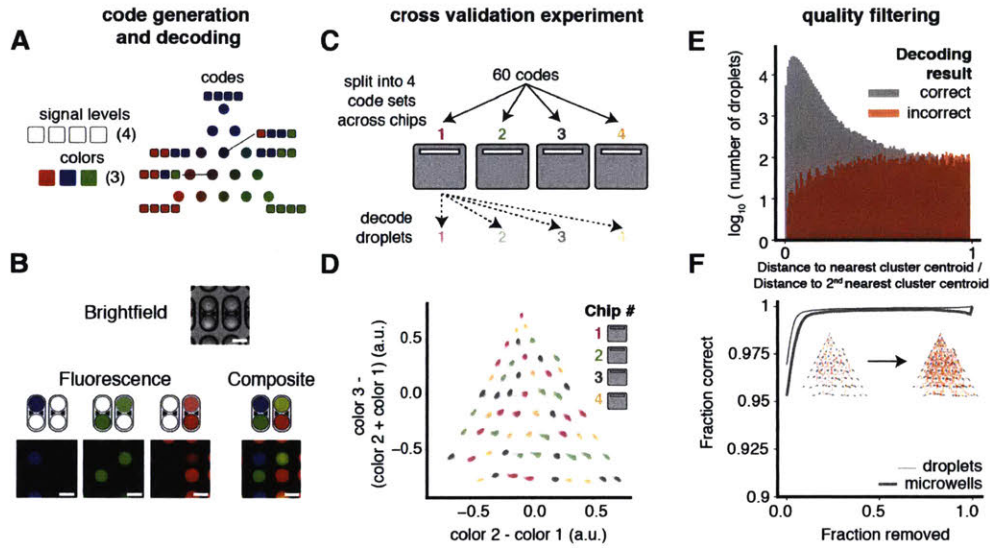
**Figure 2-4. Fluorescence encoding performance**. (**A**) Fluorescence codes are constructed from varying discretized signal levels of each dye, such that the code has the same total dye signal (and concentration, typically 1 μM). (**B**) Droplets are decoded by sequential imaging of fluorescence channels corresponding to each encoding dye. Scale bars represent 150 μm. (**C**) To measure performance, we created droplets with a set of 60 codes from 3 colors and 10 signal levels (see Table 2-2). The set of 60 was divided into four sets of 15, split across four chips (*k*=2). We determined that droplets were incorrectly decoded if they were assigned to a code that was not represented on the chip. (**D**) The three-color fluorescence values of each droplet (n = 164,024 across 82,012 wells) are shown as a two-dimensional projection. Each point is plotted at 1% opacity. (**E**) For each droplet, quality can be scored by computing the distance of the fluorescence values to the centroid of its assigned cluster, and comparing to the distance to the centroid of second nearest cluster. A histogram shows the fraction of total droplets that were identified as incorrectly decoded as function of this score. (**F**) Removing droplets above a score threshold can improve the fraction of correctly decoded droplets (thin gray line). Microwells containing at least one droplet above the score threshold can also be removed (thick gray line). Using the same projection as part D, insets show removed droplets beyond the score threshold (red) compared to passing droplets (gray).

**Table 2-2. Number of fluorescence codes possible.** *The set used in Figure 2-4C, D. **Possible strategies for a full set of codes for a 96-well plate. ***A possible strategy for a full set of codes for a 384-well plate.

| | | Number of discernible signal levels | | | | | |
|---|---|---|---|---|---|---|---|
| | | 10 | 11 | 12 | 13 | ... | 27 |
| Number of dyes | 3 | 66* | 78 | 91 | 105** | | 406 |
| | 4 | 286** | 364 | 455*** | 560 | | 4,060 |

# 2.3.3 Microwells allow decoding of droplet contents prior to merging by low-magnification microscopy

In conventional 96-well plates, reagents are encoded by their well address (*e.g.* A1, E3). Droplets must encode this information using different strategies, such as the concentration of a fluorescent dye that can be read by an optical sensor [52], [53]. In common droplet microfluidic platforms, the need to decode droplet contents in a serial stream presents formidable challenges to the accessibility. First, optical sensors must be integrated with fluidic devices requiring custom instrumentation [56]. Second, since droplets cannot be tracked between the point of decoding and a later assay, decoding droplet contents and conducting an experimental measurement must take place at the same point. This is especially challenging in a combinatorial experiment because the experimental measurement is conducted on a merged droplet, so the encoding scheme must not lose information upon merging (*e.g.* if pre-merged droplets are encoded with different levels of a single fluorescent dye, merging can lose information because levels will be averaged).

Microwells resolve these challenges to enable a simple optical encoding strategy with high accessibility. Microwells hold droplets in fixed positions such that they can be imaged with widely available fluorescence microscopes. Additionally, the contents of droplets within each microwell can be decoded prior to merging.

Ahead of making droplets, each input is mixed with a unique ratio of fluorescent encoding dyes (Alexa Fluor 555, 594, 647, Thermo-Fisher Scientific) standardized to the same total dye concentration (typically 1 μM) (Figure 2-1A, Figure 2-4A). These fluorescence dye ratios can then be detected and assigned to each droplet with a low-magnification fluorescence scan before the droplets are merged (Figure 2-4B). Each microwell can then be matched with the later imaged optical assay (*e.g.* growth of cells reported by constitutive GFP expression) according to each microwell's position in the array (Figure 2-1D). Typically,

three encoding dyes are used, however this method can generalize to the number of distinguishable fluorescence channels available (Table 2-2). By standardizing total dye concentrations to the same concentration (*e.g.* 1 μM), the encoding is robust to systematic differences in fluorescence signal between droplets, for example non-uniform illumination across the microscope's field of view.

To measure the performance of this method, we measured decoding performance of droplets carrying codes composed of three fluorescent dyes (Figure 2-4C). By dividing each dye into 10 signal levels, we could construct up to 66 codes (see Section 2.6.3). We produced droplets carrying 60 different codes, divided into four sets of 15 and split across different four chips featuring $k=2$ microwells (Figure 2-4C). Imaging each chip yielded a fluorescence signal from each droplet as a point in 3-dimensional space (Figure 2-4D shows a 2-dimensional projection). Droplets were determined to be incorrectly decoded if they were nearest to a cluster of points that represented a code that was absent on a given chip. Since incorrect decoding can only be detected by comparing the 15 codes present on a given chip to the 45 present on the others, we estimated the decoding inaccuracy rate as 4/3 the number of incorrectly decoded droplets found. Overall, using this method we found that <5% of droplets are incorrectly decoded (Figure 2-4F).

To improve the performance, each droplet can be assigned a "quality score" by comparing the distance of its fluorescence values to the centroids of the nearest and $2^{nd}$ nearest clusters. Removing droplets exceeding a score threshold improved decoding performance to >99% accuracy (Figure 2-4F). In most applications, we expect this will not be necessary since we can compute a median of signal levels across replicate microwells containing the same set of droplets, which is stable to outliers caused my misclassification. However, applications where the signal from every microwell are used may benefit from applying a quality score threshold.

The 66 dye ratio codes given by the encoding scheme in Figure 2-4D were sufficient for applications described throughout the rest of this thesis. Due to combinatorial scaling, most experiments are more limited by the number of microwells on a chip rather than the total number of inputs (see Figure 2-7). Only inputs to the same chip require unique encodings, and the number of unique codes is rarely limiting. For example, in Chapter 3, pairwise combinations of drugs from two libraries are screened by dividing one library into 156 batches run across individual chips.

For other applications where larger numbers of codes may be required, we expect this encoding scheme can scale to 96 or 384 inputs on a unique chip (Table 2-2; see Section 2.6.3 for derivation). We expect that three dyes can be used to create enough codes for a 96-well plate input by using 13 dye signal levels,

bringing clusters ~23% closer in Figure 2-4D. However, enough codes for a 384-well plate input would require 27 signal levels for three encoding dyes. In this case, it would be a better choice to use a fourth encoding dye to generate enough codes from 12 dye signal levels, yielding 455 total codes (clusters would be ~17% closer in Figure 2-4D).
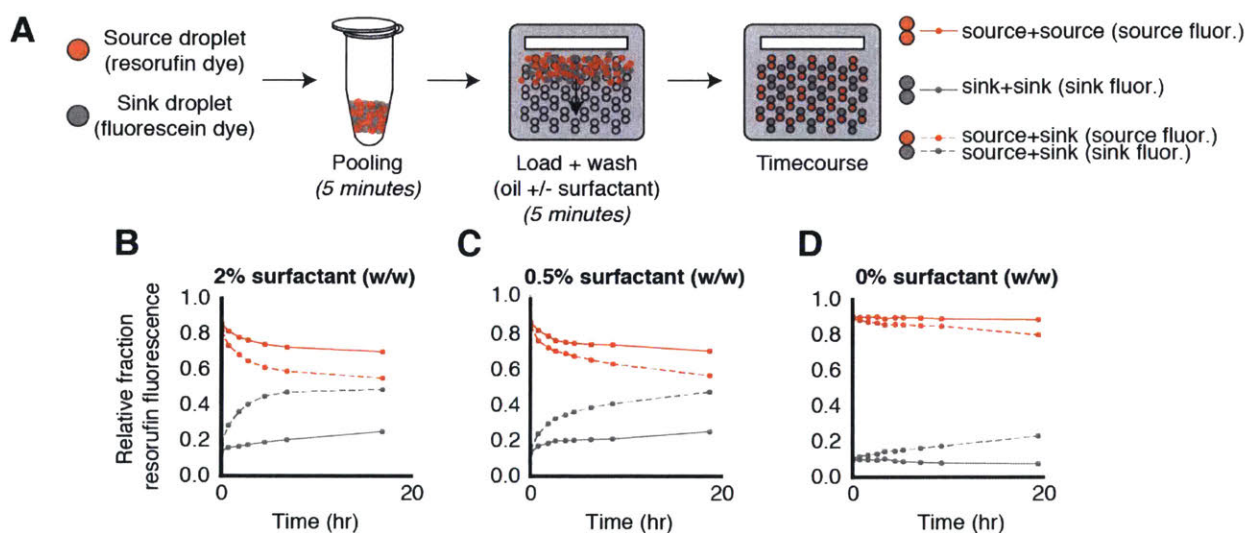


**Figure 2-5. Compound exchange between droplets in microwells.** (**A**) To model cross-contamination, we tracked the exchange of the fluorescent dye resorufin (carried by "source droplets") to empty droplets ("sink droplets", encoded by fluorescein). (**B, C, D**) Exchange is measured over time by the fraction of fluorescence measured in source droplets (red lines) and sink droplets (gray lines) as a function of surfactant wash concentration (0%, 0.5% and 2% w/w). The effect of compartmentalization is measured by comparing the rates of dye accumulation in sink droplets when co-compartmentalized in microwells with source droplets (dotted lines) or other sink droplets (solid lines). Exchange that occurred during the pooling phase was measured by the fraction of fluorescence in sink droplets at the first timepoint.

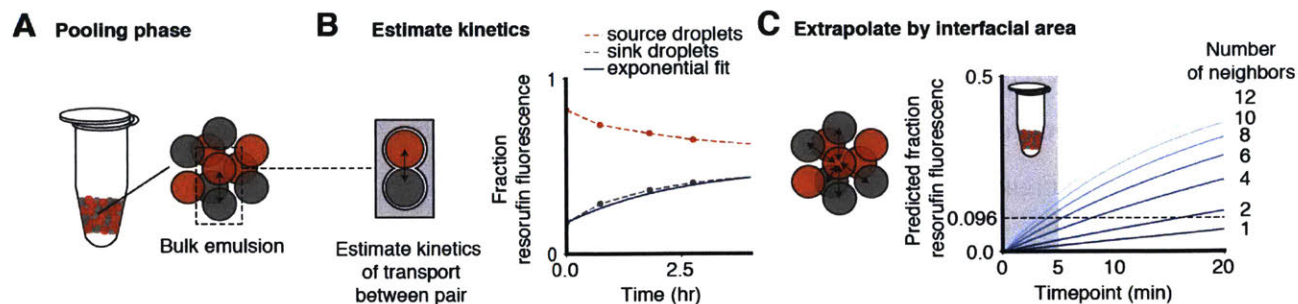**Figure 2-6. Compound exchange between droplets during pooling phase.** (**A**) During the pooling phase, droplets are mixed in a bulk emulsion, modeled by a 3-dimensional hexagonal lattice of droplets. (**B**) We used $k=2$ microwells to model transport between neighboring droplets in the bulk emulsion (using the same dataset as Figure 2-5). We tracked the accumulation of dye in the sink droplets (gray dashed) and the loss of dye from the source droplets (red dashed) in 2% w/w surfactant (as is present during pooling; same data as Figure 2-5B). Previous studies established that the kinetics of exchange follow a single exponential at early timepoints, and a power law at later timepoints [59]. An exponential fit of the data is shown as a solid blue curve. (**C**) To predict transport in a bulk emulsion setting, we linearly extrapolated the fit kinetic constant in part B by the increase in interfacial area of up to 12 neighboring droplets. We compared these predictions to observed quantities in Figure 2-5D. In the experiment described in Figure 2-5, source and sink droplets were pooled in a 1:1 ratio for 5 minutes, and loaded into microwells for 5 minutes. At the first timepoint, the fraction of resorufin dye in the sink droplets in sink-only wells (0% w/w surfactant) was measured as 0.096 (Figure 2-5D), shown as a black dotted line. For comparison, the predicted exchange from our model over the 5 minute timescale is highlighted (gray).

## 2.3.4 Microwells extend compatibility for small molecules by limiting chemical cross-contamination between droplets after loading

A challenge in droplet microfluidics that has limited many applications such as cell-based compound screening is the exchange of compounds between droplets on assay-relevant timescales (1-100 hours) [56], [59], [60]. Compound exchange is mediated by the dynamic equilibrium of surfactant molecules between the aqueous-oil interface and reverse-micelles in the oil phase. Compounds partition into surfactant reverse-micelles that then diffuse through the oil phase and re-fuse with new droplets [59], [80]. Naturally, this

phenomenon has limited the input scope of droplet microfluidic platforms to compounds with minimal partitioning into surfactant reverse-micelles, typically hydrophilic or high-molecular-weight compounds [56], [59], [80].

Though it cannot be entirely eliminated, the microwell array design limits this phenomenon and improves the support for small molecules, enabling new applications such as cell-based drug screening (described in Chapter 3). In our workflow, transport of compounds can occur between droplets during the pooling of droplets (5 minutes), and between microwells after droplets are loaded (1-50 hours). The microwell array restricts exchange during this longer phase by *(i)* depleting free surfactant by an oil wash, and *(ii)* limiting reverse-micelle diffusion between microwells by mechanically sealing the microwell array to a substrate.

*Estimation of compound exchange between microwells*

To model compound exchange, we monitored the transport of the fluorescent dye resorufin (a reference compound commonly used to assess chemical cross-contamination [59], [60], [80]) from "source" droplets to "sink" droplets (encoded by fluorescein, a slow-exchanging dye) (Figure 2-5A). Exchange between droplets in microwells can be monitored directly via imaging the microwell array over time. We found that compartmentalization alone (without depletion of free surfactant) limited resorufin transport compared to exchange between pairs of droplets in the same microwell (Figure 2-5B). Depleting free surfactant by washing the loaded microwell array prior to sealing further decreased exchange to levels below our detection limit (Figure 2-5C, D).

*Estimation of compound exchange during droplet pooling*

The pooling phase just prior to loading still presents an opportunity for compounds to exchange between droplets. We predict that for compounds of similar hydrophobicity to our reference compound, resorufin, this can be limited to <10%.

During droplet pooling, droplets are dispersed in a three-dimensional bulk emulsion of packed spheres. We model the bulk emulsion of pooled droplets by *(i)* measuring the exchange rate between a single pair of neighboring droplets using the microwell array; *(ii)* extrapolating these measurements to a bulk emulsion with multiple neighboring droplets; and *(iii)* comparing our model's predictions to observed quantities.

We measured the kinetics of resorufin exchange between neighboring droplets in microwells containing one source and one sink droplet (Figure 2-5A, Figure 2-6A). Previous studies have shown that the kinetics follows a single exponential at early times, and a power law at later times [59]. We therefore modeled

exchange at timepoints up to 2 hours by a single-exponential (Figure 2-6B), from which we could fit a kinetic constant (see Section 2.6.9).

Since each neighboring droplet in the bulk emulsion can participate in compound exchange, the rate could be increased relative to the estimate from microwells containing only two droplets (Figure 2-6C). For example, a droplet carrying Compound A may neighbor two droplets carrying Compound B. Therefore, we linearly extrapolated the fit kinetic constants in measured in Figure 2-6B by the increase in the interfacial area based on the number of neighboring droplets carrying a given compound (Figure 2-6C) (see Section 2.6.9).

As an experimental test of our prediction, we estimated the exchange between source and sink droplets during pooling in the experiment described in Figure 2-5. Since we do not detect any increase in resorufin in microwells containing only sink droplets (Figure 2-5D), the fraction of fluorescence detected at the first timepoint (.096) must have occurred during the pooling step. Source and sink droplets were pooled in a 1:1 ratio, so we expect that during pooling, for a given sink droplet, an average of 50% of the ~12 neighboring droplets in the three-dimensional bulk emulsion are source droplets (with the distribution as binomial). This measurement (0.096) is in good agreement with our predictions of exchange rate for four neighboring source droplets over the duration of the pooling step (Figure 2-6C).

While in this experiment source and sink droplets were pooled in a 1:1 ratio, most applications will pool equal volumes of droplets over a large set of distinct inputs (e.g. 64), so the fraction of droplets carrying a specific compound is expected to be much smaller. In these circumstances, it is rare that a given droplet will neighbor more than one droplet carrying the same compound, so kinetics for gain of a single contaminant compound are described by one neighbor, but the kinetics for loss of a compound are described by multiple neighbors (Figure 2-6C).

*Generalizing resorufin measurements to other compounds and experimental settings*

In these experiments we used resorufin dye as a convenient model, however applying these measurements to other compounds and settings requires two considerations. First, exchange kinetics depend on compound properties, specifically those that affect the relative affinity of a given compound for reverse-micelles [56], [59], [80]. Empirically, we see that more hydrophobic compounds exchange faster (fluorescein exchanges more slowly, and rhodamine more quickly than resorufin) and that LogD (log10 of the octanol-buffer partition coefficient) is a useful predictor of exchange rate. The cLogD value (a prediction of hydrophobicity at pH 7.4, computed by Accelrys Pipeline Pilot) of resorufin is 1.586, which is of middling

36

hydrophobicity compared with drug-like compounds. We expect that compounds that are much more hydrophobic than resorufin will likely be diluted across many other droplets below active concentrations during the pooling phase.

Second, gain of a contaminating compound (*i.e.* a false positive) is likely more limited than loss of a compound (*i.e.* a false negative) according to the predictions in Figure 2-6C. Different applications may value these differently. For example, a drug screen may only value the validation rate, which is influenced by the false positive rate (gain of a contaminant compound), but not the false negative rate or sensitivity (loss of a compound). However low sensitivity should be expected for more hydrophobic compounds.

Taken together, these results suggested that our microwell design could indeed enable drug screening applications with limited false positive rates from compound exchange, which we pursue in Chapter 3.

# 2.4 Discussion
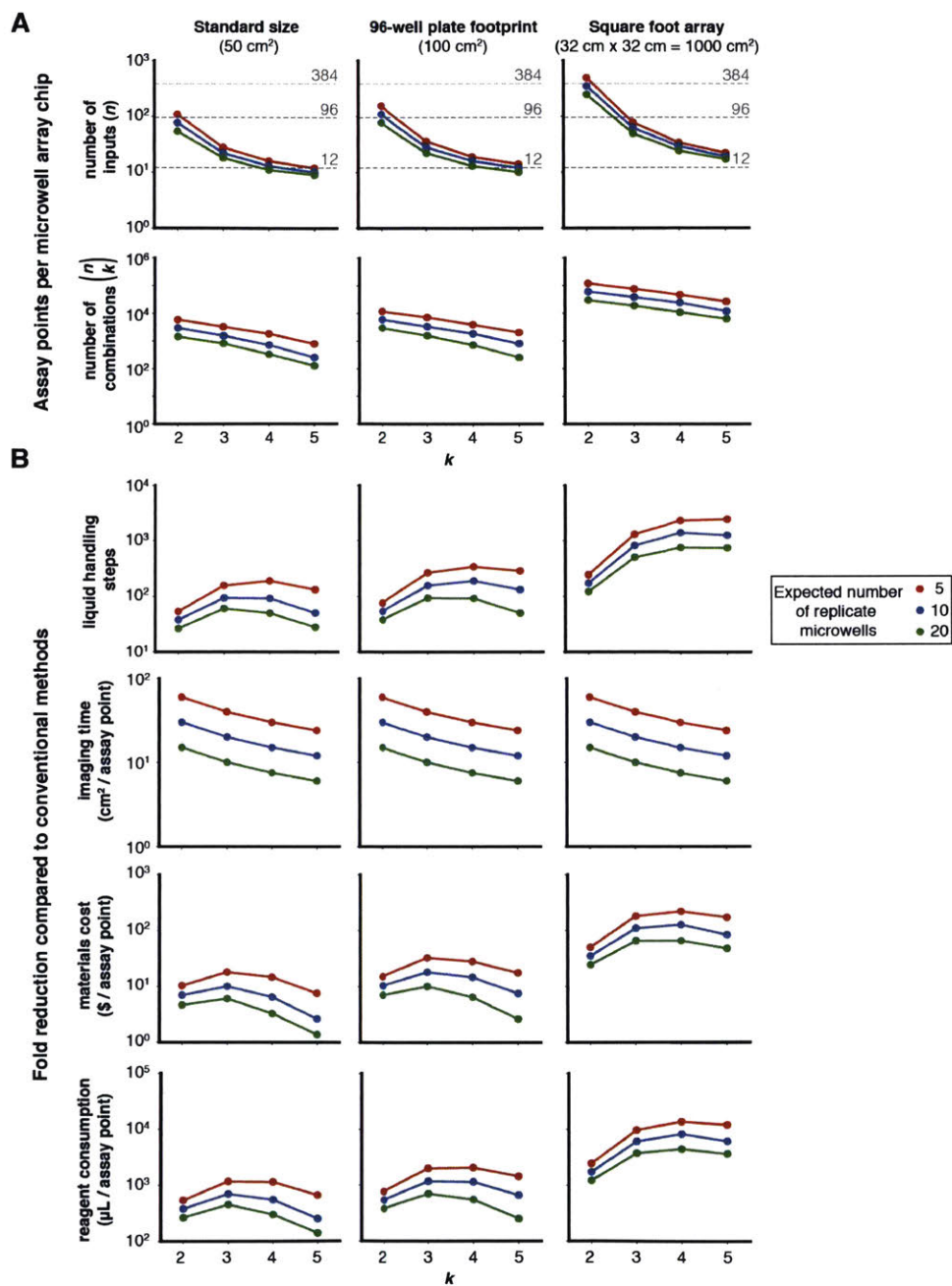


**Figure 2-7. Reductions in liquid handling, costs, and reagent consumption for hypothetical experiments.** (**A**) The maximum number of inputs $n$ and combinations $\binom{n}{k}$, such that the expected number of microwells containing a given set of $k$ droplets is 5, 10, or 20. For reference, numbers of inputs corresponding to commonly used numbers are highlighted (12 = 1 row of 96-well plate, 96 = 1 96-well plate, and 384 = 1 384-well plate). (**B**) Compared to conventional liquid handling in 96-well plates, the fold

reductions in liquid handling steps, imaging time, materials cost, and reagent consumption. Details on modeling and assumptions are provided in Section 2.6.10 with example calculations in Table 2-3 and Table 2-4.

# 2.4.1 Our design improves factors limiting combinatorial experiments by an order of magnitude

In this chapter, we introduced a new platform for combinatorial experiments with the goal of making order of magnitude reductions in liquid handling complexity, costs, and reagent use. We gave an overview of the design and explained how the principles behind each component improve on some limitations of droplet microfluidic platforms.

To evaluate whether this design indeed achieves the goals of improving the factors limiting combinatorial experiments, we can consider hypothetical, abstracted experiments and compare the performance of our platform to conventional liquid handling in 96-well plates. These experiments have three parameters: *(i)* the number of input reagents, $n$; *(ii)* the subset size $k$; and *(iii)* the replication level (Figure 2-7A). In each case, the goal of the experiment is to assemble all $\binom{n}{k}$ combinations at the desired replication level. We examine three replication levels (5, 10, and 20), as different applications can tolerate different levels of assay noise (for example, see Chapter 3 Figure 3-1E). For comparison to conventional methods, we consider constructing all combinations in 96-well plates by conventional liquid handling, in duplicate. To examine the scaling relationships, we will assume three microwell array sizes: *(i)* the "standard" size (50 cm$^2$, used throughout this thesis); *(ii)* a 96-well plate footprint (100 cm$^2$); and *(iii)* a hypothetical "square foot" array (1000 cm$^2$). The 96-well plate footprint is a realistic design goal that would maintain interoperability with current laboratory instruments and robotics standardized to this format. The square foot array could be considered as 10 96-well plate footprint arrays run in parallel, or an eventual design target for a custom instrument. For each microwell array size and value of $k$, Figure 2-7A shows the maximum number of inputs $n$ such that $\binom{n}{k}$ combinations can be constructed at each replication level (see Sections 2.6.2 and 2.6.10 for derivations).

Figure 2-7B shows the fold reduction in liquid handling steps, costs, and reagent consumption in each of the experimental scenarios. In all cases, liquid handling steps are reduced by at least an order of magnitude,

peaking at 100-fold reductions for the standard size array and even larger reductions for larger arrays. To compare costs, we break down contributing factors by category (liquid handling, imaging time, materials cost, and reagent consumption), as any factor could dominate for a given application. Across most factors, a >10-fold reduction can be achieved, but the material costs reduction is bounded by droplet production costs (fluorous oil, fluorosurfactant, and plastic consumables, *e.g.* Bio-Rad QX200 cartridges which currently cost $1/input). In applications where these costs dominate, they might be managed by splitting droplet volumes across multiple microwell array chips. These costs could also continue to fall with economies of scale as droplet platforms gain popularity across the life sciences. Lastly, reagent consumption is greatly reduced in all cases, which may be of tremendous value for applications that require high-value chemicals such as rare natural products.

## 2.4.2 Limitations

*Scalability*

The overall scale of experiments on a single chip (Figure 2-7A) is limited by the maximum array size, imposed by fabrication limits as well as the total scan area available on a conventional microscope stage. Experiments that are larger than those described in Figure 2-7A must therefore be divided across multiple chips (as done in Chapter 3; see Section 2.6.10 for more discussion). A modest increase (~10-fold) could be achieved by increasing the microwell density in the array, and perhaps by making droplets smaller, but the volume of droplets likely cannot be significantly reduced below 1 nL in applications that involve cell culture due to density limits. Ultimately, these limits might be circumvented by fabricating microwells into a reeled, contiguous film that can be continuously unspooled and passed over an optical sensor.

Additionally, while the parallel processing of droplets increases accessibility and robustness relative to a serial processing approaches, it moderately sacrifices throughput. For the droplet sizes used here, serial droplet microfluidic devices have been reported merging and sorting of droplets at rates up to 200 droplets / s [52], [83]. At current microwell densities, our platform could achieve the same throughput at 0.17 cm$^2$ / s imaging rate, which is about five-fold faster than we currently achieve in practice. Faster imaging could be easily achieved with higher concentrations of encoding dye to reduce camera exposure times, higher microwell densities, faster microscope stage movement speeds.

The design choice to randomly construct combinations introduces another limitation because some combinations between the inputs might be undesired. For example, in constructing pairwise combinations of a library of drugs across a library of cell lines, the microwell array will also construct combinations of *(i)* two drugs with no cells, and *(ii)* two cells with no drugs. While this results in only a 50% inefficiency for pairwise combinations, in a 3-wise combinatorial screen, only 22% of combinations will have an element of each library. One strategy for overcoming this limitation is to make differently sized droplets that can be captured sequentially. Preliminary data for this approach is presented in Chapter 5 (see Section 5.2.1).

*Generalizability*

While sealing the microwell array after loading improved compatibility for small molecules, one also loses access to the droplets. This limits the assay scope to optical assays. The ability to retrieve droplets from the array for further analysis, would allow DNA, mRNA, protein-based assays that cannot be currently performed optically. To selectively capture droplets from the array, the array could be sealed with a pierceable plastic adhesive rather than glass. This adhesive could be later punctured with a microneedle, aided by a micro-manipulator for accuracy. *(Cheri Ackerman suggested this approach and she is currently developing it)*. This strategy would only support targeted selection of droplets, but maintaining access to all droplets could also useful for a number of applications. For example, later addition of assay reagents such as staining is not currently supported. Feeding and removal of waste products from droplets could also help support longer term cell culture.

# 2.5 Conclusion

Here we introduced a platform for combinatorial experiments using droplet microfluidics. Our approach makes order-of-magnitude reductions to the liquid handling complexity, cost, and reagent consumption that currently limit these experiments. Our design also improves the accessibility, generalizability, and scalability of droplet microfluidic platforms.

# 2.6 Methods and operational guide

This section describes the methods used for experiments in this chapter, and provides a detailed operational guide for our platform.
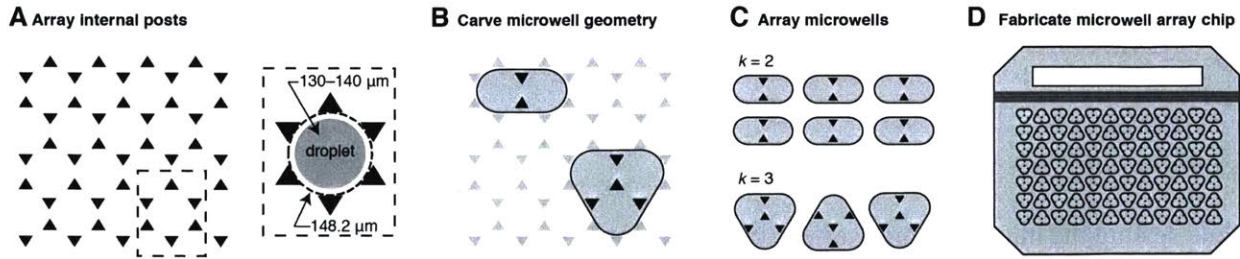


**Figure 2-8. Microwell array design.** (**A**) Triangular posts were arrayed such that each hexagonal arrangement enclosed a space optimized for a single droplet. The diameter of the enclosed space used in all designs was set to 148.2 µm, which was optimized for 135-µm diameter droplets. (**B**) Convex hulls were drawn to encircle internal posts to achieve the desired $k$. (**C**) The microwell designs were arrayed with ~50 µm inter-microwell spacing. (**D**) The arrays were fabricated onto PDMS chips with dimensions compatible with our loading apparatus.

## 2.6.1 Microwell design and fabrication

*Generation 1 microwell array designs were a proof of concept and are provided reference, however all future designs should use Generation 2.*

*Generation 1*

Each microwell consists of two circular geometries (diameter = 148.6 µm) set at 10% overlap by diameter. We arrayed microwells in a hexagonal lattice with 50 µm inter-microwell spacing, across the interior of the 6.2 × 7.2 cm microwell array chip area. This resulted in 43,000 microwells ( Figure 2-2B). Generation 1 microwell arrays typically achieved about 60% loading and merging efficiency (data not shown), compared to 90+% efficiency of Generation 2 designs (Figure 2-3).

*Generation 2*

All microwell array chips consisted of the following design features:

1. An array of microwells of one or more values of $k$, where $k$ denotes the number of droplets each microwell was designed to receive.

2. Internal posts within these microwells designed to *(i)* control the number of droplets entering a microwell; *(ii)* inhibit the entry of large droplets; and *(iii)* prevent exit of droplets once they have entered.

3. At the top of the array, a loading slot in which droplets were injected by micropipette.

4. Just below the loading slot, a series of "moat" channels designed to trap droplets below a given size threshold (here, 90 μm). The joint effect of these moats and posts within microwells creates a "band-pass" filter on droplet size.

Microwell designs to capture $k$ droplets were inductively generated. Designs began with a hexagonal array of triangles positioned at the void spaces in a hexagonal sphere-packing of droplets. We then drew a microwell boundary to enclose a subset of posts in accordance with the desired $k$. The size of droplets can vary based on the viscosity of the aqueous phase and surfactant concentration, so droplet diameters were measured by microscopy to determine the sphere-packing and optimal inter-triangle spacing.

We arrayed the microwells at 50-μm inter-microwell spacing within the chip boundaries (6.2 cm × 7.2 cm). Figure 2-2E shows the number of microwells in the array for each value of $k$. The number of microwells declines with $k$ as the footprint of each microwell increased.

To filter small droplets prior to loading, an array of >15 "moats" was added to the top of each chip. Empirically, we found that the 90 μm-wide moats were optimal.

*Fabrication*

For both Generation 1 and Generation 2, we designed all chips in AutoCAD (Autodesk) and created mylar photomasks (Fineline Imaging). From these masks, we fabricated our designs to 100-120 μm feature height using photolithography on silicon wafers (Microchem SU8-2050). We embedded these wafers into custom molds to create PDMS (Dow Corning Sylgard 182 or 184) chips (by soft lithography), of consistent thickness (0.635 cm) and droplet-loading slot location and size. Chips were then coated with 1.5 μm parylene C by vapor deposition (Paratronix) to inhibit water loss from assay droplets, inhibit compound uptake, and stiffen the chip to prevent interior collapse during droplet loading [49].

## 2.6.2 Expected levels of microwell-level replication of combinations

As combinations are randomly assembled in microwells, experimental designs should consider the total number of microwells expected to contain a given combination of the input reagents. If too many inputs are loaded onto a microwell array chip, some fraction of combinations may not even be observed at all.

Most experiments only consider combinations where each droplet is distinct (e.g. [A, B, C], and not [A, A, C]), therefore we will focus the discussion on this calculation.

To calculate the expected number of microwells that will contain a given combination, we model $N$ total microwells as capturing randomly drawn subsets of $k$ droplets from a set of $n$ droplet types, with replacement. First, consider that the probability of a given microwell capturing any ordered subset of $k$ droplets is $\frac{1}{n^k}$. Then consider the total number of ways to order the subset of interest. Subsets composed of $k$ unique droplets have $k!$ orderings. Therefore, the probability of capturing a distinct subset is $\frac{k!}{n^k}$, and the expected number of microwells for a given unique combination is $N\frac{k!}{n^k}$. As examples, Table 2-3 shows the number of inputs ($n$) such that $N\frac{k!}{n^k}$ is at least 10 for a total array area of 50 cm$^2$ and different values of $k$, with more generalized results Figure 2-7A.

The distribution of microwells containing a given combination should follow a Poisson distribution with mean $\lambda = N\frac{k!}{n^k}$, assuming that the droplets are equally loaded and well-mixed. This fact may be useful for limiting the expected fraction of distinct droplet combinations that are replicated across microwells less than a threshold number of times.

## 2.6.3 Fluorescence encoding

To encode reagents in droplets, we use distinct ratios of three fluorescent dyes (Alexa Fluor series, Thermo Fisher Scientific). All ratios were generated to have the same final total dye concentration of 1 μM, with concentration of each component dye varied. The dyes used here are Alexa Fluor 555, 594, and 647, however we expect that the performance should not depend on the exact dyes chosen as long as they are distinguishable given the filter sets available on a user's fluorescence microscope.

44

We prepared stock codes at 10-50X concentration in 96-well plates in water. At the point of each experiment just before making droplets, we selected the codes to use and mix them with reagents to 1 μM final concentration.

*Derivation of codes and total encoding complexity*

The number of codes that can be generated, or encoding complexity, can be derived given the number of discrete signal levels $S$ and number of dyes $d$. All codes have the same total signal $S$, composed of a given number of discrete "slots" assigned to each dye such that the total number of slots is set to $S$. The approach to calculating the number of codes generated by this scheme is commonly known as "stars and bars combinatorics", and is equal to $\binom{S+d-1}{d-1}$. Table 2-2 shows the number of codes for given numbers of $S$ and $d$. Codes used throughout this thesis are from the set of $S=10$ and $d=3$, which yields 66 total codes.

# 2.6.4 Droplet production

To produce droplets, 20 μL of each input-dye mixture were transferred via multichannel micropipette to Bio-Rad QX200 cartridges to produce 20,000 1-nL droplets (continuous phase: fluorocarbon oil 3M Novec 7500 with 0.5-2% w/w RAN Biotech 008 FluoroSurfactant) using the Bio-Rad QX200 instrument (3 min / cartridge of 8 each) or a custom aluminum pressure manifold (1.5 min / 6 cartridges of 8 each). This process requires less than 30 minutes to emulsify all wells in a 96-well plate.
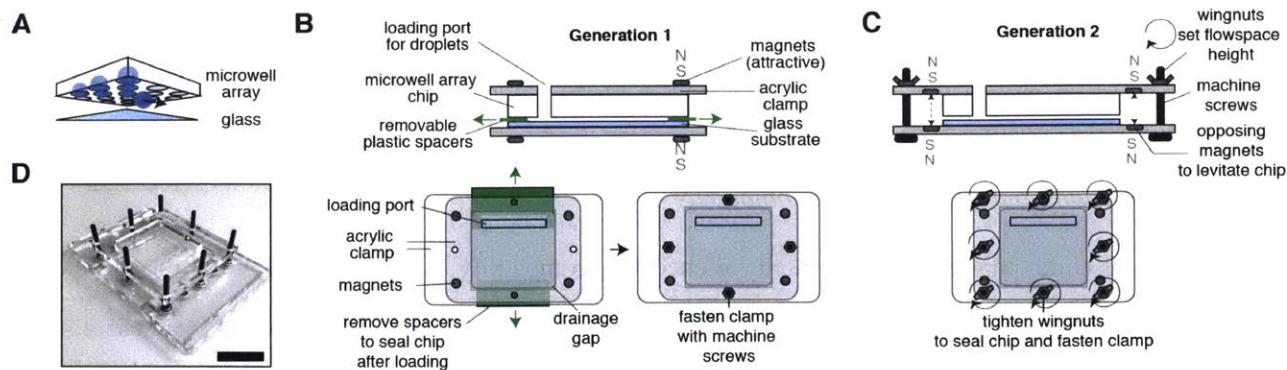
**Figure 2-9. Microwell array chip loading**. (**A**) To load droplets into microwells, we invert the chip and flow droplets underneath such that their buoyancy in the fluorous oil drives them into microwells. (**B**) To suspend the microwell array chip, in Generation 1, we used two removable plastic spacers. (**C**) Generation 2 simplified this design by magnetically levitating the microwell array chip. Opposite-facing magnets were embedded in the top and bottom pieces of the acrylic housing to levitate the top piece to which the microwell array chip adheres. Machine screws are then used to set the top piece at the desired height for loading, or afterwards, to clamp the chip to the glass substrate and seal the array. (**D**) A photograph depicts the Generation 2 microwell array assembly. The scale bar represents approximately 4 cm.

## 2.6.5 Microwell array chip setup and loading

Microwell array chips are loaded in three steps:

1. We pool the droplets carrying the different inputs
2. To load the microwells, we flow the droplets underneath the inverted microwell array
3. We wash and clamp the microwell array to the glass substrate

Just before loading a chip, a fraction (*e.g.* 4 µL) of each set of droplets was pooled by multichannel micropipette into a single well or microcentrifuge tube (5 min) (to total aqueous volume 200 µL, or ~200,000 droplets, per chip).

To load, we invert the chip and use the buoyancy of the droplets in the surrounding fluorous oil to drive the droplets into microwells (Figure 2-9A). We constructed a loading apparatus consisting of a top and bottom acrylic piece that aid to suspend the microwell array above a glass substrate during loading, and after, clamp the microwell array to the glass to seal the chip. The glass substrate piece is custom-cut from large glass

slides (Brain Research Laboratories; 1.2 mm thickness) and made hydrophobic via pretreatment with Aquapel (a fluoro-silane).

In Generation 1 (Figure 2-9B), we suspended the microwell array chip over the glass using plastic spacers (height = 250 μm). The chip was held in place within the assembly via its spontaneous adhesion to the top acrylic piece; the two halves of the assembly were held in place via neodymium magnets. After loading was complete, we then removed the plastic spacers and fastened the clamp using machine screws.

In Generation 2 (Figure 2-9C), we instead relied on magnetic levitation of the microwell array chip. Both acrylic pieces contained four neodymium magnets oriented such that the two acrylic pieces repelled. The We then adhered the non-parylene-coated top side of the microwell array chip to the top piece of the acrylic by pressing the PDMS against acrylic to form a vacuum. The the top piece was lowered toward the bottom piece via tightening the wingnuts to counteract the magnetic repulsion until the desired flow space between the glass and microwell array chip was attained (~500-700 μm). In this setup, after loading was complete, we clamped the chip to the glass simply by tightening the wingnuts.

In both generations, to load the chip, we first filled the gap between the chip and the glass using 0% w/w surfactant oil. The pooled droplets were then injected into the loading port using a micropipette, with draining oil recycled to sweep excess droplets away (5 mins). After loading was complete, the chip was washed with oil (0% w/w surfactant) to deplete residual surfactant, and clamped according to the methods described above. All operations are performed with a standard P200 or P1000 micropipette.

## 2.6.6 Microscopy, image analysis, and fluorescence decoding

All fluorescence microscopy was performed using a Nikon Ti-E inverted fluorescence microscope with fluorescence excitation by a Lumencor Sola light emitting diode illuminator (100% power setting). Images were taken across four fluorescence channels for GFP (Semrock GFP-1828A) and the three encoding dyes, Alexa Fluor 555 (Semrock SpGold-B), 594 (Semrock 3FF03-575/25-25 + FF01-615/24-25), 647 (Semrock LF635-B). Images were collected by a Hamamatsu ORCA-Flash 4.0 CMOS camera (exposure times range 50ms – 500ms) at 6.5 μm/pixel resolution achieved by 2X-4X optical magnification. The exposure timing was dictated by the magnification and pixel binning. The total scanning time for 2X and 4X magnification were 12 minutes and 20 minutes, respectively.

We developed an image analysis pipeline to:

1. Identify droplets as circular objects within the image

2. Decode the contents of each droplet based on the fluorescence code

3. Assign each droplet to a microwell

To detect each droplet in the image, we average all fluorescence channels and apply a circular Hough transform (scikit-image) to detect circular objects with a diameter of 100–140 μm.

To decode each droplet's fluorescence code, we measure the average fluorescence intensity of each dye (a 3-dimensional vector for each droplet). These vectors are then projected onto a two-dimensional plane, eliminating systematic effects from differences in illumination (Figure 2-4D). The DBSCAN algorithm (scikit-learn) identifies the clusters of droplets corresponding to each input condition. Optionally, a user can correct clustering errors, such as cluster collisions caused by optical activity of reagents in the input library. A quality score for each droplet can be computed based on the distance to the assigned cluster centroid (Figure 2-4E, F). The Hungarian algorithm (scikit-learn) then maps each cluster to the pre-determined centroids of each dye mixture. Pre-determined centroids can typically be set by *a priori* ratios of dyes. Alternately, to account for dye shifts caused by optical activity of reagents, each input-dye mixture can be imaged prior to emulsification to predict effects on the fluorescence of the resultant droplets and establish an alternative centroid for affected dye mixtures.

Once identified and decoded, we use two strategies to assign droplets to microwells in the array. Generation 1 chips only consist of $k=2$ microwells. We infer that a pair of droplets shared a microwell if the distance between their centroids along the vertical microwell axis is less than an adjustable distance threshold, typically set to 162.5 μm. Generation 2 chips consist of microwells with variable sizes, which complicates this approach. Therefore, we compute the optimal alignment between [the centroid positions of all droplets] and [the photomask design used to construct a given microwell array chip]. After alignment, we infer droplets share a microwell if their centroids aligned to the same microwell in the photomask.

## 2.6.7 Electro-coalescence of droplets

We merged the droplets to mix the reagents in each microwell by applying an AC electric field (4.5 MHz, 10,000-45,000-volt source underneath glass slide supplied by corona treater (Electro-Technic Products), for ~10 seconds of exposure during which the tip of the corona treater was moved below the glass surface).

# 2.6.8 Methods for loading and merging efficiency measurements

To measure the efficiency of microwell array loading and merging (Figure 2-3), we constructed microwell array chips with microwell sizes ranging $k=\{1, 2, \ldots 7; 19\}$, segmented in columns on the chip. To test the impact of internal post features, we used a total of four normal chips and two chips without posts. We loaded the chips using the above methods with a set of 1-nL droplets of M9BSA media (our base media for Chapter 4; 1X M9 salts (Teknova), 1X Trace metals (Teknova), 0.1 mM calcium chloride, 2 mM magnesium sulfate, 0.05% w/v BSA) in Novec 7500 oil (3M) + 2% w/w fluorosurfactant (RAN Biotech, 008-Fluorosurfactant). After loading, we imaged and merged the chips according to the methods above. Chip #4 was not merged due to an experimental error.

To measure loading efficiency, we used the above described image analysis methods to identify the number of droplets in each microwell of size $k$.

To determine merging efficiency, we analyzed images of the merged droplets to calculate a median merged droplet size for correctly loaded microwells of each value of $k$. This analysis yielded a "standard curve" of merged droplet sizes. We then compared the merged droplet sizes for all microwells to the standard curve. If a merged droplet size for a microwell of $k$ droplets was closest to the standard for size $k$, we assign it "correct," and "incorrect" otherwise. Standard curves could not be constructed for $k=19$ because we did not construct microwells of $k=18$ or $k=20$, therefore merging efficiency for $k=19$ is not reported.

# 2.6.9 Methods for resorufin exchange measurements

This experiment used Generation 1 microwell array chips with $k=2$ microwells.

To construct source droplets, we emulsified resorufin (10 µM) in Cation-Adjusted Mueller Hinton Broth (CAMHB) using 2% w/w 008-FluoroSurfactant (RAN Biotech) in Novec 7500 fluorocarbon oil (3M) using Bio-Rad QX200 cartridges. Sink droplets were made in a similar fashion, but with fluorescein (5 µM, CAMHB), as this dye showed negligible exchange on assay timescales [59], [80]. Droplets containing resorufin or fluorescein were pooled in a 1:1 ratio by micropipette in a microcentrifuge tube (5 min) and then loaded into the chip (5 min) such that microwells received either two sink droplets (sink-only wells), two source droplets (source-only wells), or one sink and one source droplet (Figure 2-5A). The random loading process resulted in these pair types being randomly dispersed across the array. We washed the chip

with oil containing either 2%, 0.5%, or 0% w/w surfactant, and then mechanically clamped the chip to the glass substrate according to our standard protocol.

Resorufin fluorescence measurements of the sealed array were taken over 20 hours at three distinct fields of view. Sink droplets were identified by their high fluorescein fluorescence, and assay background was subtracted from all measurements. To measure inter-well exchange, we compared the mean resorufin fluorescence of microwells containing two source droplets and microwells containing two sink droplets (normalized to their sum). As a proxy for bulk emulsion systems and to predict exchange during the pooling phase of our protocol, we compared the mean resorufin fluorescence of source droplets and sink droplets in microwells containing one source droplet and one sink droplet (normalized to their sum).

We modeled exchange of compounds during droplet pooling as a permeation process, following Skhiri *et al.* [59]. If $C_0$ and $C_1$ represent the concentration of resorufin in a source and sink droplet respectively:

$$\frac{dC_0}{dt} = -\frac{1}{2}a(C_0 - C_1)$$

$$\frac{dC_1}{dt} = \frac{1}{2}a(C_0 - C_1)$$

$$\frac{d\left(\frac{C_1}{C_1 + C_0}\right)}{dt} = a\left(\frac{1}{2} - \frac{C_1}{C_1 + C_0}\right)$$

$$\frac{C_1}{C_1 + C_0} = \frac{1}{2}(1 - e^{-at})$$

Here $a$ is a rate constant that represents surfactant reverse-micelle diffusivity, the distance between droplets, the interfacial area, and other transport parameters. Therefore, in Figure 2-6B we fit the timepoints at <3 hours of the resorufin fluorescence of the sink droplet using this equation and obtained the rate constant $a$ = 0.0066 min⁻¹.

To extrapolate these measurements to a bulk emulsion system, we assumed $a$ depends linearly on the interfacial area [59]:

$$\frac{C_1}{C_1 + C_0} = \frac{1}{2}(1 - e^{-ant})$$

where $n$ represents the number of neighboring droplets ($n=1$).

50

## 2.6.10    Modeling assumptions for reduction in liquid handling steps, costs, and reagent consumption

Example calculations for each section are shown in Table 2-3 and Table 2-4.

*Hypothetical experiment sizes*

In these experiments, we consider a fixed microwell array size (50 cm², 100 cm², or 1000 cm²), for microwells designed to merge $k$=2, $k$=3, $k$=4, or $k$=5 droplets. We assumed a constant density for $k$=1 microwells of 1,200 microwells / cm² such that a 50 cm² chip had 60,000 $k$=1 microwells. Since larger microwells take up more area, we made commensurate reductions in the number of microwells over this fixed area. Therefore, we assumed densities of 1,200, 600, 400, 300, and 240 microwells / cm² for $k$=1, 2, 3, 4, and 5 respectively. Note that these densities are approximate and underestimate the true number of microwells for two reasons. First, here we just divided the starting density of 1,200 microwells / cm² by the well size $k$, but we can see that this underestimates the density given by real microwell numbers achieved in Figure 2-2. Second, although 50 cm² is the total chip footprint, microwells are present on only a fraction of the chip, due to the loading slot and trenches, and the microwell fraction of the total footprint is higher for larger chip sizes. However, we expect our modeling results should not depend strongly on taking these factors into account.

For each value of $k$ and microwell array size (50, 100, and 1000 cm²), we report the number of inputs ($n$) to achieve a total number of expected replicates greater than a threshold (5, 10, or 20; given by $N\frac{k!}{n^k}$, derived in Section 2.6.2) (Figure 2-7A).

Applications that require more inputs than can be processed on one chip can be addressed in two ways: *(i)* "aggregation"; or *(ii)* "batch processing."

First, in an aggregation strategy, multiples chips that receive the same inputs can be aggregated together as one total microwell array. This strategy should consider the throughput of processing microwell array chips, and the "assay time window" during which microwells across different chips are assumed identical (for example, an assay time window based on microbe doubling times for growth-based assays might be <1 hour). Controls can also be used to normalized values across chips. This strategy preserves the reductions in liquid handling steps, imaging time, material costs, and reagent consumption computed here.

In a batch processing strategy (employed in Chapter 3), each chip (with $k=k$ microwells) receives a subset $n_{chip}$ of the total $n_{total}$ inputs. To comprehensively sample all $\binom{n_{total}}{k}$ combinations, one can split $n_{total}$ into $b$ batches of size $\frac{n_{total}}{\binom{n_{chip}}{k}}$. Each chip receives $k$ batches (total $n_{chip}$ droplets per chip), and sampling all combinations requires $\binom{b}{k}$ chips. This strategy does not achieve the same reductions modeled here because measurements occur with efficiency $\frac{k!}{k^k}$, $i.e.$ 50% efficiency for $k=2$ combinations, 22% efficiency for $k=3$, 9% efficiency for $k=4$, and 4% efficiency for $k=5$.

*Liquid handling steps*

In the case of the microwell array, the total number of liquid handling steps required is three steps per input ($3n$): *(i)* transfer of encoding dyes; *(ii)* transfer to droplet production cartridge; *(iii)* transfer from droplet production cartridge to droplet pool.

To assemble $\binom{n}{k}$ combinations in 96-well plates in duplicate, the total number of liquid handling steps is assumed to be $\binom{n}{k} \times (k+1)$: *(i)* assembling each combination requires $k$ transfers; *(ii)* duplicating each assembled combination requires 1 transfer.

In comparing costs, we assumed a fixed cost / liquid handling step on both platforms.

*Imaging time*

To compare the costs of imaging the microwell array and 96-well plate, we assumed fixed cost / time (*i.e.* the amortized capital cost of the instrument / instrument life time) and fixed time / scan area / scan channel. Then to compare platforms, we compute the required scan area and number of channels per "assay point" (each combination).

On the microwell array, the scan area per assay point is given by the microwell density and the desired replication level of each experiment. The microwell array also requires 4 channels (3 for droplet decoding; 1 for the later optical assay).

The 96-well plate requires 2 wells (2 × ~1 cm² per well) for each assay point (due to the duplication requirement).

*Materials costs*

We compare the materials cost per assay point of each platform.

Each microwell array chip yields $\binom{n}{k}$ assay points. To calculate the cost of operating the microwell array, we fix droplet production costs at \$1 / condition (Bio-Rad QX200 cartridges; fluorosurfactant; oil) and \$10 / microwell array chip. Therefore the cost per assay point is $(n+10) / \binom{n}{k}$.

For 96-well plates, we assume each 96-well plate costs \$10, and each assay point requires 2 wells (due to the duplication requirement). Therefore the cost per assay point is \$0.21.

*Reagent consumption*

Similarly, we compare the reagent consumption per assay point on each platform.

The microwell array chip yields $\binom{n}{k}$ assay points and requires 20 μL of each reagent input for droplet production. Each reagent is present in $\sim\frac{\binom{n}{k}}{n}$ combinations, therefore the reagent consumption per assay point is $20n$ μL $/ \binom{n}{k}$.

In 96-well plates, we assume each assay point requires 100 μL per well and is measured in duplicate, requiring 200 μL total.

**Table 2-3. Hypothetical experiment sizes for 50 cm² microwell array and 10 replicate microwells per combination.** Hypothetical combinatorial experiments in Figure 2-7A are based on three parameters, the number of inputs $n$, the subset size $k$, and the desired replication level. Given a microwell array area and value of $k$, we found the maximum number of inputs $n$ to achieve the desired replication level. Here we show example calculations for a microwell array area of 50 cm² and desired replication level of 10 microwells. Derivation for the expected number of replicates is provided in Section 2.6.2.

| Microwell size $k$ | Number of microwells $N$ (50 cm² array) | Number of inputs $n$ | Expected replicates per combination $N\frac{k!}{n^k} > 10$ | Number of combinations $\binom{n}{k}$ |
|---|---|---|---|---|
| 1 | 60,000 | 6,000 | 10 | 6,000 |
| 2 | 30,000 | 77 | 10.1 | 2,926 |
| 3 | 20,000 | 22 | 11.3 | 1,540 |
| 4 | 15,000 | 13 | 12.6 | 715 |
| 5 | 12,000 | 10 | 14.4 | 252 |

**Table 2-4. Calculations for reductions in liquid handling steps, imaging time, material costs, and reagent consumption for $k=2$ 50 cm² microwell array with 10 replicates.** Figure 2-7B shows reductions in each of these components for all hypothetical experiments. As an example, here we show the calculations corresponding to the $k=2$ 50 cm² microwell array with 10 microwell replicates.

| Component | 96-well plate (*77 choose 2*) (2 replicates) | Microwell array (*k = 2, n = 77*) (10 microwell replicates) | Fold reduction |
|---|---|---|---|
| **Liquid handling steps** (assume fixed cost / step) | $8.8 \times 10^3$ steps <br> $(2 + 1)\binom{77}{2}$ steps | $2.3 \times 10^2$ steps <br> $3 \times 77$ steps | $3.8 \times 10^1$ |
| **Imaging time** (assume fixed cost / time) <br> (time = time / area (fixed) × area / assay point × channels) | $10^0$ cm² / well <br> × 2 wells / assay point <br> × 1 channel | $1$ cm² / ( $0.6 \times 10^3$ microwells) <br> × 10 microwells / assay point <br> × [3 (decoding) + 1 (second scan)] channels | $3 \times 10^1$ |
| **Material costs** (cost) | $2.1 \times \$10^{-1}$ / assay point <br> ($\$10$ / 96-well plate) | $\$3.0 \times 10^{-2}$ / assay point <br> ($\$10$ microwell array chip <br> + $\$1 \times 77$ droplet production <br> yields $\binom{77}{2}$ assay points) | $7 \times 10^0$ |
| **Reagent consumption** (assume fixed cost / volume) | $2 \times 10^2$ µL / assay point <br> (100 µL / well) | $5.3 \times 10^{-1}$ µL / assay point <br> (20 µL / droplet production <br> yields $\frac{\binom{77}{2}}{77}$ assay points) | $3.8 \times 10^2$ |

# Chapter 3

# Combinatorial drug discovery in nanoliter droplets

*This chapter is reproduced from Kulesa, Kehe, et al. Proceedings of the National Academy of Sciences, 2018* [68].

*This work was performed in collaboration with Jared Kehe, Juan Hurtado, and Prianca Tawde. Jared and I performed many of the experiments to establish the proof of concept together. The final screening efforts were carried out together by Jared, Juan, and I. Prianca assisted us throughout much of this work, including by designing a custom instrument for droplet production and help with materials preparation. Deepan Thiruppathy, our summer student, also assisted throughout. The original concepts behind identifying drug combinations to overcome antibiotic resistance were introduced to our lab by Stewart Fisher, and developed in collaboration with David Feldman and Navpreet Ranu.*

## 3.1 Abstract

Combinatorial drug treatment strategies perturb biological networks synergistically to achieve therapeutic effects and represent major opportunities to develop advanced treatments across a variety of human disease areas. However, the discovery of new combinatorial treatments is challenged by the sheer scale of combinatorial chemical space. Here we report a high-throughput system for nanoliter-scale phenotypic screening that formulates a chemical library in nanoliter droplet emulsions and automates the construction of chemical combinations *en masse* using parallel droplet processing. We apply this system to predict synergy between more than 4,000 investigational and approved drugs and a panel of 10 antibiotics against *E. coli*, a model Gram-negative pathogen. We found a range of drugs not previously indicated for infectious disease that synergize with antibiotics. Our validated hits include drugs that synergize with the antibiotics

vancomycin, erythromycin, and novobiocin, which are used against Gram-positive bacteria but are not effective by themselves to resolve Gram-negative infections.

## 3.2 Introduction

Much of modern drug discovery acts to modulate a specific drug target using a single agent with maximally selective effects, arising from the idea of Paul Ehrlich's "magic bullet" [84]. However, the prevalence of redundancy, feedback, and multi-functionality in biological networks challenges this approach [69]–[71]. Therapeutic strategies comprising multiple drugs in combination have been proposed to exploit network-driven interactions to achieve the desired functional perturbation, reduce toxicity, and prevent or overcome drug resistance [69]–[73]. In particular, combination antimicrobial treatments that overcome drug resistance by targeting known resistance elements (*e.g.* beta-lactamase enzymes) in addition to essential targets make up a substantial fraction of antibiotic treatments in clinical development today [85].

Despite the applicability of novel drug combinations, their identification by high-throughput screening has been slowed by the high complexity, cost, and compound consumption of conventional screening methods [74]. For example, testing all pairs of drugs from a modest library of 2,000 drugs (*e.g.* FDA approved drugs) requires almost 2 million pairwise combinations, and far more if compounds are titrated. Experiments of this scale are currently restricted to specialized labs and facilities that can accommodate the large costs and complexity (total liquid handling steps, logistics of plate layout and workflow design). Additionally, since these screens test each compound across thousands of others, thousands of times the compound quantity is required compared with single-compound screening, which can deplete an entire chemical inventory in a single screening experiment. Current methods for combinatorial discovery work around these issues, either through computational predictions of drug synergies to reduce screening scale or combining multiple tests in pools with subsequent deconvolution [86]–[88].

Here we introduce a strategy for combinatorial drug screening based on droplet microfluidics that unlocks order-of-magnitude improvements in logistical complexity and compound consumption and reduces the need for capital equipment. Through miniaturization and high-speed processing, advances in droplet microfluidics are making major impacts across the life sciences, such as allowing the measurement of 1,000+ single-cell morphological [54] and transcriptomic phenotypes [47], or high resolution and low cell-input drug dose response testing [52], [43], [53], [61], [62], [89]. Our platform leverages the throughput

potential of such microfluidic and microarray systems [54], [90]–[92], and substitutes deterministic liquid handling operations needed to construct combinations of compounds with spontaneous merging of random pairs of droplets in parallel inside a microwell array device (Figure 2-1) [93]. We used this device to screen compound combinations for bacterial growth inhibition in nanoliter droplets, demonstrating its manual operation at high throughput without robotic liquid handling.

# 3.3 Results and Discussion

Using Generation 1 microwell array chips described in Chapter 2, our platform constructs and assays all pairwise combinations of a set of input compounds. We first combine concentrated compounds with fluorescent encoding dyes (unique ratios of three fluorescent dyes), cells, and media, from which we produce 1-nL aqueous droplets in a fluorocarbon oil and stabilizing fluorosurfactant. To construct combinations, we pool and load the droplets into an array of Generation 1 $k=2$ microwells. Pairwise compound combinations are thus constructed automatically by droplet merging, considerably reducing the number of liquid handling steps required (see Chapter 2, Figure 2-7).

A challenge in droplet microfluidics that has limited cell-based compound screening is the exchange of compounds between droplets on assay-relevant timescales [56], [59], [60], [80]. Compound exchange is mediated by the dynamic equilibrium of surfactant molecules between the aqueous-oil droplet interface and reverse-micelles in the oil phase [59], [80]. In a screening context, this creates the potential for false negatives resulting from compound loss from droplets and false positives resulting from the exchange of active compounds among droplets [56]. We reasoned that our platform could limit the extent of false positives caused by cross-contamination during the longer incubation step due to the confinement of droplets in microwell compartments, and the depletion of surfactant after loading. Indeed, in Chapter 2, Section 2.3.4 we showed that these two factors reduced exchange of the refence compound resorufin after microwell loading to levels below our detection limits (Figure 2-5). Though some compounds can exchange more quickly than resorufin and may exchange significantly during the droplet pooling phase prior to loading [80], [94], these compounds would likely be diluted below active concentrations across many other droplets. The low false positive rate of the screen (described below) and further analysis of our screening hits (Figure 3-5) show that these fast-exchanging compounds (presumably present in our compound library

of drugs and drug-like molecules) do not need to be identified and removed prior to screening (for more discussion, see Section 3.6, and Figure 3-5).
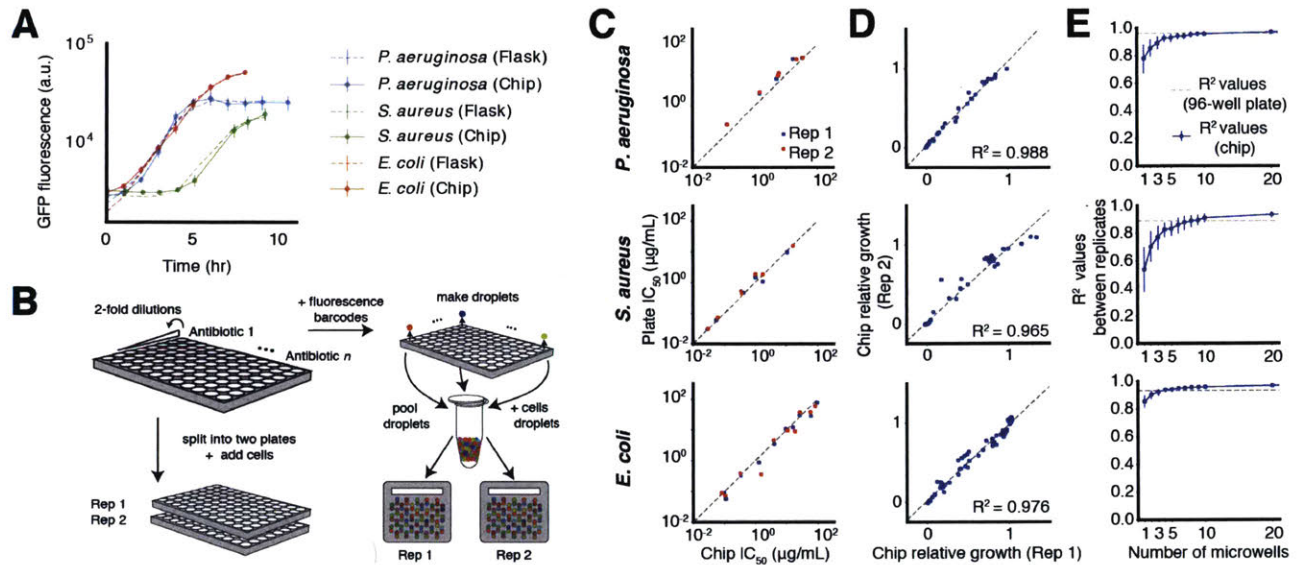


**Figure 3-1. Characterization of growth inhibition assay.** (**A**) We measured cell growth by monitoring accumulation of constitutively expressed GFP in both conventional Erlenmeyer flasks (dotted lines) and the droplet platform (solid lines). Error bars represent standard deviations of microwell measurements. Measurements from Erlenmeyer flask cultures are linearly transformed to the same scale as microwell measurements. (**B**) Experimental setup for comparing antibiotic response curves and measuring technical noise in 96-well plate broth culture format and the droplet platform. (**C**) Estimated $IC_{50}$ for each antibiotic compared between 96-well plate and droplet platform formats. Dotted lines show the diagonal. (**D**) Comparison of two technical replicates on the droplet platform of growth values at particular antibiotic dosages normalized to a media-only control. Dotted lines show line of best fit. (**E**) Relationship between microwell-level replication and technical noise, estimated by bootstrap resampling of the data in part D. Error bars represent 10-90th percentile bootstrapped $R^2$ values. Dotted lines represent $R^2$ values between technical replicates in 96-well plates.

60

# 3.3.1 Droplet-based growth inhibition assays show fidelity to conventional methods and have high data quality

As a first application of our platform, we developed fluorescence-based growth inhibition phenotypic screening assays for three model bacterial pathogens often used in antibiotic discovery, *Pseudomonas aeruginosa*, *Staphylococcus aureus*, and *Escherichia coli* [62], [89]. For each organism, we compared growth dynamics, antibiotic drug responses, and reproducibility of the droplet platform with conventional Erlenmeyer flask and 96-well plate broth culture methods (Figure 3-1). Growth dynamics (monitored by constitutive GFP fluorescence) between Erlenmeyer flasks and the droplet platform showed close correspondence, indicating no detectable toxicity or gross physiological impact on the bacteria (Figure 3-1A). We chose 6-12 antibiotics representing different chemical classes and mechanisms of action, and compared $IC_{50}$ values estimated from five-point dose response curves measured with the droplet platform and the same fluorescence assay in a 96-well plate broth culture format (Figure 3-1B; Figure 3-6, Figure 3-7, Figure 3-8). Overall, culture plates and the droplet platform indicated similar potency for each antibiotic and comparable levels of assay noise ($R^2$ values between technical replicates) (Figure 3-1C,D, Figure 3-9).

High-throughput screening is extremely sensitive to assay noise as hits must be enriched with respect to false positives. In the droplet platform, droplets carrying different compounds are paired randomly in microwells, and assay noise is suppressed by making multiple measurements of the same compound pair across replicate microwells. The number of replicate microwells is a random variable with an expected value determined by the number of possible unique input droplet pair combinations and the number of microwells on a given chip (see Chapter 2, Section 2.6.2). To explore this relationship between microwell-level replication and throughput, we down-sampled the number of replicate microwells observed per antibiotic dose and compared measurements from two technical replicate microwell arrays. We observed diminishing improvements at replication levels past 5-10 microwells (Figure 3-1E), which is the approximate level of replication obtained when 64 unique inputs are applied to the Generation 1 microwell array (see Section 3.5.5).
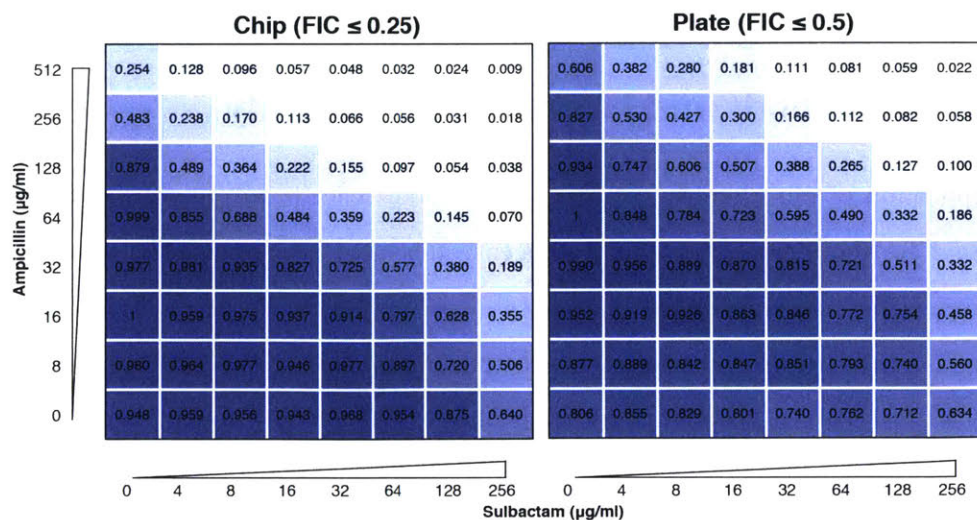
**Figure 3-2. Comparison of checkerboard assay between 96-well plates and microwell array chip.** Comparison of the checkerboard drug interaction assay in *P. aeruginosa* for the antibiotic ampicillin and sulbactam, a beta-lactamase inhibitor and known potentiator. Each point shows a relative growth value normalized to the maximum growth value on the 64-point matrix. Both platforms report a synergistic interaction as described by the FIC index method (FIC index ≤ 0.5).

# 3.3.2 Droplet-based growth inhibition assays detect compound synergy

To evaluate our ability to detect synergy between compound pairs, we tested a canonically synergistic pair, ampicillin (a beta-lactam antibiotic) and sulbactam (a beta-lactamase inhibitor), against *P. aeruginosa* (Figure 3-2). Synergy is commonly assessed by crossing a dilution series of each compound in a "checkerboard" assay matrix and quantifying the deviation of activity levels from a model of independent acting drugs (Bliss synergy) or the Fractional Inhibitory Concentration (FIC) index method [95], [96]. Synergy (defined as FIC index ≤ 0.5) was detected in both 96-well plate broth culture (FIC index ≤ 0.5) and the droplet platform (FIC index ≤ 0.25).
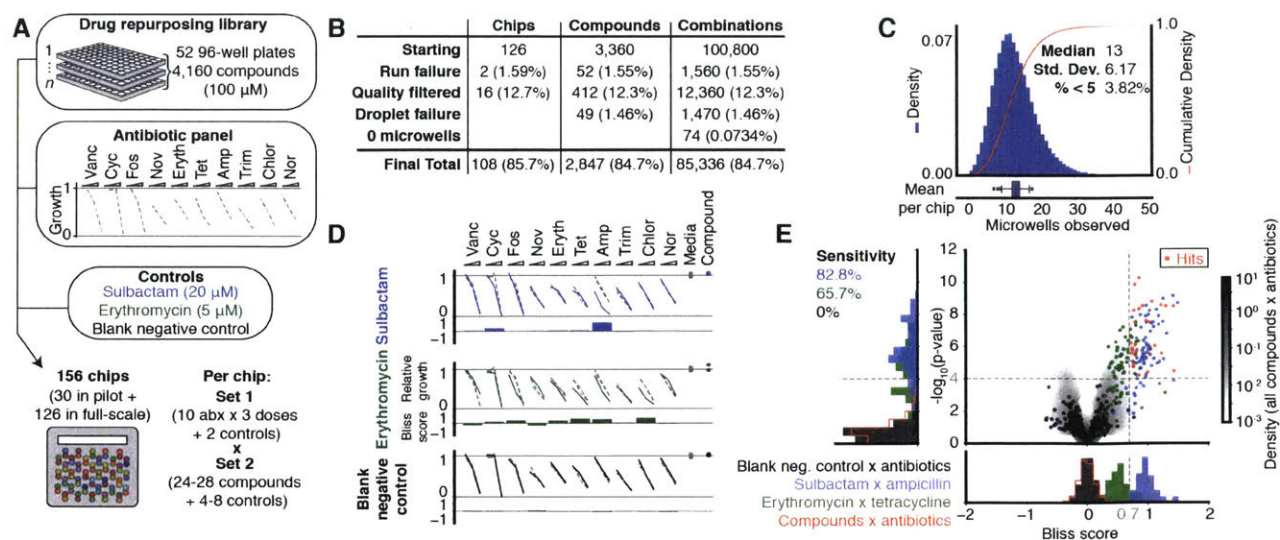
**Figure 3-3. Drug repurposing antibiotic potentiation screen.** (**A**) To measure antibiotic potentiation, we generated three-point dose response curves for ten different antibiotics in combination) with 4,160 compounds (each at single concentration, 100 μM) from a drug repurposing library, as well as positive controls (sulbactam and erythromycin) and negative controls (blank media). Each chip formulated all pairwise combinations of two input sets: (*i*) 3 antibiotics × 10 concentrations + 2 controls (32 total); (*ii*) 24-28 compounds + 4-8 controls (32 total). (**B**) The final numbers of analyzed combinations in the full-scale screening phase, after accounting for losses and quality filtering. (**C**) The histogram (blue bars) and cumulative distribution (red line) of the number of microwells observed for each compound × antibiotic combination. (Bottom panel) Tukey box plot of mean numbers of microwells of all compound × antibiotic combinations on each chip in full-scale phase of screen. (**D**) Representative primary screening data are shown for control compounds. Synergy was identified by comparing antibiotic response curves in the presence of a compound compared to those of the antibiotic alone (gray, dotted), made quantitative by calculating a "Bliss score." At right, the growth in the presence of compound alone ("Compound", colored points), or the absence of antibiotic and compound ("Media", gray points) are shown. (**E**) 28 compound × antibiotic combination hits (red points) were determined by thresholding all compound × antibiotic pairs (gray, shaded contours) on effect size (Bliss score > 0.7, gray dotted line) and statistical significance (p-value < $10^{-4}$, gray dotted line). (Left panel) Projection of vertical axis. Sensitivity to positive controls (blue: sulbactam, green: erythromycin). (Bottom panel) Projection of horizontal axis. Bliss score distributions of positive and negative (black: blank) controls. Histograms are set to 50% opacity to show overlap. Full names of all abbreviated antibiotic names are provided in Table 3-1.

### 3.3.3 We designed a screen to identify drug combinations that overcome intrinsic resistance to antibiotics in Gram-negative pathogens

We next applied our system to identify compounds that can potentiate the activity of antibiotic drugs. In the face of rising antibiotic resistance, efforts to develop new classes of antibiotics have yielded little success [85], [97], [98]. Unfortunately, many antibiotics such as vancomycin, erythromycin, and novobiocin cannot be used to treat important Gram-negative pathogens such as *E. coli*, *P. aeruginosa*, *A. baumannii*, and *K. pneumoniae* due the impermeability of their outer membranes and numerous efflux systems [85], [98]. Previous work suggests that identifying compounds that sensitize drug-resistant pathogens is a promising strategy to broaden the spectrum of existing antibiotics [99]–[101].

We screened for potentiation of a panel of ten antibiotics with diverse mechanisms and biochemical target localizations (each antibiotic titrated across a three-point response curve, Table 3-1) by a "drug repurposing" library of 4,160 compounds against *E. coli* (Figure 3-3A) [100], [102]. This curated library is composed of tool and investigational compounds with extensive preclinical and clinical research data, as well as launched drugs [102]. We reasoned that hits from screening this library may have potential for expedited translation for use in sensitizing Gram-negative pathogens to existing antibiotics [102], [103].

Our analysis focused on determining compound × antibiotic synergies by evaluating a shift of a three-point antibiotic dose response with and without compound, quantified by a synergy metric ("Bliss score") for each compound × antibiotic pair (Figure 3-3A, D). This metric assumes a null model (Bliss) such that if a exposure to *antibiotic A* results in relative cell growth $(1-f_A)$, and *compound B* results in relative cell growth $(1-f_B)$, the expected cell growth under the *compound B* × *antibiotic A* pair is just $(1-f_B) \times (1-f_A)$. Other synergy metrics (Loewe, FIC index) are possible, but we chose this method for its simplicity of interpretation and compatibility with measurements at single compound dosages. The specific choice of synergy metric is not critical, we planned to validate screening hits using checkerboard assays to explore the full interaction landscape and permit quantification through other synergy metrics, such as the FIC index method.

# 3.3.4 We screened 4+ million total microwell assays over 10 days

This screening effort resulted in the construction of 4+ million total microwell assays across 156 microwell array chips, and was completed in 10.3 days in two phases (Pilot phase: 800 compounds, 30 chips, 3.33 days; Full-scale phase: 3,360 compounds, 126 chips, 7 days). With a total of 64 unique inputs per microwell array chip (set 1: 10 antibiotics at 3 dose points + 2 controls; set 2: 24-28 compounds + 4-8 controls), each chip run constructed 720-840 combinations of compound × antibiotic (24-28 compound × 10 antibiotics × 3 dose points), 276-378 compound × compound (1/2 × 24 × 23; 1/2 × 28 × 27), 120-240 control × antibiotic combinations (4-8 controls × 10 antibiotics × 3 dose points), and 48-56 compound × control combinations (24-28 compounds × 2 controls) (Figure 3-3A). Pairwise combinations of antibiotics and controls were also constructed.

We evaluated screening performance from our full-scale phase, comprised of 126 microwell array chip runs and 100,800 compound × antibiotic assay points from 3,360 compounds. Dropout can occur due to chip-run failures, failures to produce, load, and classify droplets, or failure to observe any microwells containing a particular compound × antibiotic combination. Of the 126 chip runs, we had two logistical failures and removed 16 runs due to failed controls to yield a final chip passing rate of 85.7% (108 runs) (Figure 3-3B, Figure 3-10). Droplet production, pooling/loading, or fluorescence code assignment failed for 49 compounds (Figure 3-3B). Overall, of the starting 100,800 compound × antibiotic combinations, 84.7% were successfully measured with an overall median value of 13 replicate microwells (Figure 3-3B, C).

To assess data quality, each chip run was performed with a set of positive (sulbactam × ampicillin; erythromycin × tetracycline) and negative (blank media × all antibiotics) controls to determine the expected sensitivity and false positive rate of the screen (Figure 3-3A, D). The Bliss score distribution of all blank media × antibiotic pairs was well-described by a $t$ distribution, which we used as a null model to calculate p-values for each compound × antibiotic pair (Figure 3-11). To measure sensitivity, each run included one or both positive controls: sulbactam × ampicillin (large effect size, expected Bliss score ~1) and erythromycin × tetracycline (small effect size, expected Bliss score ~0.5) (Figure 3-3D). At an expected false positive rate of $10^{-4}$ (p-value threshold), we recovered 82.8% of sulbactam × ampicillin controls (n=58/70) and 65.7% of erythromycin × tetracycline controls (n=46/70) (Figure 3-3E). To call hits from all the compound × antibiotic pairs, we chose a Bliss score effect size threshold that separated sulbactam ×

ampicillin controls from erythromycin × tetracycline controls (Bliss score > 0.7) (Figure 3-3E). Using these thresholds to score all pairs yielded 28 hit compound × antibiotic pairs (0.098% of total 28,470) from 20 distinct compounds (0.70% of total 2,847) (Figure 3-3E). While we focused analysis on compound × antibiotic pairs, we did identify that one hit compound, pasireotide, also synergized with tedizolid, another compound in the repurposing library run on the same microwell array chip (Figure 3-12).
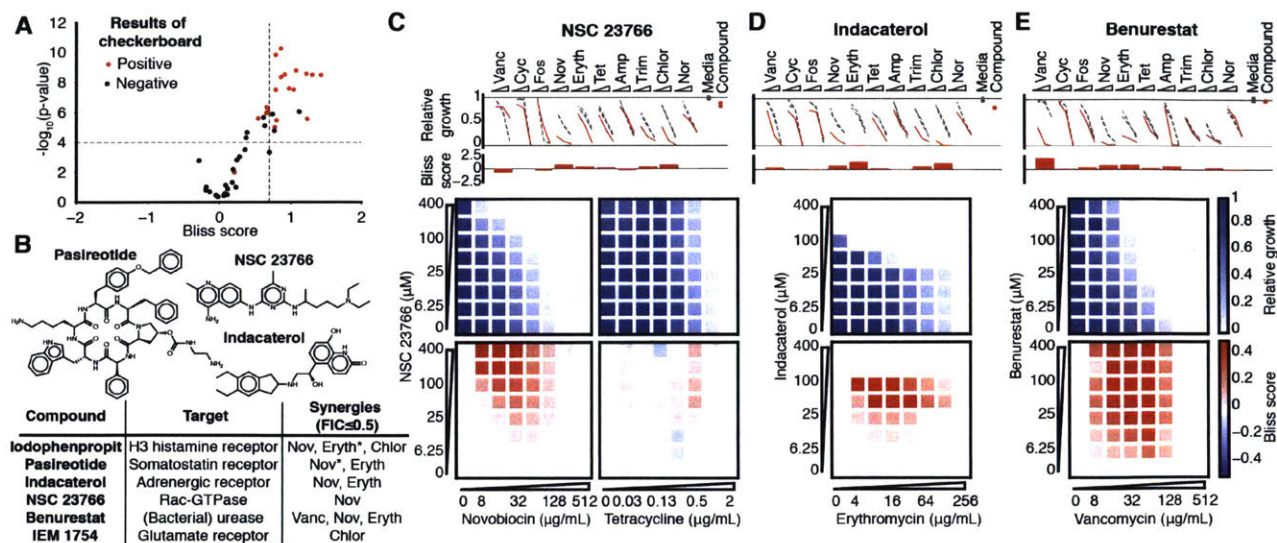
**Figure 3-4. Validation of hits from primary screen.** (**A**) In eight-point checkerboard assays with *E. coli*, we tested a total of 46 compound × antibiotic combinations of which 17 (11 distinct compounds) scored as hits in the primary screen. Combinations that scored positive (red) and negative (black) for Bliss synergy are plotted according to results from the primary screen. Gray lines indicate primary screening thresholds. (**B**) Target, status, antibiotic synergy set (by FIC index method), and selected structures of validated hits. The first four compounds are from the full-scale phase; the last two are from the pilot phase. Starred (*) antibiotics represent additional synergies revealed in validation. Structures were rendered in ChemDraw from SMILES strings. (**C**) (Top panel) Primary screening data and calculated Bliss scores for NSC 23766. Growth in presence of compounds alone (red dots, "Compound") relative to the absence of antibiotic and compound (gray dots, "Media") are shown at right. (Bottom panels) 96-well plate checkerboard assay of NSC 23766 × novobiocin (positive for synergy) (left) and NSC 23766 × tetracycline (negative for synergy) (right). For each checkerboard assay, the relative growth values and Bliss scores are shown (color scaling at right). (**D**) Primary screening and checkerboard data for indacaterol × erythromycin (positive for synergy). (**E**) Primary screening and checkerboard data for benurestat × vancomycin (positive for synergy). Full names of all abbreviated antibiotic names are provided in Table 3-1.

## 3.3.5 Our screen uncovered novel antibiotic potentiators among non-antibacterial drugs

We selected 17 hit compound × antibiotic pairs from 11 distinct compounds for confirmation in eight-point checkerboard assays measured in 96-well plate broth culture format (Figure 3-4A, Figure 3-13). For comparison, we measured an additional 29 pairs that did not pass Bliss score and p-value thresholds in the primary screen for a total of 46 tested pairs. Of the hit combinations, 14/17 (82.4%) scored as synergistic by Bliss Independence at the same dosages as in the primary screen (p = $5.8 \times 10^{-4}$, calculated from a binomial distribution null model where compound × antibiotic pairs randomly score positive with p=19/46, the fraction positive of total tested pairs) (Figure 3-4A). We investigated whether differences between primary screening Bliss scores and 96-well plate Bliss scores could be explained by physico-chemical properties of compounds, but did not find any systematic effects (Figure 3-14).

After applying the more stringent FIC synergy criterion (FIC index $\leq 0.5$) to each checkerboard, we identified six compounds among our hits with synergies with at least one antibiotic (four from full scale phase, two from pilot phase; supporting validation for pilot phase hits is shown in Figure 3-15 and Figure 3-16). For two hit compounds, we identified synergies with additional antibiotics beyond what was detected in the primary screen, and upon further inspection we found these additional compound × antibiotic pairs scored close to the thresholds applied in the primary screen (Figure 3-4A, B). Notably, we found no previous indication of antibacterial activity for five of these six compounds, which constitute a range of different chemical structures, characteristics, and known biochemical targets (Figure 3-4B). Comparing the primary screening data for each hit across the full panel of ten antibiotics shows some commonalities and differences that may provide clues as to mechanism of action (Figure 3-4C-E) [100]. For example, many hits shared common interactions with novobiocin and erythromycin, but some showed divergent effects with vancomycin ranging from strong synergy to strong antagonism (Figure 3-4C-E).

# 3.4  Conclusion

Here we demonstrated a nanoliter droplet combinatorial drug screening platform and applied it at scale to discover novel potentiators of antibiotics from a drug repurposing library. Exploring the mechanism of action of these potentiators may guide future efforts to engineer antibiotic adjuvants, an important strategy

in the fight against antibiotic resistance in Gram-negative pathogens [99]–[101]. By replacing robotic liquid handling with spontaneous random assembly of compound combinations in nanoliter droplets at a large scale, the logistical complexity of our combinatorial screen was reduced such that we could complete this screen using only manual pipetting in just 10 days. This platform is compatible with commercially available lab equipment already present in many academic and industrial life science research facilities. Other groups have already demonstrated successful droplet-based culture of a wide range of organisms including human cell lines [52]–[54], [61] and we expect that our platform can be developed to support many types of phenotypic and biochemical assays. The use of optical microscopy for assay readout facilitates extension to a variety of disease-specific models and imaging assays including gene expression reporters and high content cell imaging [53], [54]. While much work remains, our platform represents an important new tool to leverage drug combinations for chemical biology and therapeutics discovery.

## 3.5 Methods

### 3.5.1 Droplet production and microwell array chip operation

All droplets were produced using Novec 7500 oil (3M) with 1% w/w fluorosurfactant (RAN Biotech, 008-FluoroSurfactant), using Bio-Rad QX200 cartridges and a custom aluminum pressure manifold according to methods in Chapter 2 (see Chapter 2 Section 2.6.4 – Droplet production).

All experiments used Generation 1 chips fabricated and operated as described in Chapter 2 (see Chapter 2 Section 2.6.1 – Microwell design and fabrication; and Section 2.6.5 – Microwell array chip setup and loading). These microwell array chips consist of 43,000 $k$=2 microwells (see Chapter 2 Figure 2-2B).

### 3.5.2 Fluorescence microscopy and encoding

All experiments used 64 codes within the 66-code set generated by $S$=10 discrete signal levels and $d$=3 according to Chapter 2 Section 2.6.3 – Fluorescence encoding.

Fluorescence microscopy was performed using a Nikon Ti-E inverted fluorescence microscope according to methods in Chapter 2 Section 2.6.6 – Microscopy, image analysis, and fluorescence decoding.

In the antibiotic potentiation screen full-scale phase, each compound-dye mixture was imaged ahead of screening to predict effects on the fluorescence of the resultant droplets and establish an alternative centroid for affected dye mixtures.

### 3.5.3 Cell culture preparation

Plasmid-borne constitutive GFP-expressing strains of *Staphylococcus aureus* (chloramphenicol-resistant), *Pseudomonas aeruginosa* PAO1 (gentamicin-resistant), and *Escherichia coli* K-12 MG1655 (kanamycin-resistant) were used. With the exception of experiments with *S. aureus*, which were conducted in LB media, all experiments and screens were conducted in Cation-Adjusted Mueller Hinton broth (CAMHB) (BD Difco).

For all three organisms, all experiments began with overnight cultures from glycerol stocks. Cells were initially transferred to 4 mL of media plus 30 mg/mL of the respective antibiotic to select for GFP-expressing cells. Cells were kept at 37C, 220 RPM. Shortly before an experiment onset (~2-3 hours), cells were diluted 1:1000 into antibiotic-containing media and their growth monitored. Upon reaching early log phase (OD ~ 0.05, or ~$10^7$ cells/mL), cells were diluted into fresh media (no antibiotic) and normalized to a starting OD of 0.03-0.04 in fresh media. Droplets of 1 nL volumes resulted in an initial count of about 10 cells per droplet. At saturation, cell density was estimated at $10^3$–$10^4$ cells per droplet.

# 3.5.4 Methods for comparison of cell growth on droplet platform with standard methods

To compare growth rates between conventional broth culture and the droplet platform, we prepared cultures of *P. aeruginosa*, *S. aureus*, and *E. coli* (see Section 3.5.3 – Cell culture preparation). We then split cultures between (1) Erlenmeyer flasks (10% of the flask volume, 37C, 220 RPM) and (2) droplets loaded into the microwell array (37C, no shaking). We monitored growth via accumulation of GFP fluorescence measured by (1) transferring to clear-bottom 96-well plates and measuring by fluorescence plate reader (Molecular Devices SpectraMax), or (2) epifluorescence microscopy (Nikon Ti-E). For each organism, we transformed GFP measurements from the (1) 96-well plate reader to the same scale as the (2) droplet platform measurements by computing a least squares linear regression between measurements matched at each timepoint (Figure 3-1A, data shown for (1) are transformed based on linear regression).

To compare antibiotic response curves, we created serial dilutions of six (for *P. aeruginosa*) or 12 (for *S. aureus*, *E. coli*) antibiotics in media in clear-bottom 96-well plates: Trimethoprim (Trim), Chloramphenicol (Chlor), Ceftriaxone (Ceft), Tetracycline (Tet), Kanamycin (Kan), Norfloxacin (Nor), Fosfomycin (Fos), Cycloserine (Cyc), Vancomycin (Vanc), Erythromycin (Eryth), Ampicillin (Amp), Novobiocin (Nov) (Sigma-Aldrich) (Figure 3-1B). We emulsified cells cultured under the same conditions as above, and in parallel emulsified five points on each antibiotic dosage curve (no cells added). After pooling all emulsions, we loaded them in two technical replicate microwell arrays. Similarly, we then added cells to the 96-well plates and split the cell-antibiotic mixtures across two technical replicate plates (clear-bottom 96-well plates, with parafilm at edges to prevent edge effects, final volume 200 μL).

Using GFP fluorescence measurements similar to above, we compared the median GFP value from microwells that received an [antibiotic + no cells] droplet paired with a [media-only + cells] droplet, with equivalent final dosage conditions in the 96-well plates (Figure 3-6, Figure 3-7, Figure 3-8). To compare dose responses, we obtained a non-linear least squares fit of the Hill curve for concentration $C$ to data obtained from both 96-well plates and our platform (three local parameters: offset, magnitude, $IC_{50}$; 1 global parameter for each antibiotic: Hill coefficient, $h$).

$$G = offset + magnitude * \frac{1}{1 + \frac{C^h}{IC_{50}^h}}$$

In comparing fit $IC_{50}$'s, we removed antibiotics with plasmid-mediated resistance (*S. aureus:* Chlor; *E. coli:* Kan), or poor fit quality due to suboptimal dosage range (*S. aureus:* Ceft, Eryth, Nor, Tet; *E. coli:* Ceft).

As construction of droplet pairs in microwells was random, each pair of input conditions appeared in a random number of replicate microwells. To compute how technical noise scales as a function of $k$ replicate microwells, we resampled with replacement $k$ microwells from each set of replicates and recomputed the median GFP across each sample (Figure 3-1E).

# 3.5.5 Methods for antibiotic potentiation screening

We performed a small pilot screen (30 chips) and a larger full-scale screen (126 chips with 108 passing a chip quality filter, Figure 3-10). All data and performance analysis presented comes from this full-scale phase, although Figure 3-4 includes hits from both phases. Additional supporting data for pilot phase hits is shown in Figure 3-15 and Figure 3-16.

For all screening, each chip received droplets containing a total of 64 input conditions, with 32 held constant across all chips (Set 1) and 32 that varied on each chip (Set 2) (Figure 3-3A). Set 1 included [30 antibiotic conditions (10 antibiotics × 3 concentrations) + no cells] and [2 media-only controls + no cells]. Set 2 included [24-28 compounds (100 μM) + cells], [1 or 2 positive controls (sulbactam (20 μM) and/or erythromycin (5 μM)) + cells], and [1 or 2 negative "blank" media-only no-compound controls + cells]. Set 2 also included an additional [2 or 4 media-only controls + cells] that were used to measure dose response of antibiotics alone for comparison (Figure 3-3A, D, gray dotted lines). All conditions were in CAMHB

and 2% DMSO (all concentrations reported are final concentrations). We used *E. coli* K-12 MG1655 cultures ("+ cells") with normalized starting density (see Section 3.5.3 – Cell culture preparation).

We screened compounds from the Broad Institute's Drug Repurposing Library, which consists of 4,160 compounds in 52 96-well plates (80 compounds per plate at 100 μM final concentration, with controls in columns 1 and 12) [104]. We planned to divide the 4,160 compounds into batches run across different chips, with the batch size set such that expected number of replicate microwells for each compound × antibiotic droplet combination was at least 10 to achieve low assay noise (informed by analysis in Figure 3-1E). To determine the batch size, we considered that Generation 1 microwell array chips typically yield about 26,000 properly loaded and merged microwells from 43,000 microwells (see Chapter 2, Figure 2-3B). We computed the expected representation of compound × antibiotic combinations according to Chapter 2 Section 2.6.2 – Expected levels of microwell-level replication of combinations, and found that 64 unique inputs would constitute an expected average of 12.7 microwells (= 26,000 × 2 / $64^2$). Based on this analysis, each 96-well plate was divided into 3 groups of 32, each of which was screened on a separate chip but pooled with the same set of antibiotics-carrying droplets (total 32) to yield a total of 64 inputs per microwell array chip.

To measure growth inhibition, we evaluated the median GFP fluorescence intensity of the replicate microwells containing a given combination as a stable statistic for the central tendency of the intensity distribution across microwells. For example, the combination [Antibiotic A + no cells] paired with [Compound B + cells] was represented in ~13 microwells on a chip (Figure 3-3C). The median GFP intensity across these 13 replicates was used to predict whether Compound B potentiated the activity of Antibiotic A at these concentrations (Section 3.5.8 – Bliss synergy scoring). Given the nature of the chip setup, the combination [Compound B + cells] paired with [Compound C + cells] was also be represented ~13 times on this chip, enabling us to also score compound × compound synergies in addition to compound × antibiotic synergies (Figure 3-12), though this was not the focus of our analysis.

**Table 3-1. Antibiotic potentiation screen antibiotic panel.** Three-point dose response curves were generated for each antibiotic in the presence and absence of compounds. All concentrations are reported as final concentrations in Cation-Adjusted Mueller Hinton Broth, 2% DMSO.

| Name | Abbreviation | Concentration (µg / mL) | | |
|---|---|---|---|---|
| Vancomycin | Vanc | 128 | 64 | 32 |
| Cycloserine | Cyc | 16 | 8 | 4 |
| Fosfomycin | Fos | 2 | 1 | 0.5 |
| Novobiocin | Nov | 128 | 64 | 32 |
| Erythromycin | Eryth | 64 | 32 | 16 |
| Tetracycline | Tet | 0.5 | 0.25 | 0.125 |
| Ampicillin | Amp | 4 | 2 | 1 |
| Trimethoprim | Trim | 0.3125 | 0.15625 | 0.078125 |
| Chloramphenicol | Chlor | 4 | 2 | 1 |
| Norfloxacin | Nor | 0.0625 | 0.03125 | 0.015625 |

# 3.5.6 Chip quality scoring

To quality-score each microwell array chip, we measured the difference between conditions representing the top and bottom of the assay dynamic range. The top of the dynamic range is given by microwells that contained a [media-only control + cells] droplet paired with a [media-only control + no cells] droplet. To represent the bottom of the dynamic range, we used microwells containing a [media-only + cells] droplet paired with a [cycloserine (16 µg/mL) + no cells] droplet. The latter condition generates a signal that represented the lowest GFP signal level expected in a growth-suppressed assay culture.

We quantified the observed dynamic range on each microwell array chip by computing the Z-factor metric [105]. We computed the median GFP values for the set of microwells representing the maximum and minimum signal levels described ($m_+$ and $m_-$). To estimate a standard error, we bootstrap resampled median GFP estimates from each set (1000 iterations) to estimate a sampling distribution, and measured standard errors as the standard deviation of the two sampling distributions ($s_+$ and $s_-$) (Figure 3-10A). We then computed the Z-factor (Z') as follows:

$$Z' = 1 - \frac{3(s_+ + s_-)}{|m_+ - m_-|}$$

Chips with Z-factors < 0.21 were removed from analysis for low quality, a threshold determined by manual examination of the distribution (Figure 3-10B). In the full-scale phase, 85.7% of chips passed this threshold.

# 3.5.7 Antibiotic potentiation screen performance scoring

For each antibiotic in our panel (Figure 3-3A, gray dotted lines), the dynamic range of the potentiation was set by the difference between relative growth measured for the lowest concentration of the antibiotic tested and maximal possible growth inhibition. To represent maximum growth inhibition in each case, we chose cycloserine (16 μg/mL), which produced the minimum detectable signal.

To quantify assay performance for the overall screen, we compiled relative growth estimates (GFP) from all chips for each antibiotic (at the lowest concentration represented) and compared to cycloserine (16 μg/mL) (Figure 3-17). We quantified this comparison by computing the Z-factor (Z') [105] for each pair of distributions across the 108 chips from the full-scale screen phase.

# 3.5.8 Bliss synergy scoring

To estimate synergy between compounds and antibiotics, we computed the deviation from growth inhibition expected by Bliss Independence $(f_A + f_B - f_A f_B)$ [95]. If treatment Antibiotic A resulted in 80% growth $(1 - f_A)$, and Compound B resulted in 75% growth $(1 - f_B)$, then assuming they act independently we expect their combination to have resulted in 60% growth $(1 - f_A) \times (1 - f_B)$. To estimate their synergy, we subtract the observed growth from the expected growth $[(1 - f_A) \times (1 - f_B)] - (1 - f_{AB}) = f_{AB} - (f_A + f_B - f_A f_B)$.

We estimated the net growth inhibition for Antibiotic A from microwells carrying an [Antibiotic A + no cells] droplet paired with a [media-only + cells] droplet. We estimated net growth inhibition of a compound from microwells carrying a [Compound B + cells] droplet and a [media-only + no cells] droplet. We normalized all growth values to microwells containing a [media-only + cells] droplet paired with a [media-only + no cells] droplet and estimated synergy using the Bliss Independence metric. Since each antibiotic was present at three concentrations, we summed this metric for the compound across each of the three conditions to yield a final metric we called "Bliss score." Compounds with net growth inhibition exceeding 80% at the screening concentration of 100 μM were removed from analysis (total 96 compounds).

We divided Bliss scores by their corresponding standard errors to yield a test statistic (Bliss score/standard error). To estimate the standard error in our Bliss score measurement, we first bootstrap resampled (100 iterations) all microwells in the array to the number of replicate microwells counted for each pair of inputs. We then computed a bootstrapped Bliss score for each bootstrapped sample to estimate a sampling distribution, from which we computed an estimated standard error.

Using the Bliss score and estimated standard error, we computed a test statistic (Bliss score/standard error) that we modeled with a $t$ distribution fit to our blank negative controls (density function $f_T$ fit with parameters: $\upsilon = 11.23$, degrees of freedom; $\sigma = 0.922$, scale parameter, fit with scipy) (Figure 3-11).

$$f_T = \frac{\Gamma\left(\frac{(\upsilon + 1)}{2}\right)}{\sigma\sqrt{\pi\upsilon}\,\Gamma\left(\frac{\upsilon}{2}\right)}\left(1 + \frac{(x/\sigma)^2}{\upsilon}\right)^{-\frac{\upsilon+1}{2}}$$

## 3.5.9 Checkerboard validation

Hits from the antibiotic potentiation screen were re-supplied and checkerboards were constructed from 2-fold serial dilutions of a compound and an antibiotic to create a 64-point matrix in 96-well v-bottom plates (Costar), 2% DMSO (final concentration). An *E. coli* K-12 MG1655 culture was prepared (see Section 3.5.3 – Cell culture preparation) and added to the plates (final volume 100 μL; plate edges wrapped with parafilm to reduce edge effects). We incubated the plates (37C, 220 RPM, 7 hours) and measured growth by GFP accumulation using a SpectraMax plate reader (Molecular Devices) (Figure 3-13).

We calculated deviation from Bliss Independence according to the formula above for each point in the dosage matrix (using the dosage response curves for compound alone and antibiotic alone). To compare our plate data with primary screen data, we estimated Bliss synergy using the same method (Bliss score) and compound (100 μM) and antibiotic dosages (Table 3-1) as in primary screening. The metric "Bliss score" (Figure 3-13, Figure 3-14) refers to the sum of the values for each of the 3 antibiotic concentrations (see Section 3.5.8 – Bliss synergy scoring).

We called a compound × antibiotic pair positive for Bliss synergy in checkerboard assays if the summed Bliss score (at the 3 antibiotic concentrations) was ≥ 0.4. We computed a validation rate by computing the fraction of hit compound × antibiotic pairs in primary screening data (Bliss score > 0.7 and p-value < $10^{-4}$) that scored positive in the plate-based checkerboard validation testing. To assess the significance of this

result, we assumed a null model that any given compound × antibiotic pair (independent of primary screening data) scores positive in the plate-based validation with probability $p$, estimated from the fraction of total positives from all pairs tested (19/46).

## 3.5.10 Fractional inhibitory concentration determination

The fractional inhibitory concentration (FIC) is a more stringent test of synergy, defining synergy as FIC $\leq$ 0.5 [96]. For a given Antibiotic A and Compound B, we measured the minimum inhibitory concentration (MIC) of each as the first well in the dosage series with <10% growth. If this was not observed in the conditions tested, we assumed that the MIC was twice the highest tested dose. For a well in the matrix at dosage point ($A: x, B: y$) with <10% growth, we calculated the FIC = $x/\text{MIC}_A + y/\text{MIC}_B$ (where $\text{MIC}_A$ is the MIC measured for Antibiotic A independently, and $\text{MIC}_B$ is the MIC measured for Compound B independently). We classified the compound × antibiotic combination as synergistic if the minimum FIC in the matrix was $\leq 0.5$.

# 3.6 Supplemental Text

Compound exchange between droplets can yield both false negatives (due compound loss from a droplet), and false positives (due to exchange among droplets during the initial pooling step) in screening. We examined the potential for false negatives in three ways. First, the $\text{IC}_{50}$ values measured for a variety of antibiotic drugs in the droplet platform corresponded closely to the $\text{IC}_{50}$ values measured in conventional 96-well plate assays (Figure 3-1C). Second, we looked for systematic differences between the physico-chemical properties of screening hits and the full screening library (Figure 3-5). The cLogD distribution of screening hits did not significantly differ from the library (median of validated hits: 2.70) ($p > 0.45$, Mann-Whitney U test) with values as high as 3.8 (iodophenpropit), however, there was some bias toward higher molecular weight compounds (median of validated hits: 408 Da) ($p < 0.008$, Mann-Whitney U test). Third, we compared Bliss scores computed from primary screening data with those found in 96-well plate checkerboard assays at the same concentrations (Figure 3-14). While some compound × antibiotic pairs showed differences, we did not observe a systematic effect from hydrophobicity (cLogD) or the molecular weight of the compound (Figure 3-14). For example, while IPAG × tetracycline was not detected in the

primary screen, IPAG (cLogD 3.86; MW 395 Da) has similar cLogD and molecular weight to two validated hits: iodophenpropit (cLogD 3.87; MW 414 Da) and NSC 23766 (cLogD 3.05; MW 422 Da). We also note that compounds were also re-supplied at this stage, which could also explain some differences in potency (such as with SNS-032 (BMS-387032), Figure 3-13 Panel 1).

We additionally assessed false positive risk from cross-contamination between droplets. First, 108/124 chips passed stringent quality control assessments of the internal positive and negative control conditions (Figure 3-10). Second, of our primary screening hits where validation was attempted, 82.4% (14/17 tests, p-value = 0.00058 for a binomial null model across all pairs positive in plates; 8/11 distinct library compounds) were successfully validated in conventional 96-well plate checkerboard assays (Figure 3-4A). This result indicates that while the full extent of chemical compatibility with the droplet platform is unknown, screening was productive and did not rely on identifying and removing fast-exchanging or incompatible compounds in libraries prior to the screen.
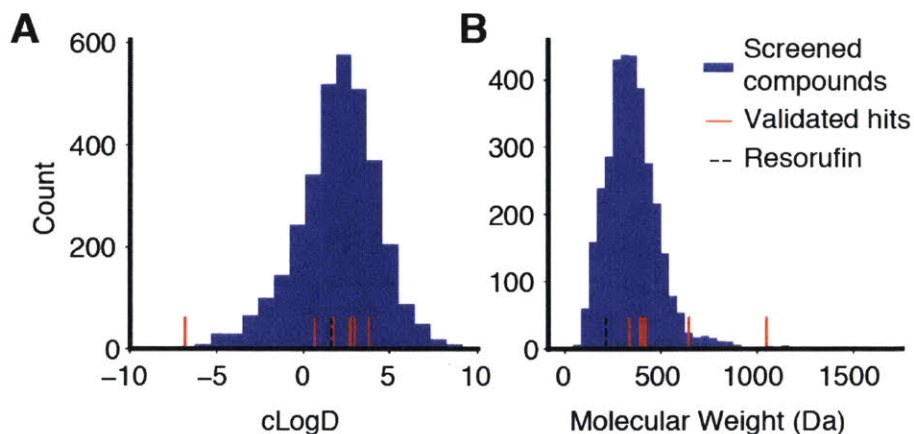
# 3.7 Supplemental Figures



**Figure 3-5. Physico-chemical properties of compounds in antibiotic potentiation screen.** To explore the compatibility of the droplet platform with common chemical libraries, we compared the distribution of calculated physico-chemical properties of screening hits to the compounds from the full screening library screened in the full-scale phase of the antibiotic potentiation screen. (**A**) We compared the calculated LogD (cLogD) of all compounds screened with validated screening hits (96-well plate checkerboard validation, Bliss score $\geq 0.4$) (Figure 3-4A, Figure 3-13) (red ticks), as well as resorufin (black tick), the fluorescent model compound used to measure compound transport across droplets and microwells by direct imaging (Chapter 2, Figure 2-5). cLogD values were computed using Accelrys Pipeline Pilot assuming pH 7.4. We did not detect any significant difference in cLogD between the hits and the overall library (median of validated hits: 2.70) ($p > 0.45$, Mann-Whitney U test). (**B**) In comparing molecular weight distributions of the library versus hits, the validated hits showed some bias towards larger compounds (median of validated hits: 401 Da) ($p < 0.008$, Mann-Whitney U test).
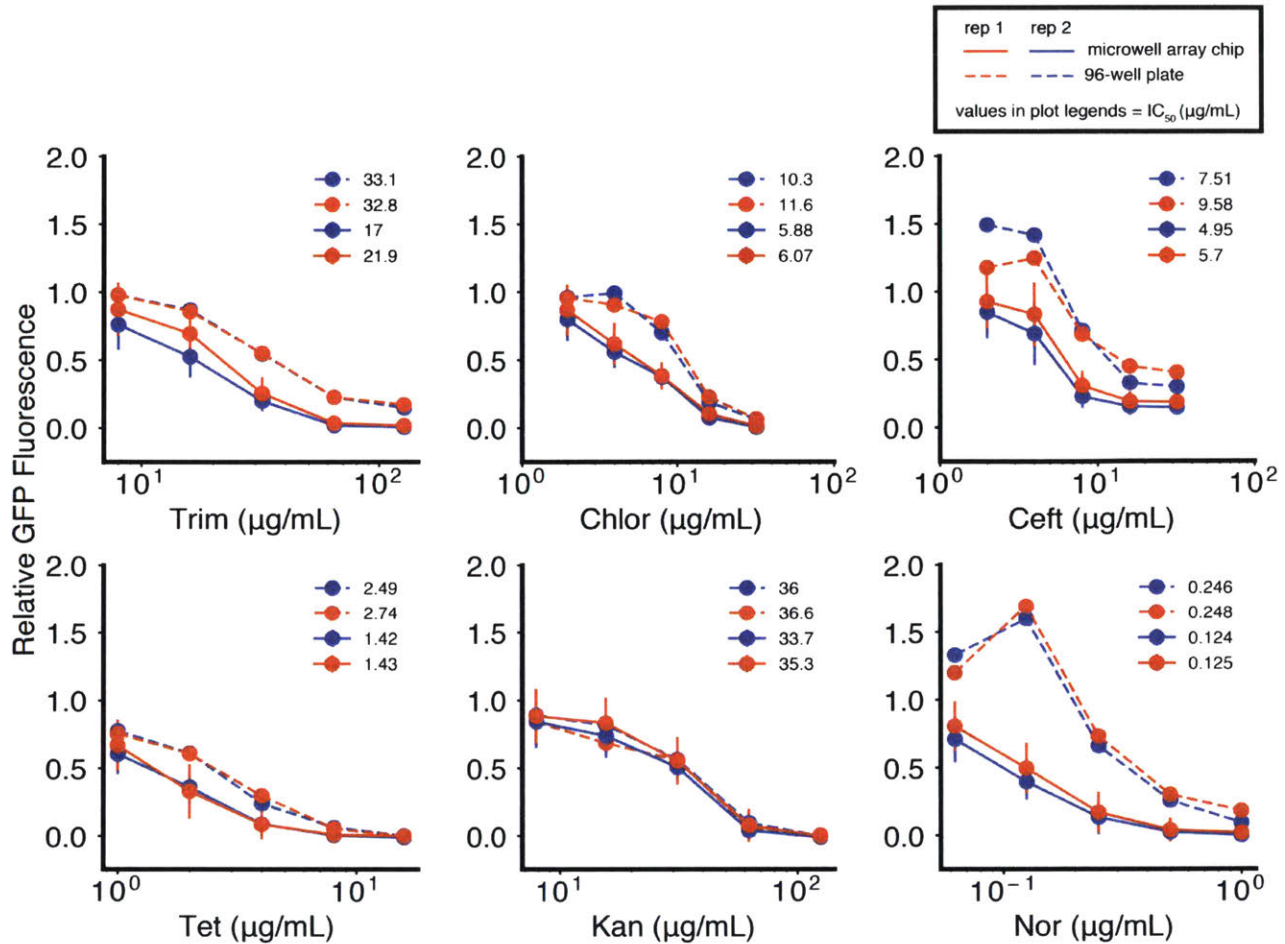
**Figure 3-6. Antibiotic dose response comparison between 96-well plates and the microwell array chip for *P. aeruginosa*.** We tested five-point dose response curves for 6 different antibiotics against *P. aeruginosa* and compared dose responses in 96-well plates (dotted lines) with the microwell array chip (solid lines), for two technical replicates (replicate 1: blue, replicate 2: red) (experimental setup is shown in Figure 3-1B). All data are normalized to no-antibiotic controls. Error bars represent standard deviations of replicate microwells for each condition, with samples of size  n = 127 (100, 147.5) (replicate 1), and n = 172 (149.5, 193) (replicate 2) (median (25$^{th}$ percentile, 75$^{th}$ percentile)).  Legends represent fit $IC_{50}$ ($\mu$g/mL) values for each curve, obtained by non-linear least squares fitting of the Hill curve to each dose response. Data points and $IC_{50}$ values are also reported Figure 3-1 and Figure 3-9.
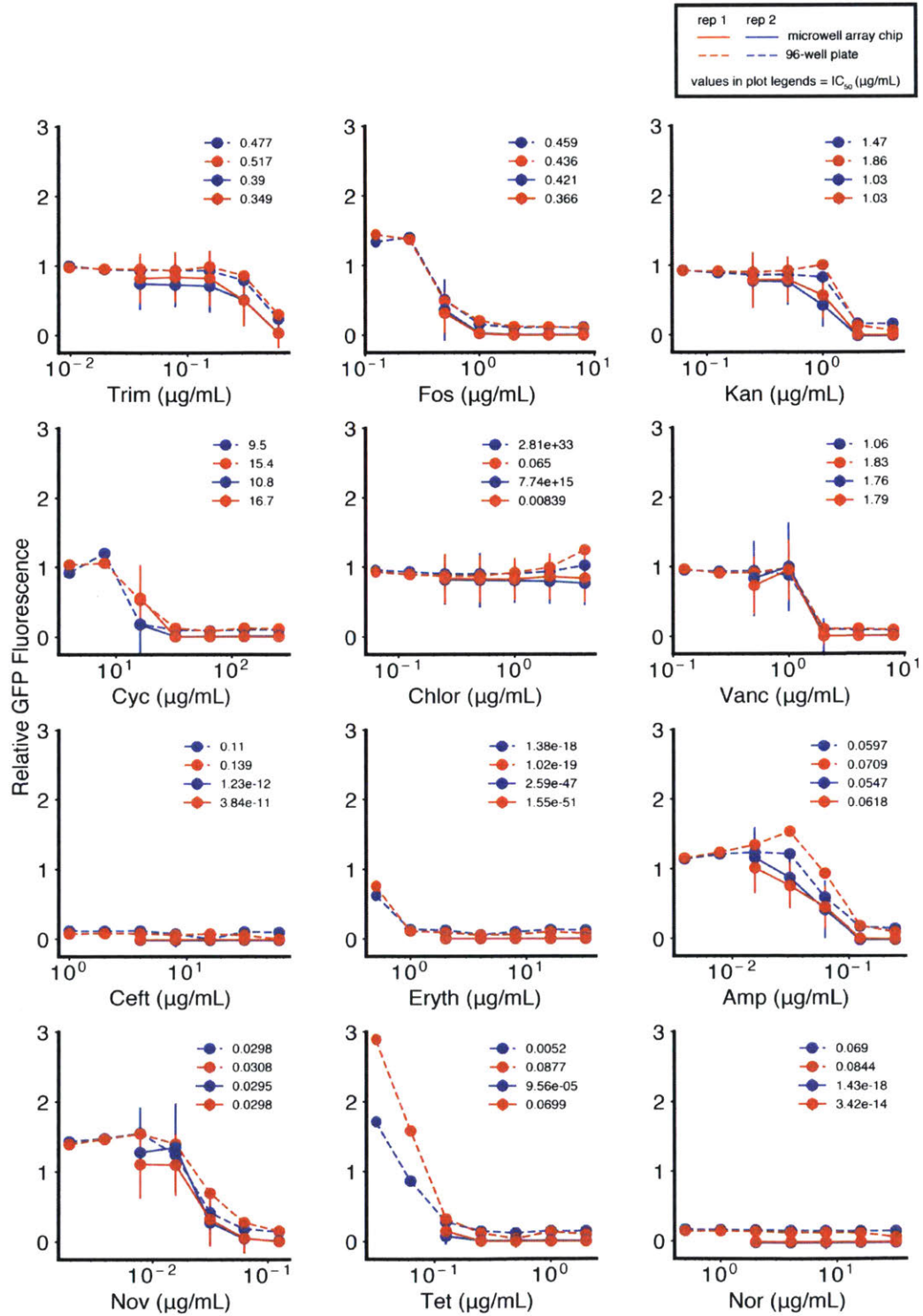
**Figure 3-7. Antibiotic dose response comparison between 96-well plates and the microwell array chip for *S. aureus*.** We tested five-point dose response curves for 12 different antibiotics against *S. aureus* and compared responses in 96-well plates (dotted lines) with the microwell array platform (solid lines), for two

technical replicates (replicate 1: blue, replicate 2: red) (experimental setup is shown in Figure 3-1B). All data are normalized to no-antibiotic controls. Error bars represent standard deviations of replicate microwells for each condition, with samples of size n = 157.5 (120.25, 190) (replicate 1), and n = 142.5 (119, 165.5) (replicate 2) (median (25th percentile, 75th percentile)). Legends represent fit $IC_{50}$ (μg/mL) values for each curve, obtained by non-linear least squares fitting of the Hill curve to each dose response. Data points and $IC_{50}$ values are also reported Figure 3-1 and Figure 3-9.
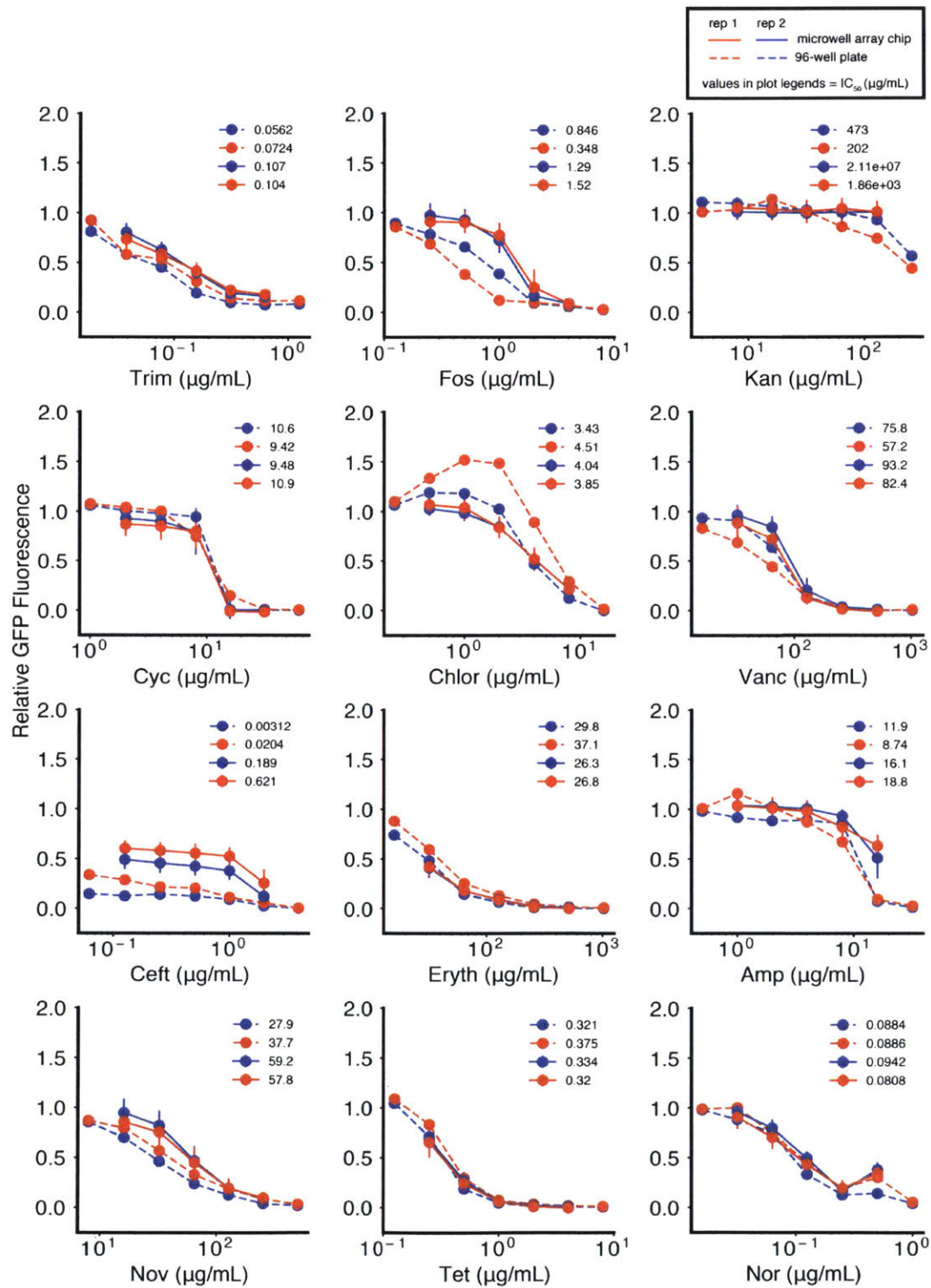
**Figure 3-8. Antibiotic dose response comparison between 96-well plates and the microwell array chip for *E. coli*.** We tested five-point dose response curves for 12 different antibiotics against *E. coli* and compared responses in 96-well plates (dotted lines) with the microwell array platform (solid lines), for two technical replicates (replicate 1: blue, replicate 2: red) (experimental setup is shown in Figure 3-1B). All

data are normalized to no-antibiotic controls. Error bars represent standard deviations of replicate microwells for each condition, with samples of size n = 171 (137.25, 208.25) (replicate 1), and n = 130 (107.5, 149) (replicate 2) (median ($25^{th}$ percentile, $75^{th}$ percentile)). Legends represent fit $IC_{50}$ ($\mu g/mL$) values for each curve, obtained by non-linear least squares fitting of the Hill curve to each dose response. Data points and $IC_{50}$ values are also reported Figure 3-1 and Figure 3-9.
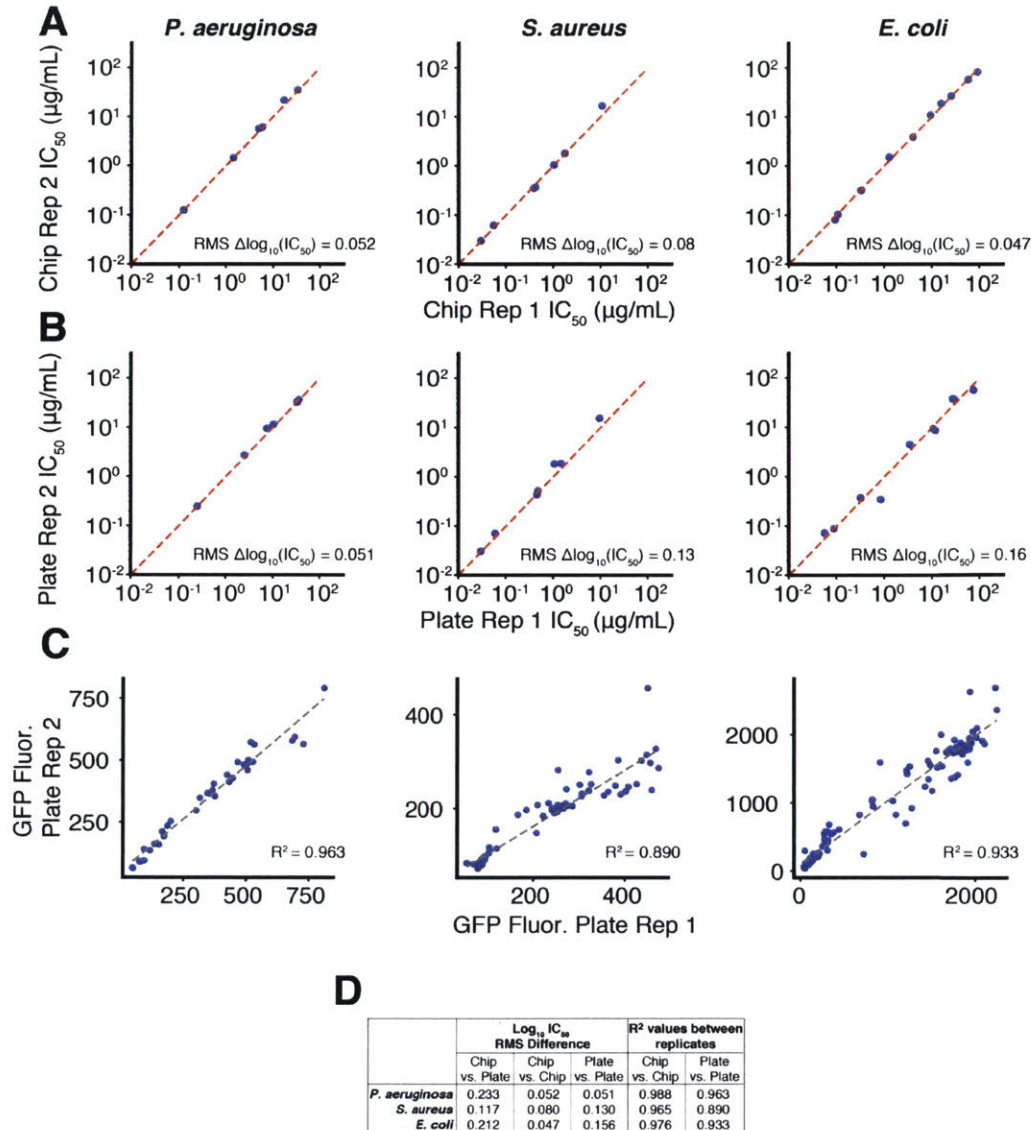
| | Log$_{10}$ IC$_{50}$ RMS Difference | | | R$^2$ values between replicates | |
|---|---|---|---|---|---|
| | Chip vs. Plate | Chip vs. Chip | Plate vs. Plate | Chip vs. Chip | Plate vs. Plate |
| *P. aeruginosa* | 0.233 | 0.052 | 0.051 | 0.988 | 0.963 |
| *S. aureus* | 0.117 | 0.080 | 0.130 | 0.965 | 0.890 |
| *E. coli* | 0.212 | 0.047 | 0.156 | 0.976 | 0.933 |

**Figure 3-9. Technical noise estimation of microwell array chip and 96-well plate assays.** (**A**, **B**) For comparison to data reported in Figure 3-1C, scatterplot comparisons of fit IC$_{50}$ values from technical replicate antibiotic dose responses (Figure 3-6, Figure 3-7, Figure 3-8) are shown. We report the root mean square of the change in log$_{10}$(IC$_{50}$) [RMS $\Delta$log$_{10}$(IC$_{50}$)], which represents the difference from the diagonal ($x = y$, red, dotted). (**C**) For comparison to Figure 3-1D, a scatterplot comparison of 96-well plate technical replicate measurements of relative GFP fluorescence, from Figure 3-6, Figure 3-7, and Figure 3-8 is shown. Lines of best fit (gray, dotted) and corresponding R$^2$ values are also shown. These R$^2$ values are also shown in Figure 3-1E (gray, dotted). (**D**) A summary table of RMS $\Delta$log$_{10}$(IC$_{50}$) and R$^2$ values for inter-platform comparisons relative to differences between technical replicates on each platform.
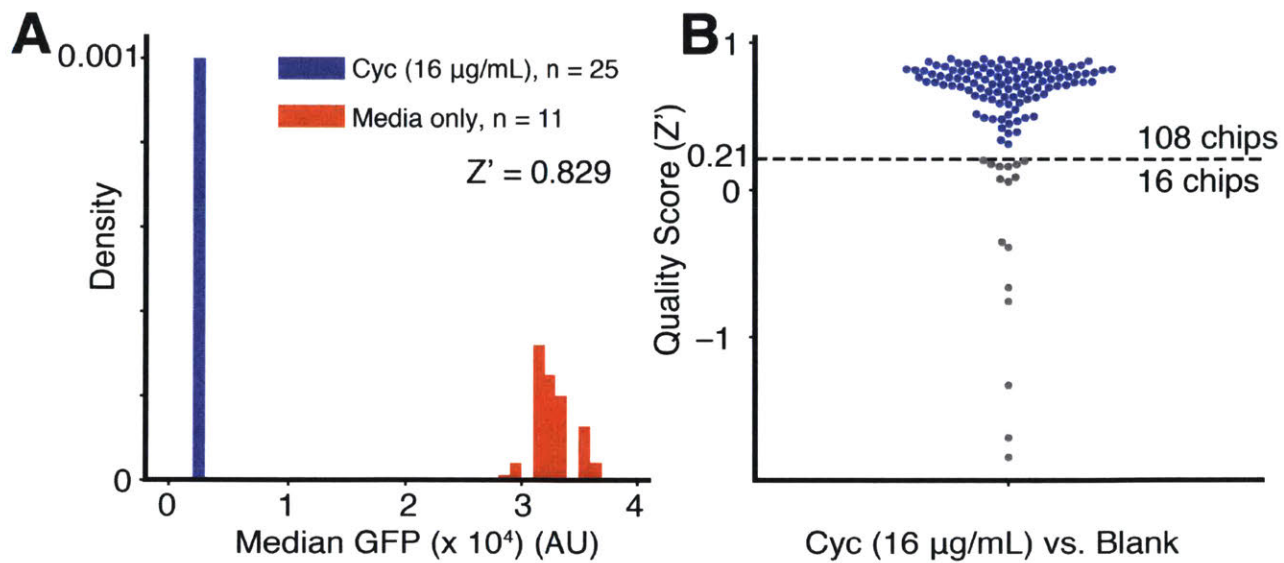
**Figure 3-10. Quality scoring individual microwell array chips used in the screen.** We estimate a quality score of each microwell array chip by evaluating the observed dynamic range in growth values. Chips with low quality were then filtered out prior to analysis of screening data. (**A**) Quality scoring procedure for a single representative microwell array chip based on calculating a Z-factor (Z') between microwells representing the top (media-only control, red) and bottom (cycloserine 16 μg/mL, blue) of the growth assay dynamic range. Histograms show median GFP growth values computed from samples bootstrapped from original sample of replicate microwells (1,000 iterations). (**B**) Each point represents the Z-factor (Z') computed for a particular microwell array chip, as shown for an exemplar chip in part A. 108 chips passed our quality threshold (Z' > 0.21), and 16 chips failed.
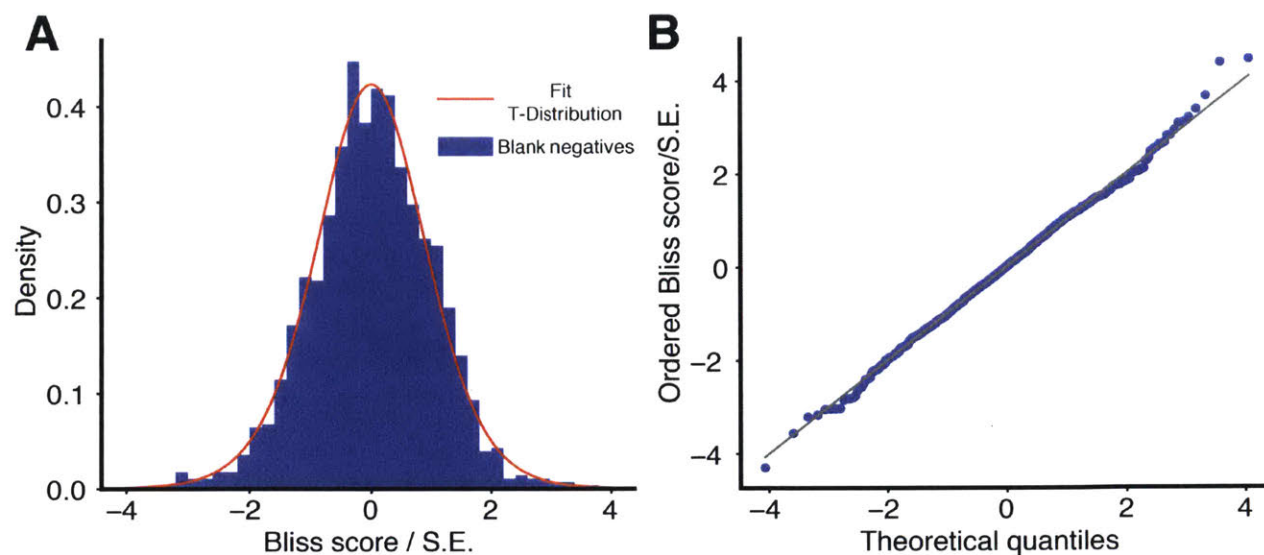
**Figure 3-11. Distribution of screening data values from blank negative controls.** To estimate the statistical significance of Bliss scores measured for each compound × antibiotic pair in the primary screen, we computed a test statistic from each Bliss score divided by an estimated standard error. Null data representing this test-statistic were obtained in-line from the screen from all pairs of blank negative controls × antibiotics. (**A**) A histogram of the test statistic for all blank negative control × antibiotic pairs (n = 140 × 10 antibiotics = 1400; blue) and a fit $t$ distribution (11.2 degrees of freedom, scale = 0.992; red) which constituted our null model for p-value calculations. (**B**) To determine the quality of the fit, we compare ordered values of our test-statistic with theoretical quantiles estimated for our fit $t$ distribution. Theoretical quantiles are generated by Filliben's estimate of the median order statistic [106]. The diagonal ($x = y$, gray) is shown for comparison.
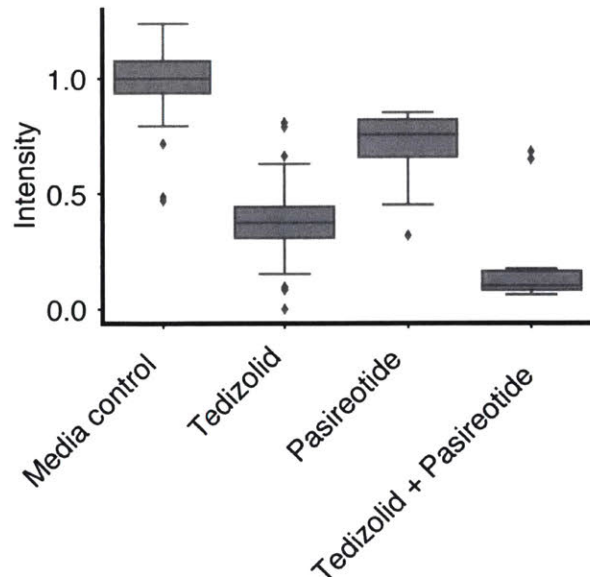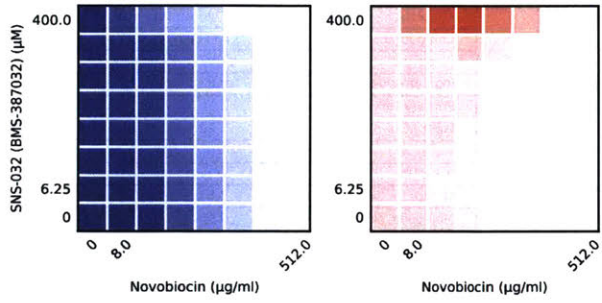
**Figure 3-12. Synergy between two compounds in antibiotic potentiation screen.** Tedizolid and pasireotide are two compounds from the drug repurposing library that were loaded on the same microwell array. As the array constructed compound × compound pairs in addition to compound × antibiotic pairs, we identified a synergistic interaction between these two compounds. Intensity reflects GFP measurements for each microwell, normalized to the median GFP value for microwells containing a [media-only + cells] droplet paired with and [media-only + no cells] droplet (Tukey box plot). Tedizolid reflects relative GFP measurements for microwells carrying a [tedizolid (100 μM) + cells] droplet paired with a [media-only + no cells] droplet. Pasireotide reflects relative GFP measurements for microwells carrying a [pasireotide (100 μM) + cells] droplet paired with a [media-only + no cells] droplet. Tedizolid + Pasireotide reflects relative GFP measurements for microwells carrying a [tedizolid (100 μM) + cells] droplet paired with a [pasireotide (100 μM) + cells] droplet. (Note that synergy is still detected for Tedizolid + Pasireotide despite there being an initial starting cell count that is twice as large as that of the other pairs.)
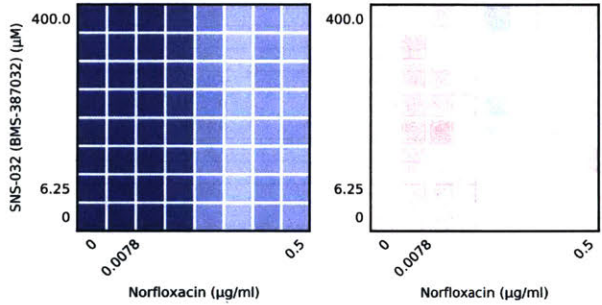
Fig. 3-13 Panel 1
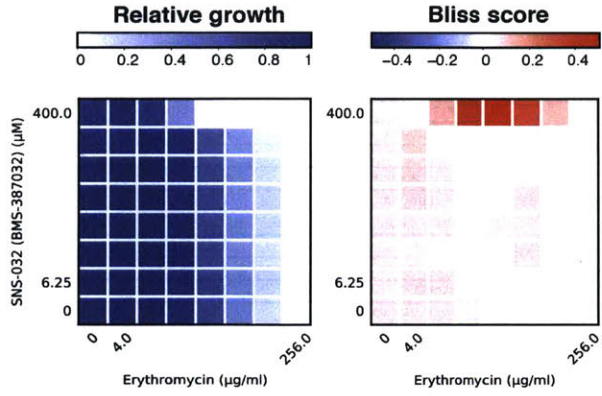


| Antibiotic | Erythromycin |
|---|---|
| Compound | SNS-032 (BMS-387032) |
| Primary Bliss | 1.12 |
| $\log_{10}$ p-value | -6.06 |
| Primary Hit | 1 |
| Plate Bliss | 0.0609 |
| Plate FIC | ≤0.625 |
| Plate Hit | 0 |
| cLogD | 1.07 |
| Molecular Weight | 381 |

| Antibiotic | Novobiocin |
|---|---|
| Compound | SNS-032 (BMS-387032) |
| Primary Bliss | 0.375 |
| $\log_{10}$ p-value | -4.3 |
| Primary Hit | 0 |
| Plate Bliss | 0.109 |
| Plate FIC | ≤1.0 |
| Plate Hit | 0 |
| cLogD | 1.07 |
| Molecular Weight | 381 |

| Antibiotic | Norfloxacin |
|---|---|
| Compound | SNS-032 (BMS-387032) |
| Primary Bliss | -0.0374 |
| $\log_{10}$ p-value | -0.444 |
| Primary Hit | 0 |
| Plate Bliss | 0.0659 |
| Plate FIC | n/a |
| Plate Hit | 0 |
| cLogD | 1.07 |
| Molecular Weight | 381 |

| Antibiotic | Vancomycin |
|---|---|
| Compound | 20-Hydroxyecdysone |
| Primary Bliss | 0.109 |
| $\log_{10}$ p-value | -0.504 |
| Primary Hit | 0 |
| Plate Bliss | 0.237 |
| Plate FIC | ≤1.0 |
| Plate Hit | 0 |
| cLogD | 1.14 |
| Molecular Weight | 481 |

| Antibiotic | Ampicillin |
|---|---|
| Compound | 20-Hydroxyecdysone |
| Primary Bliss | 0.063 |
| $\log_{10}$ p-value | -0.451 |
| Primary Hit | 0 |
| Plate Bliss | 0.0833 |
| Plate FIC | ≤1.0 |
| Plate Hit | 0 |
| cLogD | 1.14 |
| Molecular Weight | 481 |
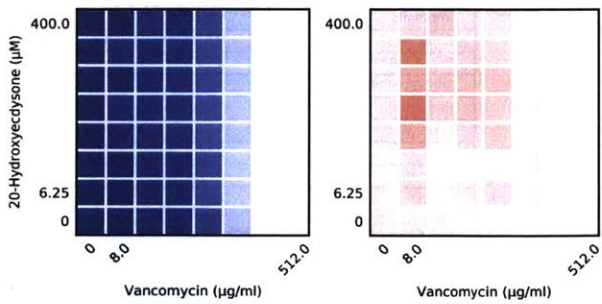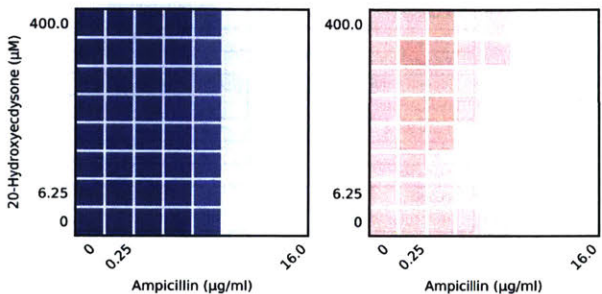
Fig. 3-13 Panel 2

**Relative growth**

0  0.2  0.4  0.6  0.8  1

**Bliss score**

−0.4  −0.2  0  0.2  0.4
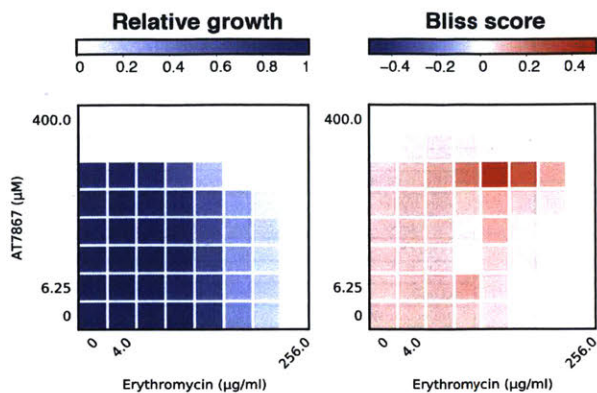


| Antibiotic | Erythromycin |
|---|---|
| Compound | AT7867 |
| Primary Bliss | 1.22 |
| $\log_{10}$ p-value | -8.6 |
| Primary Hit | 1 |
| Plate Bliss | 0.984 |
| Plate FIC | 0.75 |
| Plate Hit | 1 |
| cLogD | 2.81 |
| Molecular Weight | 338 |

| Antibiotic | Chloramphenicol |
|---|---|
| Compound | AT7867 |
| Primary Bliss | 1.07 |
| $\log_{10}$ p-value | -8.82 |
| Primary Hit | 1 |
| Plate Bliss | 1.22 |
| Plate FIC | 1.0 |
| Plate Hit | 1 |
| cLogD | 2.81 |
| Molecular Weight | 338 |

| Antibiotic | Tetracycline |
|---|---|
| Compound | AT7867 |
| Primary Bliss | 0.389 |
| $\log_{10}$ p-value | -4.66 |
| Primary Hit | 0 |
| Plate Bliss | 0.0728 |
| Plate FIC | 1.0 |
| Plate Hit | 0 |
| cLogD | 2.81 |
| Molecular Weight | 338 |

| Antibiotic | Novobiocin |
|---|---|
| Compound | Indacaterol Maleate |
| Primary Bliss | 0.797 |
| $\log_{10}$ p-value | -5.49 |
| Primary Hit | 1 |
| Plate Bliss | 0.509 |
| Plate FIC | 0.5 |
| Plate Hit | 1 |
| cLogD | 2.7 |
| Molecular Weight | 392 |

| Antibiotic | Erythromycin |
|---|---|
| Compound | Indacaterol Maleate |
| Primary Bliss | 1.42 |
| $\log_{10}$ p-value | -8.52 |
| Primary Hit | 1 |
| Plate Bliss | 0.986 |
| Plate FIC | 0.375 |
| Plate Hit | 1 |
| cLogD | 2.7 |
| Molecular Weight | 392 |
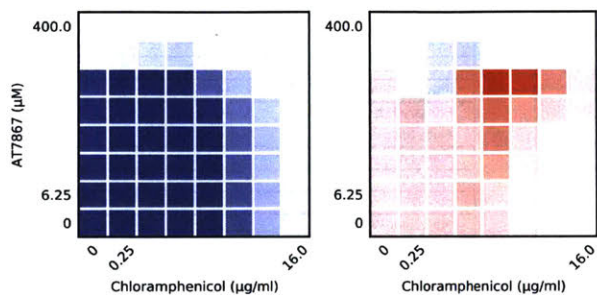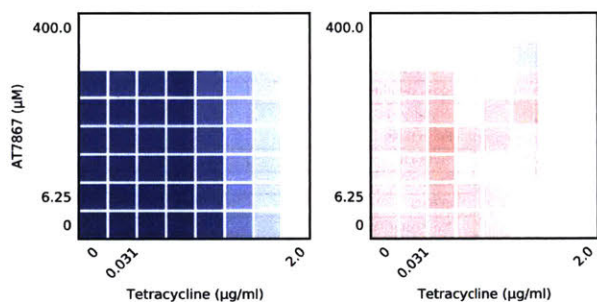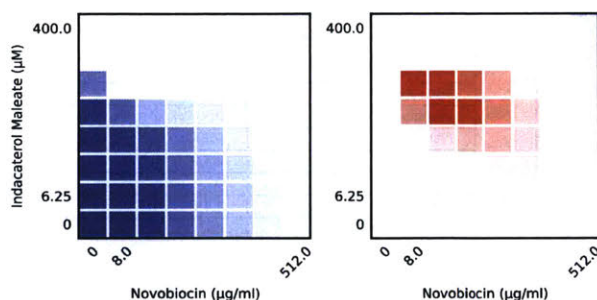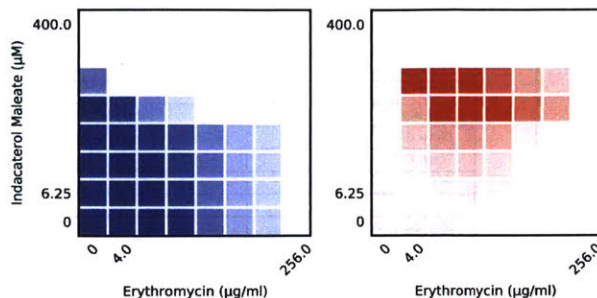
**Relative growth**

0   0.2   0.4   0.6   0.8   1

**Bliss score**

−0.4   −0.2   0   0.2   0.4

**Fig. 3-13 Panel 3**
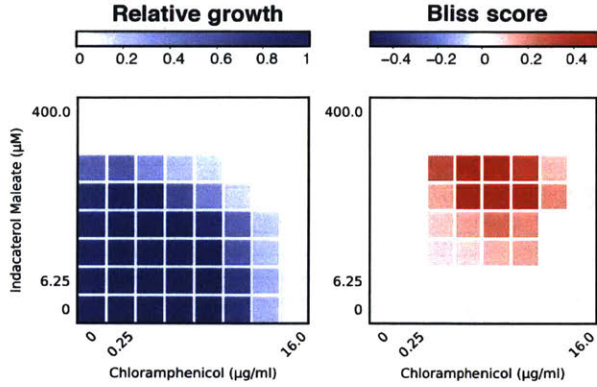
| Antibiotic | Chloramphenicol |
|---|---|
| Compound | Indacaterol Maleate |
| Primary Bliss | 1.3 |
| $\log_{10}$ p-value | -8.54 |
| Primary Hit | 1 |
| Plate Bliss | 1.4 |
| Plate FIC | 0.75 |
| Plate Hit | 1 |
| cLogD | 2.7 |
| Molecular Weight | 392 |

| Antibiotic | Cycloserine |
|---|---|
| Compound | Indacaterol Maleate |
| Primary Bliss | -0.0217 |
| $\log_{10}$ p-value | -0.369 |
| Primary Hit | 0 |
| Plate Bliss | 0.139 |
| Plate FIC | 1.0 |
| Plate Hit | 0 |
| cLogD | 2.7 |
| Molecular Weight | 392 |

| Antibiotic | Vancomycin |
|---|---|
| Compound | Acarbose |
| Primary Bliss | 0.77 |
| $\log_{10}$ p-value | -5.03 |
| Primary Hit | 1 |
| Plate Bliss | 0.584 |
| Plate FIC | ≤0.53125 |
| Plate Hit | 1 |
| cLogD | -6.84 |
| Molecular Weight | 646 |

| Antibiotic | Erythromycin |
|---|---|
| Compound | Acarbose |
| Primary Bliss | 0.656 |
| $\log_{10}$ p-value | -5.97 |
| Primary Hit | 0 |
| Plate Bliss | 0.423 |
| Plate FIC | ≤1.0 |
| Plate Hit | 1 |
| cLogD | -6.84 |
| Molecular Weight | 646 |

| Antibiotic | Cycloserine |
|---|---|
| Compound | Acarbose |
| Primary Bliss | 0.677 |
| $\log_{10}$ p-value | -6.03 |
| Primary Hit | 0 |
| Plate Bliss | 0.487 |
| Plate FIC | ≤1.0 |
| Plate Hit | 1 |
| cLogD | -6.84 |
| Molecular Weight | 646 |
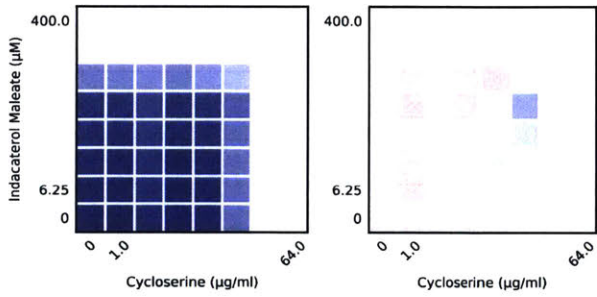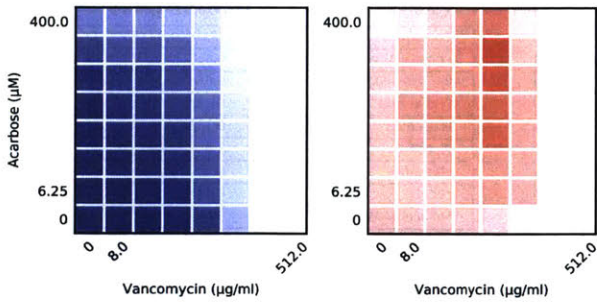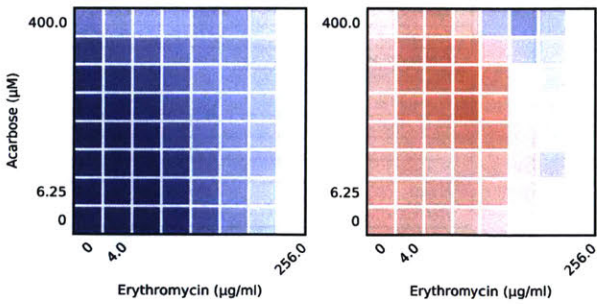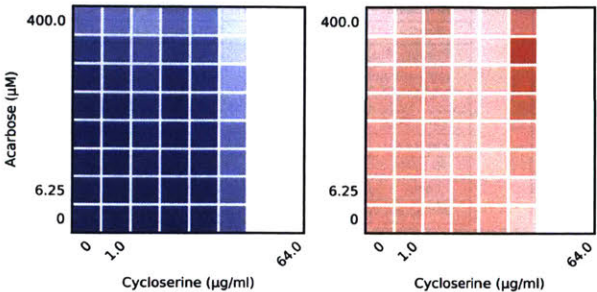
Fig. 3-13 Panel 4

**Relative growth**

0  0.2  0.4  0.6  0.8  1

**Bliss score**

−0.4  −0.2  0  0.2  0.4



| Antibiotic | Trimethoprim |
|---|---|
| Compound | Acarbose |
| Primary Bliss | 0.247 |
| log$_{10}$ p-value | -2.82 |
| Primary Hit | 0 |
| Plate Bliss | 0.174 |
| Plate FIC | ≤0.75 |
| Plate Hit | 0 |
| cLogD | -6.84 |
| Molecular Weight | 646 |

| Antibiotic | Erythromycin |
|---|---|
| Compound | PRT062607 (P505-15, |
| Primary Bliss | 0.859 |
| log$_{10}$ p-value | -8.37 |
| Primary Hit | 1 |
| Plate Bliss | 0.419 |
| Plate FIC | 0.75 |
| Plate Hit | 1 |
| cLogD | 0.646 |
| Molecular Weight | 393 |

| Antibiotic | Cycloserine |
|---|---|
| Compound | PRT062607 (P505-15, |
| Primary Bliss | 0.618 |
| log$_{10}$ p-value | -5.67 |
| Primary Hit | 0 |
| Plate Bliss | 0.308 |
| Plate FIC | 1.0 |
| Plate Hit | 0 |
| cLogD | 0.646 |
| Molecular Weight | 393 |

| Antibiotic | Chloramphenicol |
|---|---|
| Compound | PRT062607 (P505-15, |
| Primary Bliss | 0.787 |
| log$_{10}$ p-value | -9.88 |
| Primary Hit | 1 |
| Plate Bliss | 0.885 |
| Plate FIC | 0.75 |
| Plate Hit | 1 |
| cLogD | 0.646 |
| Molecular Weight | 393 |

| Antibiotic | Norfloxacin |
|---|---|
| Compound | PRT062607 (P505-15, |
| Primary Bliss | 0.192 |
| log$_{10}$ p-value | -2.19 |
| Primary Hit | 0 |
| Plate Bliss | 0.384 |
| Plate FIC | ≤0.625 |
| Plate Hit | 0 |
| cLogD | 0.646 |
| Molecular Weight | 393 |

Fig. 3-13 Panel 5



**Relative growth**

0   0.2   0.4   0.6   0.8   1

**Bliss score**

−0.4   −0.2   0   0.2   0.4

| Antibiotic | Ampicillin |
|---|---|
| Compound | 5,6-Dihydro-5-aza-2- |
| Primary Bliss | 0.767 |
| log$_{10}$ p-value | -4.78 |
| Primary Hit | 1 |
| Plate Bliss | 0.065 |
| Plate FIC | ≤1.0 |
| Plate Hit | 0 |
| cLogD | -1.67 |
| Molecular Weight | 230 |

| Antibiotic | Tetracycline |
|---|---|
| Compound | 5,6-Dihydro-5-aza-2- |
| Primary Bliss | 0.0745 |
| log$_{10}$ p-value | -0.569 |
| Primary Hit | 0 |
| Plate Bliss | 0.221 |
| Plate FIC | ≤1.0 |
| Plate Hit | 0 |
| cLogD | -1.67 |
| Molecular Weight | 230 |

| Antibiotic | Novobiocin |
|---|---|
| Compound | Iodophenpropit dihyd |
| Primary Bliss | 0.787 |
| log$_{10}$ p-value | -7.53 |
| Primary Hit | 1 |
| Plate Bliss | 0.605 |
| Plate FIC | ≤0.3125 |
| Plate Hit | 1 |
| cLogD | 3.87 |
| Molecular Weight | 414 |

| Antibiotic | Erythromycin |
|---|---|
| Compound | Iodophenpropit dihyd |
| Primary Bliss | 0.634 |
| log$_{10}$ p-value | -5.12 |
| Primary Hit | 0 |
| Plate Bliss | 0.372 |
| Plate FIC | ≤0.5 |
| Plate Hit | 0 |
| cLogD | 3.87 |
| Molecular Weight | 414 |

| Antibiotic | Chloramphenicol |
|---|---|
| Compound | Iodophenpropit dihyd |
| Primary Bliss | 1.04 |
| log$_{10}$ p-value | -7.54 |
| Primary Hit | 1 |
| Plate Bliss | 1.33 |
| Plate FIC | ≤0.5 |
| Plate Hit | 1 |
| cLogD | 3.87 |
| Molecular Weight | 414 |
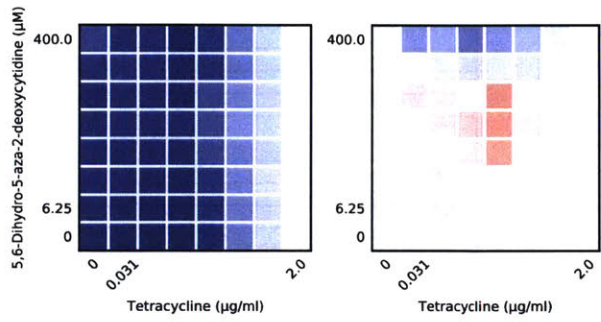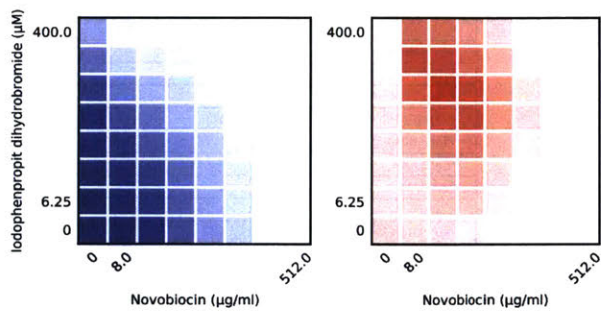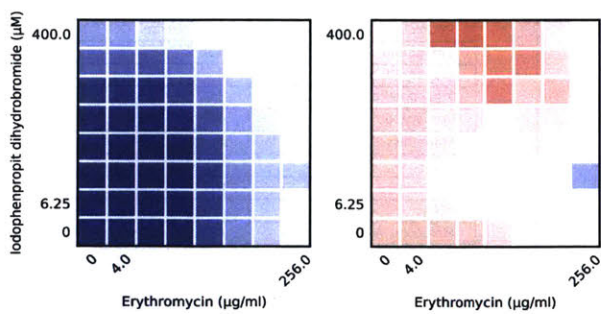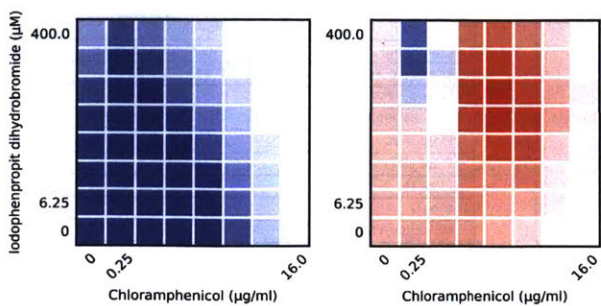
93

Fig. 3-13 Panel 6



**Relative growth** — scale bar: 0, 0.2, 0.4, 0.6, 0.8, 1

**Bliss score** — scale bar: −0.4, −0.2, 0, 0.2, 0.4
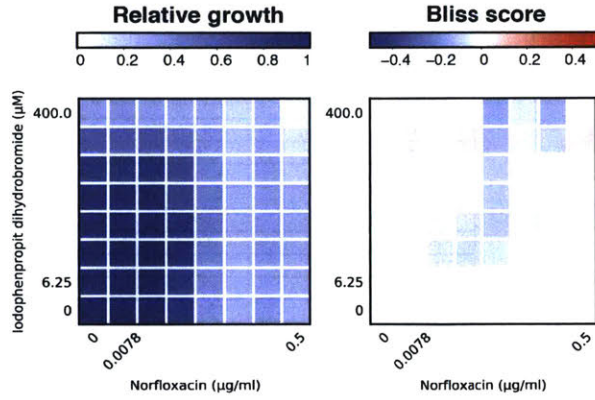
| Antibiotic | Norfloxacin |
|---|---|
| Compound | Iodophenpropit dihyd |
| Primary Bliss | 0.18 |
| $\log_{10}$ p-value | -1.32 |
| Primary Hit | 0 |
| Plate Bliss | -0.127 |
| Plate FIC | ≤1.0 |
| Plate Hit | 0 |
| cLogD | 3.87 |
| Molecular Weight | 414 |

| Antibiotic | Novobiocin |
|---|---|
| Compound | NSC 23766 |
| Primary Bliss | 0.858 |
| $\log_{10}$ p-value | -10.3 |
| Primary Hit | 1 |
| Plate Bliss | 0.655 |
| Plate FIC | ≤0.375 |
| Plate Hit | 1 |
| cLogD | 3.04 |
| Molecular Weight | 422 |

| Antibiotic | Chloramphenicol |
|---|---|
| Compound | NSC 23766 |
| Primary Bliss | 0.912 |
| $\log_{10}$ p-value | -8.56 |
| Primary Hit | 1 |
| Plate Bliss | 1.32 |
| Plate FIC | ≤0.625 |
| Plate Hit | 1 |
| cLogD | 3.04 |
| Molecular Weight | 422 |

| Antibiotic | Tetracycline |
|---|---|
| Compound | NSC 23766 |
| Primary Bliss | 0.282 |
| $\log_{10}$ p-value | -3.02 |
| Primary Hit | 0 |
| Plate Bliss | 0.218 |
| Plate FIC | ≤0.515625 |
| Plate Hit | 0 |
| cLogD | 3.04 |
| Molecular Weight | 422 |

| Antibiotic | Novobiocin |
|---|---|
| Compound | Pasireotide (ditrifl |
| Primary Bliss | 0.66 |
| $\log_{10}$ p-value | -6.37 |
| Primary Hit | 0 |
| Plate Bliss | 0.633 |
| Plate FIC | ≤0.3125 |
| Plate Hit | 1 |
| cLogD | 1.71 |
| Molecular Weight | 1.05e+03 |
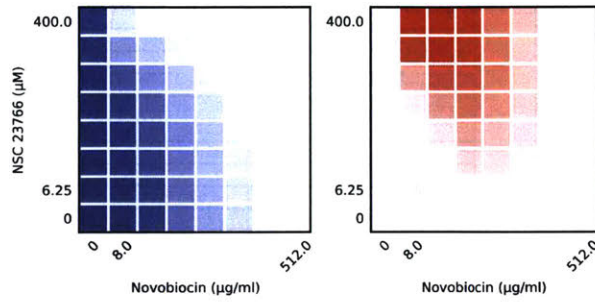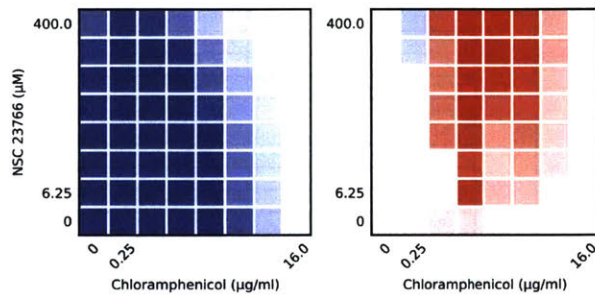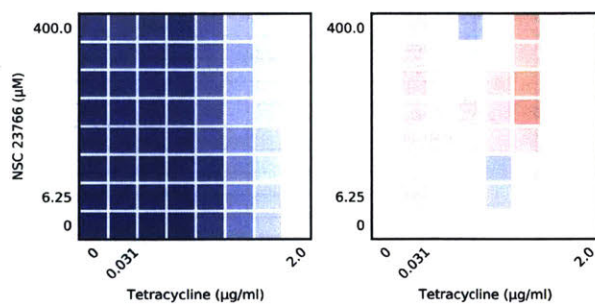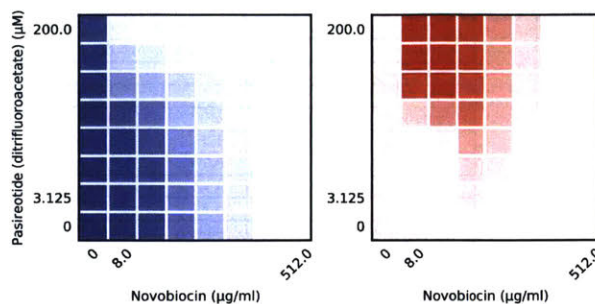
**Fig. 3-13 Panel 7**

**Relative growth**

0    0.2    0.4    0.6    0.8    1

**Bliss score**

−0.4    −0.2    0    0.2    0.4



| Antibiotic | Erythromycin |
|---|---|
| Compound | Pasireotide (ditrifl |
| Primary Bliss | 0.972 |
| log$_{10}$ p-value | -7.62 |
| Primary Hit | 1 |
| Plate Bliss | 1.71 |
| Plate FIC | ≤0.25 |
| Plate Hit | 1 |
| cLogD | 1.71 |
| Molecular Weight | 1.05e+03 |

| Antibiotic | Trimethoprim |
|---|---|
| Compound | Pasireotide (ditrifl |
| Primary Bliss | 0.542 |
| log$_{10}$ p-value | -5.61 |
| Primary Hit | 0 |
| Plate Bliss | 0.905 |
| Plate FIC | n/a |
| Plate Hit | 1 |
| cLogD | 1.71 |
| Molecular Weight | 1.05e+03 |

| Antibiotic | Norfloxacin |
|---|---|
| Compound | Pasireotide (ditrifl |
| Primary Bliss | -0.185 |
| log$_{10}$ p-value | -1.02 |
| Primary Hit | 0 |
| Plate Bliss | -0.116 |
| Plate FIC | n/a |
| Plate Hit | 0 |
| cLogD | 1.71 |
| Molecular Weight | 1.05e+03 |

| Antibiotic | Ampicillin |
|---|---|
| Compound | Oxacillin sodium mon |
| Primary Bliss | 1.23 |
| log$_{10}$ p-value | -5.59 |
| Primary Hit | 1 |
| Plate Bliss | 0.696 |
| Plate FIC | ≤0.625 |
| Plate Hit | 1 |
| cLogD | 1.63 |
| Molecular Weight | 401 |

| Antibiotic | Tetracycline |
|---|---|
| Compound | Oxacillin sodium mon |
| Primary Bliss | 0.23 |
| log$_{10}$ p-value | -1.01 |
| Primary Hit | 0 |
| Plate Bliss | 0.162 |
| Plate FIC | ≤1.0 |
| Plate Hit | 0 |
| cLogD | 1.63 |
| Molecular Weight | 401 |

95

**Fig. 3-13 Panel 8**

| Antibiotic | Vancomycin |
|---|---|
| Compound | Panobinostat (LBH589 |
| Primary Bliss | 0.114 |
| $\log_{10}$ p-value | -0.889 |
| Primary Hit | 0 |
| Plate Bliss | -0.414 |
| Plate FIC | ≤1.0 |
| Plate Hit | 0 |
| cLogD | 1.96 |
| Molecular Weight | 349 |

| Antibiotic | Ampicillin |
|---|---|
| Compound | NVP-BSK805 2HCl |
| Primary Bliss | 0.744 |
| $\log_{10}$ p-value | -5.9 |
| Primary Hit | 1 |
| Plate Bliss | 0.0694 |
| Plate FIC | 0.75 |
| Plate Hit | 0 |
| cLogD | 1.83 |
| Molecular Weight | 491 |

| Antibiotic | Tetracycline |
|---|---|
| Compound | NVP-BSK805 2HCl |
| Primary Bliss | 0.36 |
| $\log_{10}$ p-value | -3.51 |
| Primary Hit | 0 |
| Plate Bliss | -0.0859 |
| Plate FIC | 1.0 |
| Plate Hit | 0 |
| cLogD | 1.83 |
| Molecular Weight | 491 |

| Antibiotic | Cycloserine |
|---|---|
| Compound | IPAG |
| Primary Bliss | 0.697 |
| $\log_{10}$ p-value | -3.33 |
| Primary Hit | 0 |
| Plate Bliss | -0.0884 |
| Plate FIC | 1.0 |
| Plate Hit | 0 |
| cLogD | 3.85 |
| Molecular Weight | 395 |

| Antibiotic | Tetracycline |
|---|---|
| Compound | IPAG |
| Primary Bliss | 0.207 |
| $\log_{10}$ p-value | -1.99 |
| Primary Hit | 0 |
| Plate Bliss | 0.532 |
| Plate FIC | 0.75 |
| Plate Hit | 1 |
| cLogD | 3.85 |
| Molecular Weight | 395 |

96

Fig. 3-13 Panel 9



**Relative growth** / **Bliss score**

| Antibiotic | Vancomycin |
|---|---|
| Compound | SDZ 21009 |
| Primary Bliss | -0.189 |
| log₁₀ p-value | -0.8 |
| Primary Hit | 0 |
| Plate Bliss | 0.0158 |
| Plate FIC | ≤1.0 |
| Plate Hit | 0 |
| cLogD | 1.77 |
| Molecular Weight | 348 |

| Antibiotic | Ampicillin |
|---|---|
| Compound | D-Glucose 6-Phosphat |
| Primary Bliss | -0.137 |
| log₁₀ p-value | -0.708 |
| Primary Hit | 0 |
| Plate Bliss | -0.152 |
| Plate FIC | ≤1.0 |
| Plate Hit | 0 |
| cLogD | -4.07 |
| Molecular Weight | 260 |

| Antibiotic | Norfloxacin |
|---|---|
| Compound | BORNYL ACETATE |
| Primary Bliss | -0.287 |
| log₁₀ p-value | -2.78 |
| Primary Hit | 0 |
| Plate Bliss | -0.0728 |
| Plate FIC | n/a |
| Plate Hit | 0 |
| cLogD | 2.35 |
| Molecular Weight | 196 |

| Antibiotic | Trimethoprim |
|---|---|
| Compound | BORNYL ACETATE |
| Primary Bliss | 0.0871 |
| log₁₀ p-value | -1.13 |
| Primary Hit | 0 |
| Plate Bliss | -0.0908 |
| Plate FIC | n/a |
| Plate Hit | 0 |
| cLogD | 2.35 |
| Molecular Weight | 196 |

| Antibiotic | Erythromycin |
|---|---|
| Compound | ASPIRIN |
| Primary Bliss | 0.0727 |
| log₁₀ p-value | -0.496 |
| Primary Hit | 0 |
| Plate Bliss | 0.122 |
| Plate FIC | ≤1.0 |
| Plate Hit | 0 |
| cLogD | -0.245 |
| Molecular Weight | 180 |
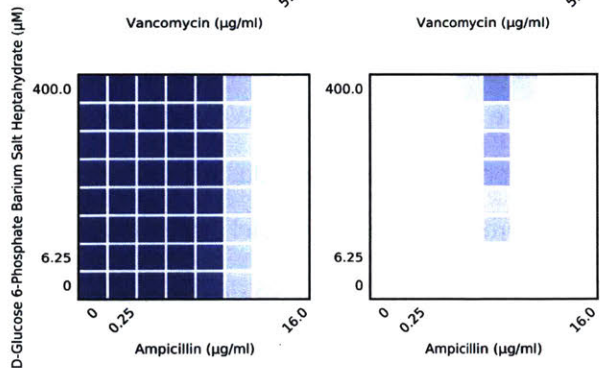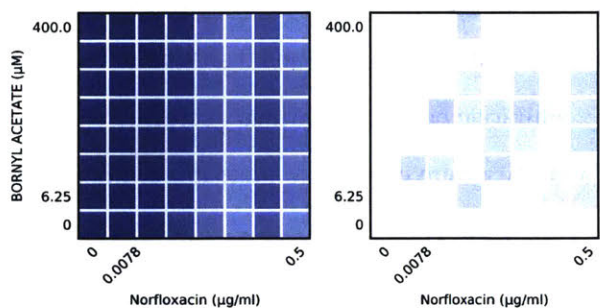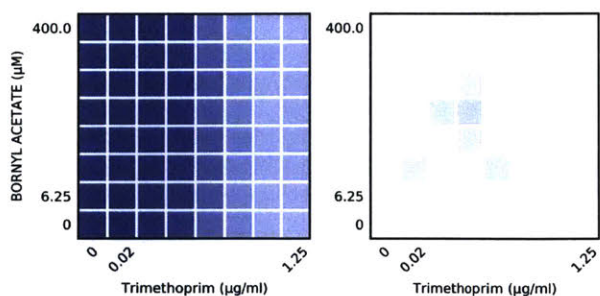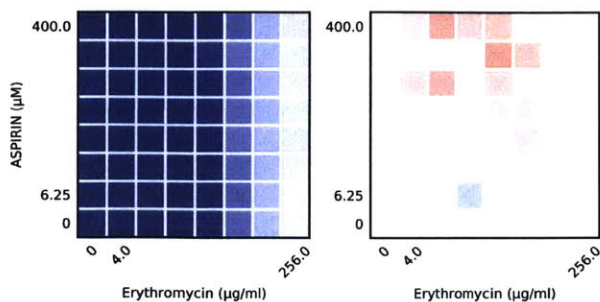
97

Fig. 3-13 Panel 10

**Relative growth**

0  0.2  0.4  0.6  0.8  1

**Bliss score**

−0.4  −0.2  0  0.2  0.4



| Antibiotic | Vancomycin |
|---|---|
| Compound | HEXACHLOROPHENE |
| Primary Bliss | -0.0491 |
| log$_{10}$ p-value | 0.469 |
| Primary Hit | 0 |
| Plate Bliss | 0.00885 |
| Plate FIC | 1.0 |
| Plate Hit | 0 |
| cLogD | 7.3 |
| Molecular Weight | 407 |
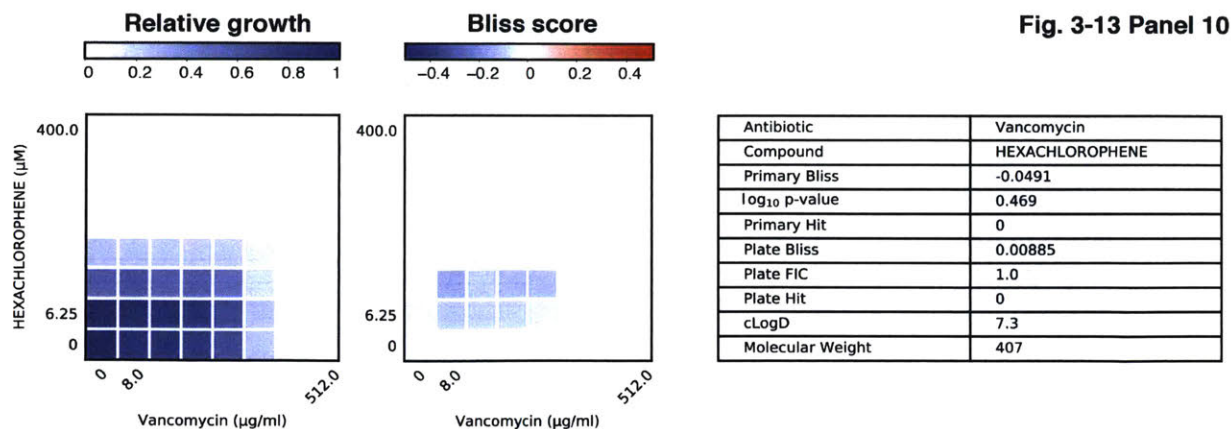
**Figure 3-13. Checkerboard validation assays (full-scale screening phase).** We chose 46 compound × antibiotic pairs to test the predictions made based on the primary screening data. All checkerboards were performed in *E. coli*. For each checkerboard, the relative growth values (left panel), calculated Bliss scores for each well position (middle panel), and a table summarizing the primary screening data (Primary Bliss, log$_{10}$(p-value), Primary Hit) and 96-well plate checkerboard synergy scores (Plate Bliss, Plate FIC, Plate Hit), and compound properties (cLogD, Molecular Weight) are shown. The value "Plate Bliss" represents the sum of the Bliss scores at the same compound concentration (100 μM) and 3 antibiotic concentrations (Table 3-1) used in the primary screen. Compound × antibiotic pairs in the primary screen were considered hits if Primary Bliss > 0.7 and -log$_{10}$(p-value) > 4, and pairs were considered plate hits if Plate Bliss > 0.4 (Fig. 4a). A scatterplot comparison of the raw data is shown in Figure 3-14.
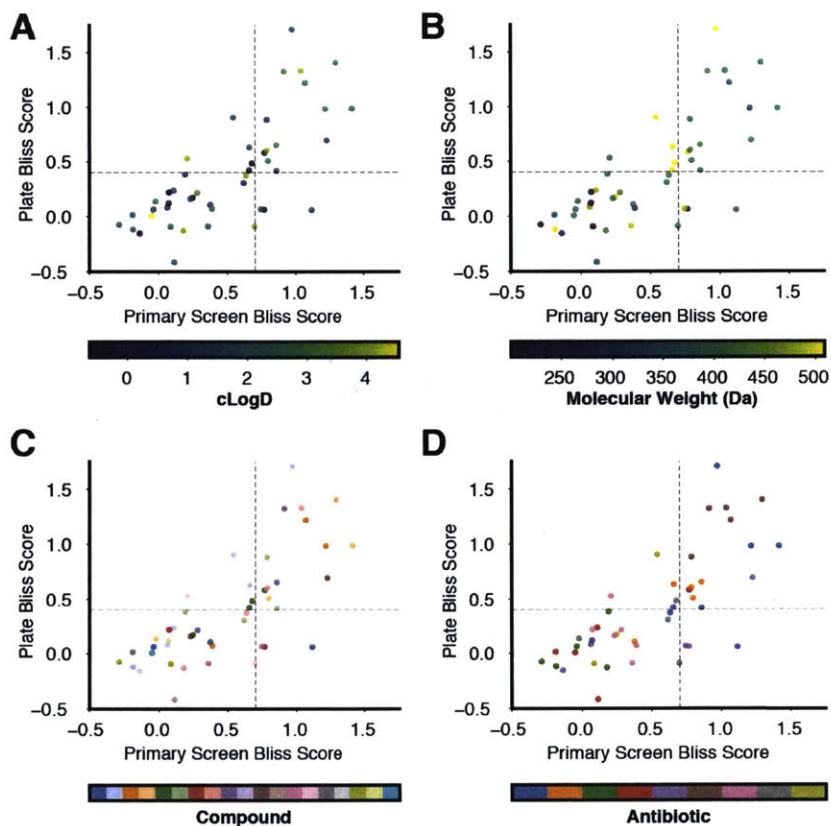
**Figure 3-14. Comparison of primary screening data to 96-well plate checkerboard assay data.** For the 46 compound × antibiotic pairs tested in 96-well plate checkerboard assays (Figure 3-13), we compared the Bliss scores computed from the primary screening data with Bliss scores computed at the same compound concentration (100 μM) and 3 antibiotic concentrations (Table 3-1) tested in 96-well plates. We investigated whether inconsistencies were predicted by chemical properties of the compound (of the compound × antibiotic pair), such as (**A**) hydrophobicity (cLogD, computed using Accelrys Pipeline Pilot) and (**B**) molecular weight (Da). Lower and upper bounds of the color scale were respectively determined by the mean +/− 1 standard deviation of the chemical property distribution of all screened compounds (Figure 3-5, blue histograms). Thresholds used to determine hits (Figure 3-4) are shown as gray dotted lines. (**C**) The same dataset, color-coded by the identity of the compound or (**D**) the identity of the antibiotic in each compound × antibiotic pair.
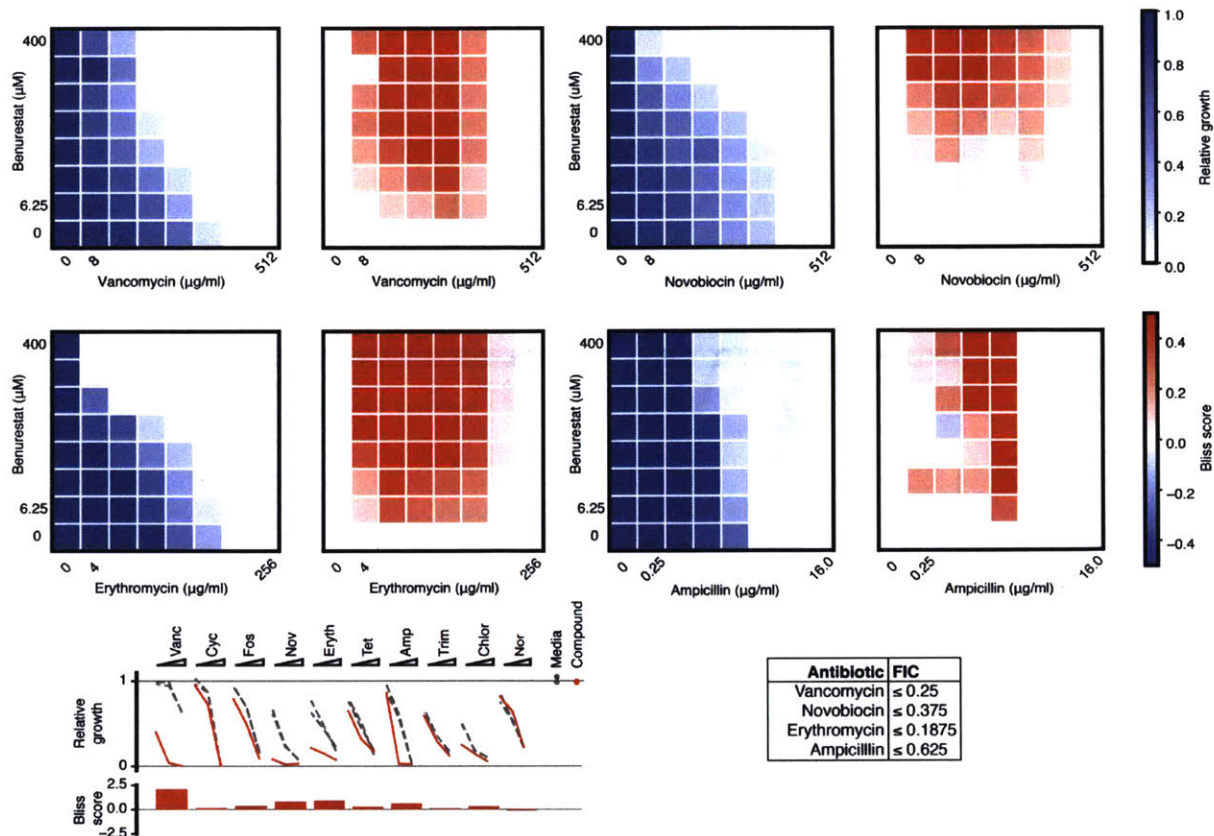
**Figure 3-15. Checkerboard validation assays – Benurestat (pilot phase).** In *E. coli*, we tested benurestat for synergies predicted with four antibiotics, measured by Bliss score and FIC. For each checkerboard, the relative growth values (left) and calculated Bliss scores for each well position (right panel) are shown. Corresponding FIC values are shown in the table below. Primary screening data are also shown for comparison.
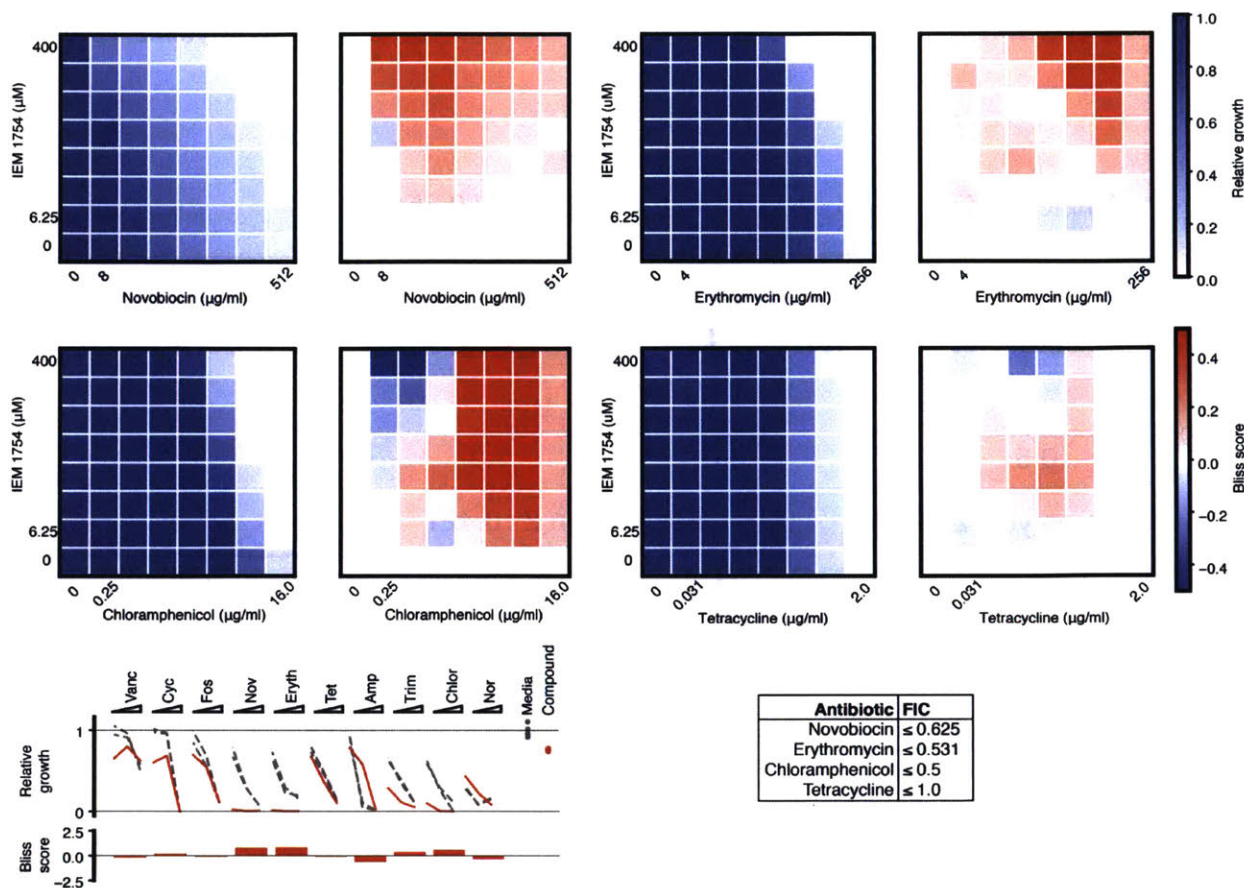
**Figure 3-16. Checkerboard validation assays – IEM 1754 (pilot phase).** In *E.coli*, we tested IEM 1754 for synergies predicted with three antibiotics, and one antibiotic predicted to show independent effects (tetracycline), measured by Bliss score and FIC. For each checkerboard, the relative growth values (left) and calculated Bliss scores for each well position (right) are shown. Corresponding FIC values are shown in the table below. Primary screening data are also shown for comparison.
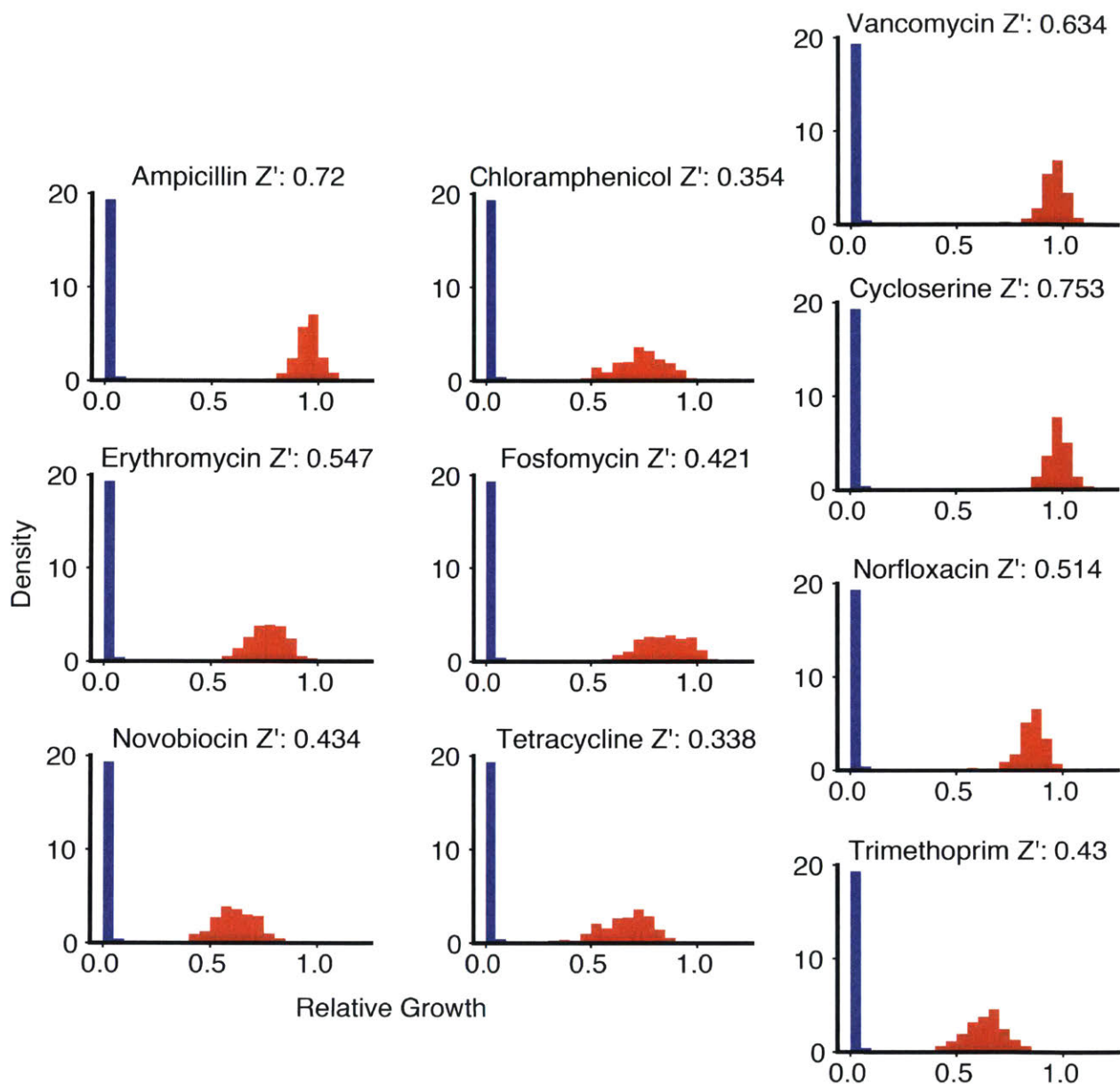
**Figure 3-17. Screening assay performance for each antibiotic in panel.** For each antibiotic in our panel, the dynamic range of the potentiation assay is the difference between the high relative growth values for the antibiotic at the lowest concentration tested (red histogram) and the low relative growth values observed under strong inhibition (cycloserine 16 µg/mL, blue histogram, same in all plots) across all 108 chips analyzed. The difference between these distributions constitutes the antibiotic-specific dynamic range within which potentiation can be detected. To quantify assay performance, we computed the Z-factor (Z', displayed in title of each plot) between these two distributions for each antibiotic.

# Chapter 4

# Toward massively parallel screening of synthetic microbial communities

*This project developed as a collaboration between the labs of Paul Blainey, Jeff Gore, and Jonathan Friedman, with contributions to all aspects from Jared Kehe, Jonathan Friedman, Anthony Ortiz, and myself. In addition, the environmental bacterial isolates used in Section 4.3.5 were collected by Logan Higgins, Jonathan Friedman, and Jeff Gore for a prior publication [107].*

*Much of this work will be published together with Generation 2 microwell designs in Chapter 2 ( Figure 2-2). Additionally, the microbial interaction screen described in Section 4.3.5 served as the pilot for work targeted for a second manuscript.*

## 4.1 Abstract

Microbial communities have important applications across metabolic engineering, bioremediation, drug discovery, and therapeutics, however engineering is frustrated by the complex underlying interaction networks. Experimental strategies to probe the interactions within microbial communities have been hindered by the logistical complexity induced by their combinatorial nature. Here, we leverage a new droplet microfluidic platform to systematically assemble microbial communities, capable of testing pairwise and higher-order interactions. Our platform considerably reduces experimental complexity, and as a proof of concept, we performed a survey of 960 pairwise interactions of microbes isolated from soil, and a comprehensive dissection of a multi-strain microbial community across different nutrient backgrounds. We expect that our platform will make broad impacts in both the basic science and engineering of microbial communities.

# 4.2  Introduction

The extreme functional diversity of microbial communities observed in nature suggests that a highly diverse set of forward-engineered microbial consortia may someday be deployed in biotechnology [108]–[111]. Consortia have already been leveraged in the discovery of novel compounds for drug discovery [112], degradation of recalcitrant polysaccharides for biofuels [113], [114], metabolic engineering [115], bioremediation [116], [117], and the development of therapeutic probiotics that promote host health and resist or reverse pathogen colonization [118]–[120]. Compared to single strains, microbial communities possess an increased range of genes and metabolic capabilities. In principle, this increase endows communities with engineerable, community-wide properties like efficient division of labor and stability of desirable phenotypes in the face of environmental fluctuations [121].

The networks of interactions that underlie community composition and function are complex and require the development of new models and engineering strategies [75]–[78]. Such strategies will likely leverage a fusion of approaches relying on genomics and metabolic modeling [122]–[124], and "bottom-up" experimental approaches to assemble and dissect the interactions within communities [125]–[127]. While genomic information continues to grow rapidly, bottom-up experimental strategies for probing microbial interactions are limited by the logistical complexity of the explosion of possible combinations of libraries of strains and environmental conditions. For example, from a library of just 20 microbes, testing all 2-way and 3-way interactions across 4 environmental conditions requires 5,400 total assays (= 4 × [20+190+1,140]; without replicates), >50 96-well plates, and ~20,000 liquid handling steps. Moreover, these combinations cannot be prepared in advance and must be assembled on the timescale of cell doubling times (< 1 hour).

We drew together multiple threads of technology development used to attack this complexity to introduce a new platform for assembling microbial communities and environments. One previous strategy cultures an array of microbial colonies on an agar gel embedded with or conditioned by a second microbe, revealing complex interactions of antibiotic production and inhibition between species [126], [128]. However, the throughput of this method is limited by the density of the array, which must be sparse to restrict diffusion between colonies [115]. To overcome this issue, other strategies confine microbes in high density microwell arrays [129], [130], or microfluidic droplets [55], assembling communities by randomly confining sets of cells in the same micro-compartment. However, the general inability to track the contents of all microwells

or droplets (their contents can only be revealed after selection), and the need to start from single cells (introducing stochasticity) limits their generalizability.

Here, we leverage these concepts to enable massively parallel assembly of synthetic microbial communities. We use a high-density microwell array to randomly confine and merge emulsions carrying liquid cultures of different organisms and environmental factors. The platform screens $\binom{n}{k}$ combinations, whereby each combination is composed of $k$ elements selected from a larger library of $n$ inputs. Both $n$ and $k$ are chosen by the user and can include different organisms and/or environmental conditions such as carbon sources, pH, and other media conditions. We demonstrate support of our platform for model environmental bacterial species with high fidelity to conventional liquid culture assays. We then use our platform to survey 960 interactions between model bacterial species and environmental bacteria isolated from soil, as well as conduct the bottom-up dissection of 200 subsets of an example 4-strain community across different carbon source environments.
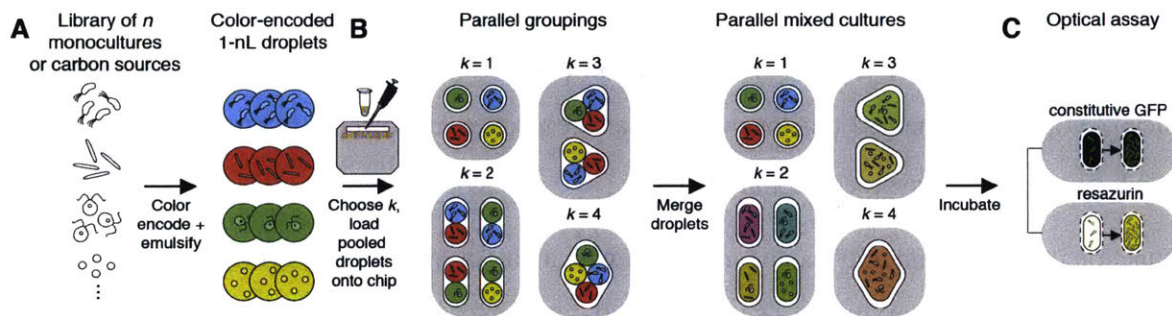
# 4.3  Results and Discussion



**Figure 4-1. Platform for bottom up construction of synthetic microbial communities.** (**A**) Droplets are loaded with monocultures of different organisms, carbon sources, or other media components that makeup the synthetic community and background. Each input is encoded by a distinct ratio of encoding dyes. (**B**) Synthetic communities are assembled by pooling the droplets carrying each component and loading them into a chip with microwells sized to capture random sets of $k$ droplets. After decoding the contents of each microwell from the encoding dyes, we merge the droplets and incubate the chip. (**C**) We perform an optical assay on each microwell to measure the function of each synthetic community.

# 4.3.1 Our platform constructs synthetic microbial communities from the bottom up

The protocol for assembling synthetic communities begins with the color encoding of $n$ inputs, which can include monocultures, environmental factors, or combinations thereof. Each color encoding is comprised of a unique ratio of three fluorescent dyes (Alexa Fluor) (total dye concentration 1 µM) that collectively encode the identity of the input (Figure 4-1A). Using a droplet generator (Bio-Rad QX200), each color-encoded input is emulsified as 1-nL droplets (with 20 µL of each culture producing 20,000 droplets) in a continuous fluorous oil phase (Figure 4-1A). These droplets are stabilized by 0.05% w/v bovine serum albumin (BSA) in the aqueous phase and a fluorosurfactant in the oil phase (see Section 4.5.1; note that we append BSA to media names where appropriate).

The droplets are pooled and injected into a flowspace beneath a microwell array chip, an inverted 6.2 cm x 7.2 cm grid of 110-µm deep microwells produced via PDMS soft lithography. Buoyant in the continuous oil phase, droplets randomly and spontaneously fill the microwells, where the size and shape of the microwell dictates the number of droplets that enter. After the microwells have been loaded with droplets, the chip is imaged at 2X magnification to decode the identity of the droplets in each microwell (Figure 4-1B). Finally, via exposure to an alternating current (AC) electric field (corona treater, Electro-Technic Products), droplets are merged together within their respective microwells (Figure 4-1A, B), generating thousands of parallel $\binom{n}{k}$ synthetic communities.

The function of each community can be measured with a pair of optical assays (Figure 4-1C). To measure the promotional or inhibitory effect of a community on a given microbe of interest, the microbe can be tagged with a fluorescent protein and growth can be tracked by the accumulation of fluorescence signal over time. In other applications, where a microbe cannot be labeled or when the total growth of all microbes in the synthetic community is of interest, we developed an assay based on the non-specific reduction of the dye resazurin to a fluorescent product, resorufin.

**Table 4-1. Model bacterial organisms and abbreviations.** The following abbreviations are used in the figures throughout the rest of this chapter. Further information is provided in Section 4.5.8.

| Organism | Abbreviation |
|---|---|
| *Escherichia coli* K-12 MG1655 | Ec |
| *Pseudomonas chlororaphis* ATCC#9446 | Pch |
| *Pseudomonas citronellolis* ATCC#13674 | Pci |
| *Pseudomonas aeruginosa* PAO1 | Pae |
| *Pseudomonas veronii* ATCC#700474 | Pv |
| *Pseudomonas fluorescens* A506 | Pf |
| *Pseudomonas aurantiaca* ATCC#33663 | Pau |
| *Pseudomonas putida* ATCC#12633 | Pp |
| *Pseudomonas syringae* B728a | Ps |
| *Herbaspirillum frisingense* GSF 30 | Hf |
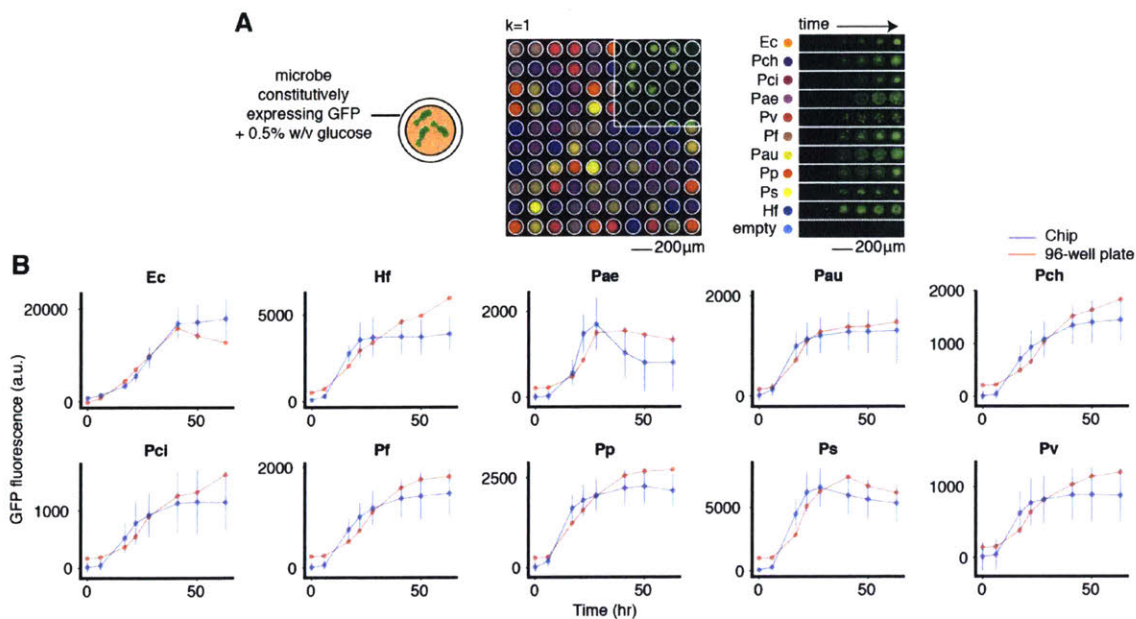
**Figure 4-2. Comparison of growth curves between platforms.** (**A**) Microbes were emulsified along with 0.5% w/v glucose in M9BSA, and loaded into a microwell array of $k=1$ microwells. Microwell arrays and corresponding cultures in 96-well plates, were incubated at room temperature (21C) with growth measured by constitutive GFP fluorescence. (*Middle*) A fluorescence micrograph showing the dye-encoded droplets carrying different microbes. The inset shows measurement of the fluorescent protein used to track microbe growth. (*Right*) A fluorescence micrograph shows the accumulation of fluorescent protein signal in a given microwell over time. (**B**) A comparison of growth curves for each organism. At each timepoint, points represent the median, and error bars represent standard deviations of the distribution of GFP measurements across all microwells containing each organism (n = 4000-5000 microwells). Measurements from 96-well plates are linearly transformed to the same scale as the microwell array (points represent the mean of 2 measurements). Full genus and species names corresponding to the abbreviated names here are provided in Table 4-1.

108

## 4.3.2 The microwell array platform supports a range of environmental microbes

We first tested the support of our platform for model organisms across microbiology. We assembled a set of ten bacterial organisms (Table 4-1) that included those used in Chapter 3 (*E. coli, P. aeruginosa*), as well as model environmental bacteria such as *Herbaspirillum frisingense*, a nitrogen-fixing species beneficial for plant growth [131], and *Pseudomonas syringae*, a model facultative plant pathogen [132]. Each model organism had been labeled with constitutive expression of a fluorescent protein (GFP or YFP) that can be monitored over time. To determine whether each organism could be cultured on the microwell array platform, we compared growth dynamics to conventional 96-well plates. A culture of each organism in a minimal media (M9BSA) supplemented with 0.5% w/v glucose was emulsified and loaded into $k=1$ microwells, or added to 96-well plates for comparison, and growth was monitored by tracking fluorescence (Figure 4-2A). The different platforms showed strong agreement indicating broad support for aerobic culture of microbial organisms represented by our set (Figure 4-2B).
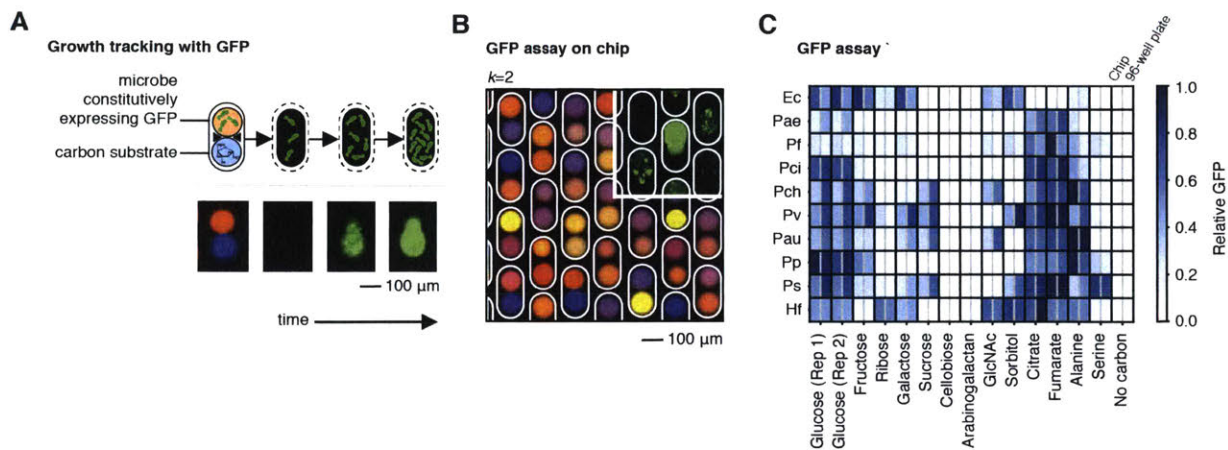
**Figure 4-3. Comparison of carbon source utilization across platforms.** (**A**) Microwells ($k$=2) capture droplets carrying *(i)* a microbe that constitutively expresses a fluorescent protein (GFP); or *(ii)* a single-carbon source media. Growth of the microbe is then monitored over time by tracking the accumulation of fluorescence signal. (**B**) Fluorescence micrographs of $k$=2 microwells loaded with pairs of droplets, showing the encoding dyes used for decoding or *(inset)* fluorescent protein used to track growth, after droplet merging and incubation. Microwells are outlined in white for contrast. (**C**) An interleaved heatmap shows fluorescence measurements of ten microbes (Table 4-1) across 13 carbon sources and 2 controls (0.5% w/v in M9BSA media) after 50 hours (21C), compared between the microwell array chip (left interleaved column) and 96-well plates (right interleaved column). For each microbe, relative measurements are normalized by subtracting background and dividing by the maximum across all carbon sources and timepoints. Full growth curves are shown in Figure 4-7.

## 4.3.3 Microbes show the same specificity for carbon substrates across platforms

Microbial interactions are impacted by the nutrient context in which they develop, for example through facilitative cross-feeding and nutrient competition, and different single-carbon source media can stabilize varied community structures [133], [134]. Therefore, we next tested that microwell array cultures maintain the carbon substrate specificity of different microbes. Using our model bacterial library, we tested growth

on 13 single-carbon source media, spanning mono- and oligomeric sugars, citric acid cycle intermediates, amino acids, and others.

The pairwise combinatorial nature of this experiment was efficiently addressed by $k=2$ microwells on our platform. We generated droplets carrying a fluorescent model microbe, single-carbon source media, or media-only controls (Figure 4-3A,B). $k=2$ microwells randomly paired microbes and carbon sources, and we tracked growth of each microbe over time (Figure 4-3A,B). For comparison, we assembled the same pairs of microbes and carbon sources in 96-well plates. Comparing platforms showed close correspondence of carbon substrate specificity (Figure 4-3C) with strong dynamic agreement (full growth curves are provided in Figure 4-7).
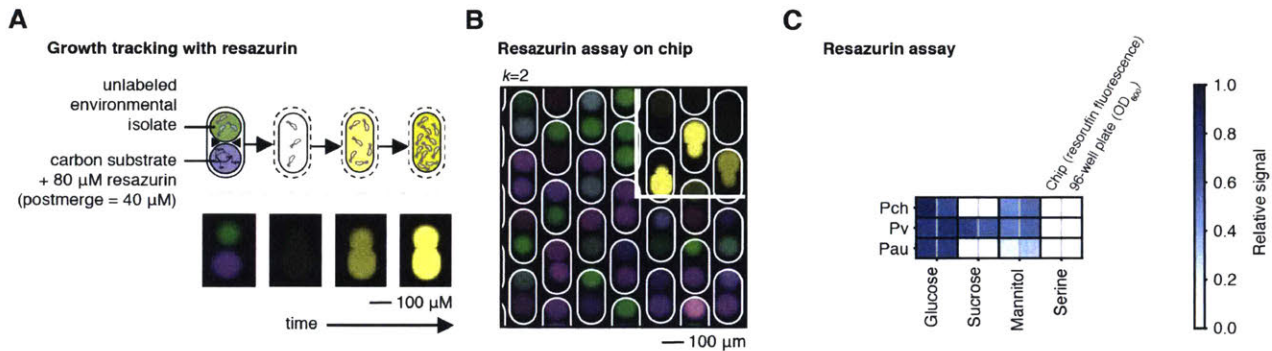


**Figure 4-4. Resazurin assay for non-specific growth measurements.** (**A**) Microwells ($k=2$) capture droplets carrying *(i)* an unlabeled microbe, such as an environmental isolate; or *(ii)* a single-carbon source media, with the addition of the dye resazurin. Microbes reduce resazurin to a fluorescent product, resorufin. Growth of microbes is monitored by the accumulation of resorufin signal. (**B**) Fluorescence micrographs of $k=2$ microwells loaded with pairs of droplets, showing the encoding dyes used for decoding or (*inset*) resorufin used to track growth, after droplet merging and incubation. Microwells are outlined in white for contrast. (**C**) An interleaved heatmap shows growth measurements for three microbes (Table 4-1) across four carbon sources after 22 hours (21C), compared between the microwell array chip (left interleaved column, resorufin fluorescence) and 96-well plates (right interleaved column, $OD_{600}$). For each microbe, relative measurements are normalized by subtracting background and dividing by the maximum across all carbon sources and timepoints. Full growth curves are shown in Figure 4-8.

## 4.3.4 Non-specific growth assays allow measurement of unlabeled microbes or total community function

While fluorescence assays have low noise and high sensitivity, microbiologists widely use optical density ($OD_{600}$) to track cell growth because of its generality. Some applications of our platform may require the use of microbes where it is difficult or impossible to engineer expression of a fluorescent protein. Experiments like the measurement of a community's ability to degrade a recalcitrant complex carbon source (*e.g.* degradation of cellulose for biofuel production) could also benefit from a "global" measure of biomass production.

For these applications, we developed an optical assay to measure microbial growth non-specifically. This assay uses resazurin, a redox-sensitive dye that is reduced to a fluorescent product (resorufin) at rates proportional to cell density by acting as an intermediate acceptor in the electron transport chain [135], [42]. Due to its low toxicity and high sensitivity, it has been broadly used for both microbial detection (*e.g.* in food safety) and cytotoxicity screening [135].

To test the resazurin assay, we again measured carbon substrate specificity as in Figure 4-3, but instead used resorufin signal to track cell growth (Figure 4-4). We generated droplets carrying three model organisms, four single-carbon source media, or a media-only control, and constructed pairwise combinations in $k=2$ microwells (Figure 4-4A, B). Comparing resorufin signal to optical density measurements ($OD_{600}$) of same conditions in 96-well plates showed strong agreement (Figure 4-4C, with full growth curves in Figure 4-8). Use as a measure of total community growth may be complicated if resorufin is produced at different rates by different microbes, but we expect the presence/absence of resorufin signal can be used in a binary sense. Further experiments are needed to explore this possibility.
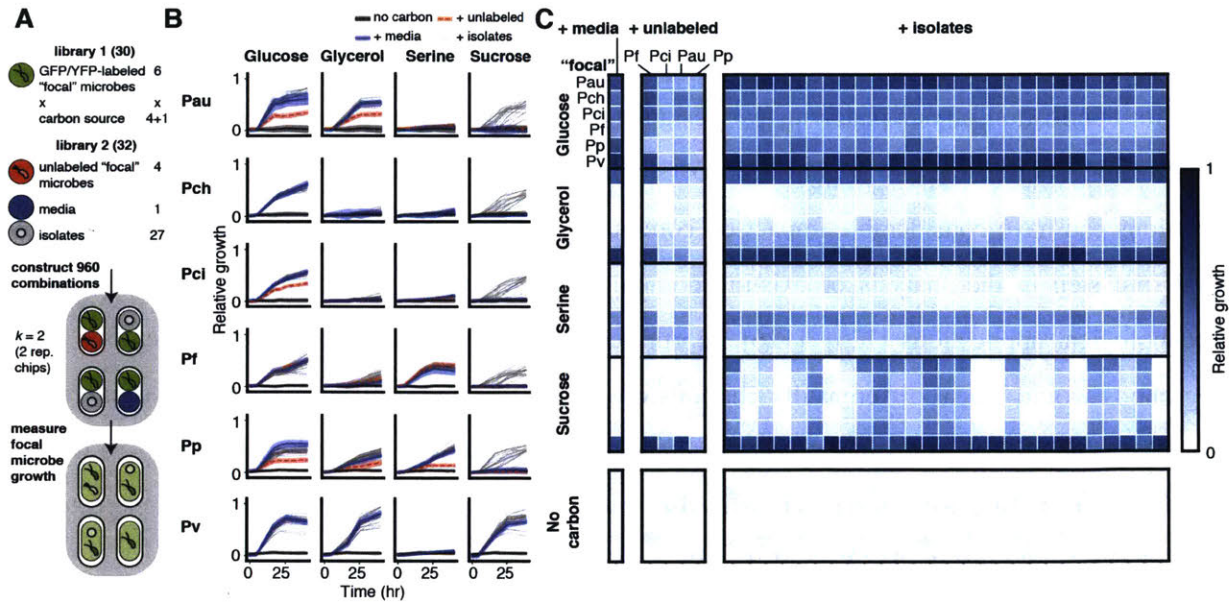
112

**Figure 4-5. Pilot microbial interaction screen.** (**A**) Experimental design. Monocultures of fluorescently labeled microbes of interest ("focal microbes") in single-carbon source media backgrounds were emulsified ("library 1"), and combined in $k=2$ microwells with "library 2" droplets carrying *(i)* unlabeled environmental isolates; *(ii)* unlabeled focal microbes; or *(iii)* base media, which contains no carbon or microbes. In each microwell, the GFP signal from each focal microbe indicated the effect of co-cultured isolate. **B**) Growth curves for each focal microbe (Table 4-1) as a function of carbon source. Co-cultures with isolates are shown in gray, and compared to the absence of a co-cultured microbe ("+ media;" blue), the corresponding unlabeled focal ("+ unlabeled;" red dashed), and the focal microbe in the absence of a carbon source ("no carbon;" black, same on all plots with shared row). Shaded regions represent the standard error of the mean, and are shown for "+ media," "+ unlabeled," and "no carbon." (**C**) A heatmap of data from part B, at 26 hours. To aid comparison, conditions in the absence of a co-cultured microbe (part B, blue lines) are shown at left. Conditions with an unlabeled focal microbe (part B, red lines) are shown as the middle column. The right column shows growth in the presence of each isolate. All data represent the mean of two technical replicate microwell array chips (a comparison between replicates is provided in Figure 4-9B). Relative growth is computed by background subtraction and normalization to the maximum GFP value on each chip.

## 4.3.5 A pilot microbial interaction screen shows common facilitation

As a pilot application of our platform, we designed a screen to measure pairwise interactions between environmental bacteria across a collection of single-carbon source backgrounds. While higher-order interactions can have considerable impact on community function, analysis of pairwise interactions is a logical first step in the analysis of existing communities or the forward engineering of new ones for biotechnological applications [125], [126]. In our screen, we hypothesized that different carbon source backgrounds would reveal different distributions of competitive and syntrophic, facilitative interactions [134]. We chose a set of four simple carbon sources – glucose, sucrose, glycerol, and serine – as well as a no-carbon control. Glucose can be metabolized by all species in our collections, while we expected that only a fraction might metabolize each of the other carbon sources in monoculture.

In order to measure interactions, we designed our screen to track the growth of an organism labeled by a fluorescent protein when co-cultured with an unlabeled organism (Figure 4-5A). We chose a set of six organisms from our model set (Table 4-1), each labeled with GFP or YFP ("focal" microbes). For use as the unlabeled organism in each pair, we chose 27 environmental bacteria isolated from a single grain of soil ("isolates"; Table 4-2) [107]. We also included four unlabeled organisms from the focal set as a positive control for nutrient competition. Last, the base media was included a negative control.

We used microwell array chips ($k$=2) to assemble all combinations of focal microbes and environmental isolates or controls in different carbon source backgrounds (Figure 4-5A). We washed and normalized monocultures of all focal microbes and isolates in a minimal media, and produced two libraries of droplets for loading into $k$=2 chips. To construct the first library ("library 1", 30 total = 6 × [4+1]), we emulsified the focal microbes (6 total) mixed with the four carbon sources (0.5% w/v; 4 total) or a negative control (media; 1 total). Isolates (27 total), unlabeled focals (4 total), or a negative control (media; 1 total) were emulsified to construct "library 2" (32 total). Droplets were loaded into $k$=2 microwells on two technical replicate microwell array chips. Each chip constructed the 960 combinations of library 1 × library 2 (Figure 4-5A), with a median of 13 replicate microwells per distinct combination on each chip (Figure 4-9A). Due to the random loading of microwells, library 1 × library 1 (450) and library 2 × library 2 combinations (512) were also assembled but not analyzed. Growth values of focal microbes from each combination showed low technical noise and high replicability between the two technical replicate microwell arrays ($R^2 \sim 0.91$; Figure 4-9B).

114

To explore the interactions between the bacteria, we compared the growth of each focal microbe across co-cultures with each isolate and control (unlabeled focals, and base media) (Figure 4-5B, C). As expected, co-culture of focal microbes with their unlabeled counterparts showed competitive effects. One exception is unlabeled *P. fluorescens*, which had a very weak effect (Figure 4-5C) and perhaps was incorrectly normalized to a lower starting cell density or imperfectly emulsified. Strong competitive or inhibitory effects among isolates were uncommon regardless of carbon source, perhaps because the model organisms were better adapted to laboratory culture conditions.

Instead, we found that co-culture with the environmental isolates often facilitated the growth of focal microbes on carbon sources where they had limited growth. This effect is most striking in the sucrose background (Figure 4-5B, C), where focal microbes that otherwise did not grow in sucrose were enabled by a large subset of environmental isolates. Sucrose facilitation did not appear specific to any focal microbe, most isolates that enabled growth in sucrose did so for all focal microbes lacking this ability. Therefore, we hypothesize that these isolates are extracellularly degrading the sucrose into glucose and fructose monomers. A more modest effect is seen in glycerol. For example, *P. putida* and *P. fluorescens* grow poorly in glycerol compared to glucose, but the growth rate is moderately improved when co-cultured with some isolates (Figure 4-5B, C). Perhaps these isolates also metabolize glycerol into intermediates that can be processed by *P. putida* and *P. fluorescens* glycolysis pathways. In contrast, cultures in serine did not show this facilitative effect (Figure 4-5B, C).
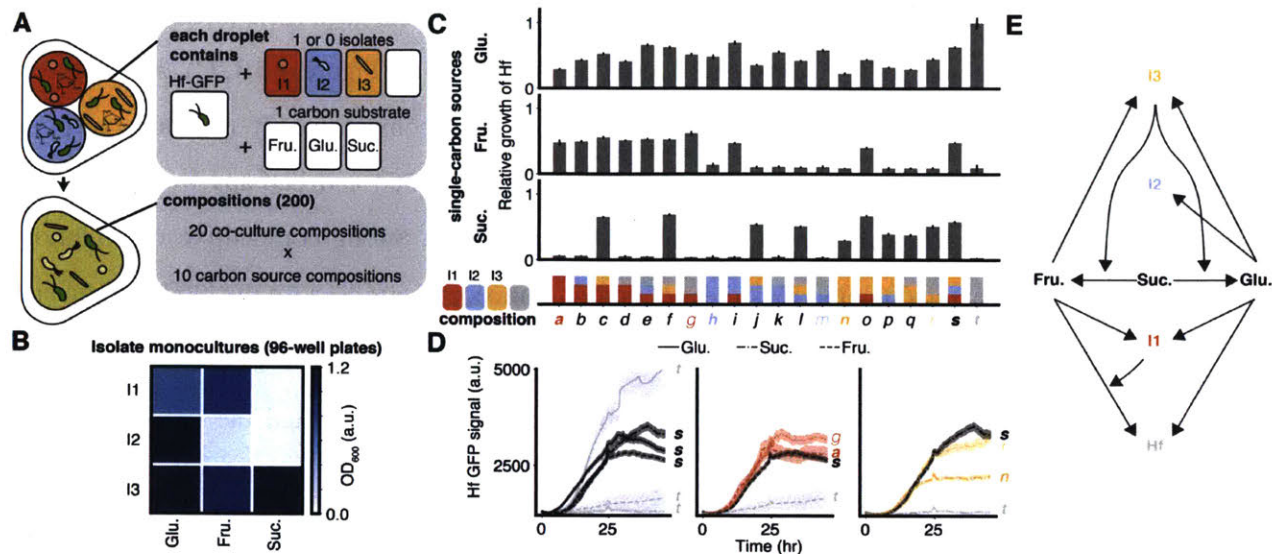
**Figure 4-6. Exploration of interactions of *H. frisingense* in a synthetic community. (A, B)** Experimental design. **(A)** *k*=3 microwells capture droplets carrying [*H. frisingense* labeled with GFP ("Hf"), a single carbon source, and 0 or 1 environmental isolates (I1, I2, I3)]. Each microwell constructs one of 200 possible compositions [20 distinct co-culture compositions of *H. frisingense* and 0-3 environmental isolates] in [10 possible carbon source compositions]. We measured a timecourse of *H. frisingense* growth by tracking GFP. **(B)** Environmental isolates were chosen based on their carbon source specificities in monoculture across glucose, fructose, and sucrose, measured in 96-well plates by optical density at 48 hours. **(C, D)** Exploration of data from microwell array, starting at a slice in time (30 hours), and then of timecourses in select conditions. **(C)** The relative growth of *H. frisingense* at 30 hours as a function of co-culture composition (*bottom*) and single-carbon source (*rows*). While not represented here, mixed-carbon source backgrounds were also constructed. Error bars represent standard error of the mean. **(D)** Selected comparisons of *H. frisingense* growth curves based on co-culture compositions in part C. *(Left)* In all single-carbon sources, a comparison of co-culture composition *s* (all environmental isolates) to composition *t* (no environmental isolates). *(Middle)* In fructose, a comparison of compositions *a* and *g*, which contain decreasing amounts of isolate I1, to composition *s*. *(Right)* In sucrose, a comparison of compositions *n* and *r*, which contain decreasing amounts of isolate I3, to composition *s*. Shaded regions show the standard error of the mean. **(E)** A phenomenological description of interactions between *H. frisingense* and the environmental isolates suggested from parts B, C, and D.

116

# 4.3.6 Our platform aids exploration of interactions within a synthetic community

In addition to screening interactions over a breadth of microbes and carbon sources, our platform can also aid a focused dissection of interactions within a single larger community. To demonstrate this, we constructed a 4-part synthetic microbial community composed of *H. frisingense* ("Hf"), a model nitrogen-fixing plant endophyte, and three environmental soil isolates in a model "complex" carbon source that does not support *H. frisingense* in monoculture, the dimeric sugar sucrose. We chose the three environmental isolates (I1, I2, I3; Table 4-3) based on their ability to grow on sucrose and monomeric "products" glucose and fructose in monoculture (Figure 4-6B).

We examined interactions between *H. frisingense* and all subsets of the environmental isolates, in single- and mixed-carbon source backgrounds of sucrose, glucose, and fructose using a $k=3$ microwell array chip (Figure 4-6A). We assembled a library of input conditions (total $12 = 4 \times 3$) from washed and normalized monocultures of the three isolates as well as a no-isolate control (total 4), each added to glucose, fructose, or sucrose (total 3). We then added a washed and normalized monoculture of *H. frisingense* to all conditions, and produced droplets such that each carried *H. frisingense*, a single isolate or no-isolate control, and a carbon source (0.5% w/v). Random loading of the droplets into $k=3$ microwells therefore constructed a total of 200 ($= 20 \times 10$) conditions from 20 distinct isolate compositions in 10 single- and mixed-carbon source backgrounds (Figure 4-6A). This operation required >10-fold less liquid handling steps than conventional methods such that it could be easily performed by hand in about 20 minutes (see Section 4.5.10).

Analysis of the different isolate compositions in single-carbon source backgrounds showed that different isolates facilitate *H. frisingense* growth in both sucrose and fructose (Figure 4-6C). While we obtained high-resolution growth curves in each condition (30 minute intervals), we first focused on a single timepoint (30 hours) of the *H. frisingense* growth curve. When in monoculture (composition $t$, Figure 4-6C) *H. frisingense* grows well in glucose, but not in sucrose, and marginally in fructose. However, growth is rescued in sucrose whenever isolate I3 is present, and in fructose whenever isolate I1 is present (Figure 4-6C).

Examining the full growth curves showed that the presence of all three isolates together (composition $s$) considerably reduces differences in growth rate and carrying capacity of *H. frisingense* across the different

carbon source backgrounds (Figure 4-6D, left panel). As expected, in composition *s* the *H. frisingense* initial growth rate is still highest on glucose, however, the highest signal is curiously achieved in sucrose.

Comparing to composition *a* shows that the presence of I1 alone likely explains the growth of *H. frisingense* in composition *s* in a fructose single-carbon source background (Figure 4-6D, middle). Indeed, fructose shows an even higher carrying capacity when the starting ratio of *H. frisingense* to I1 is increased (composition *g*) (Figure 4-6D, middle).

In contrast, the presence of I3 alone does not explain the growth of *H. frisingense* in composition *s* in a sucrose background, which achieved the highest signal level (Figure 4-6D, right). Instead this may be explained by the following (Figure 4-6E): *(i)* I3 processes sucrose into glucose and fructose; *(ii)* I1 facilitates *H. frisingense* growth on the free fructose; *(iii)* all microbes compete on the free glucose.

While the discussion here focuses on single-carbon source backgrounds (1/3 of the data), mixed carbon source backgrounds may also reveal rich interactions, such as polyauxic shifts in growth rates based on carbon sources available.

# 4.4 Conclusion

Here we introduced a new platform for the combinatorial assembly and screening of microbial communities. We demonstrated technical support for a range of microbial species, and applied our platform in two case studies of both pairwise and higher-order interactions between microbes. By making use of 1-nL scale emulsions and assembling combinations via random confinement in microwells, our platform considerably reduced the logistical complexity of these experiments by reducing both the volumes of liquid culture required and the number of liquid handling steps. For example, to perform the screen of pairwise interactions in Section 4.3.5 in conventional 96-well plates require 20 96-well plates, ~3,000 liquid handling steps, and ~4 mL of each of the 27 isolates (see Section 4.5.9) . Our platform only required a total of 62 inputs (<1 96-well plate, ~200 liquid handling steps) and 25 µL of each isolate, enabling all sample preparation to take place by hand in <1 hour (see Section 4.5.9). Also, while all experiments presented required only 1-2 microwell array chips, we previously demonstrated scaling of this platform to experiments requiring more than 100 chips (Chapter 3) enabling measurements of 100,000+ microbial interactions.

118

Screening with our platform can facilitate the direct identification of multispecies consortia possessing desirable community-wide phenotypes, such as the suppression of a pathogen, or degradation of a recalcitrant carbon substrate. Additionally, the throughput can be leveraged for a variety of other endeavors in basic microbial ecology, including the phenotypic characterization of auxotrophy, by screening sets of microbes for growth in varied carbon and nitrogen source backgrounds (*i.e.* Section 4.3.3 at high-throughput screening scale).

While the experiments here are restricted to optical assays, further technical development could extend possible assays to include mass-spectrometry [136] or optical sensors [137] to enable measurement of metabolites of interest. Other technical directions could allow for selection of a community from the array for downstream analysis, such as tracking abundances of all microbes in a community by 16S rRNA or genome sequencing.

Altogether, we expect our platform will enable new bottom-up studies of microbial communities for both basic science and biotechnological applications.

# 4.5  Methods

## 4.5.1 Base and single-carbon source media preparation

We used a minimal medium modified for compatibility with the droplet chemistry. As a base, we used M9 minimal media (1X M9 salts (Teknova), 1X Trace metals (Teknova), 0.1 mM calcium chloride, 2 mM magnesium sulfate). However, we found that use of this media alone led to significant loss of encoding dyes (and likely other hydrophobic small molecules) from droplets into fluorosurfactant reverse-micelles in the continuous phase. Supplementing this media with 0.05% w/v bovine serum albumin (BSA) stabilized the emulsions, and none of the focal microbes (Table 4-1) grow on BSA as the sole carbon source (Figure 4-3C, "No carbon" heatmap column). In summary, the media we used throughout this chapter is denoted as M9BSA (1X M9 salts (Teknova), 1X Trace metals (Teknova), 0.1 mM calcium chloride, 2 mM magnesium sulfate, 0.05% w/v BSA).

Unless indicated otherwise, all single-carbon source media were prepared to a final expected concentration (post-droplet merging) of 0.5% w/v M9BSA and sterile filtered. Controls denoted as "No carbon," indicate the base M9BSA media.

## 4.5.2 Cell culture preparation

Cultures of organisms for input into droplets were prepared in two phases. First, all cultures underwent an initial "starter phase", whereby glycerol stocks of environmental isolates and fluorescent model organisms were inoculated into 525 μL Lysogeny Broth (LB) (2-mL 96-well plate) and 4 mL (15-mL culture Falcon tube), respectively (30C, 220 RPM, 16 hr). Inoculations were conducted via pin replicator (sterilized via 70% v/v ethanol bath and heat treatment between inoculations).

A subsequent "preculture phase" (30C, 220 RPM, 24 hr) began by washing the starter phase cultures two times with M9BSA via centrifugation, removing the supernatant (Agilent Bravo), and resuspending the pellet in fresh M9BSA. Cells were then normalized to a starting $OD_{600}$ of 0.01 in M9BSA + 0.5% w/v glucose and grown for 16 hours (25C, 220 RPM).

Prior to use in an experiment, the cells were again cells twice in in M9BSA and normalized to a starting $OD_{600}$ of 0.04, either manually by micropipette or using the Perkin Elmer Janus robotic liquid handler. After adding encoding dyes, emulsions of the normalized cells were prepared and injected into the microwell array chip.

## 4.5.3 Fluorescence encoding

All inputs into droplets were encoded by a distinct ratio of Alexa Fluor 555, Alexa Fluor 594, and Alexa Fluor 647 (total concentration 1 μM) (Thermo Fisher Scientific). All ratios were a subset of ratios show in Figure 2-4. An alternative dye set was used in the resazurin assay (see below).

## 4.5.4 Microwell array chip operation

All microwell array chips were operated as described in Chapter 2.

## 4.5.5 Resazurin assay

A first set of droplets was generated that contained monocultures (OD = 0.005 – 0.02) in M9BSA with no carbon substrate. A second set contained carbon sources with 80 μM resazurin (such that, upon merging within $k$ = 2 microwells, the final resazurin concentration was 40 μM). The encoding dyes Alexa Fluor 488, Alexa Fluor 594, and Alexa Fluor 647 were used to minimize interference with resorufin. These dyes were added at 10 μM, rather than the standard 1 μM, to overcome interference from resazurin absorption of fluorescence excitation. Upon merging of droplets in $k$=2 microwells, organisms were exposed to both a carbon substrate and the resazurin. If the carbon source enabled growth, a fluorescent signal corresponding to the accumulation of resorufin was detected.

## 4.5.6 Fluorescence microscopy

All fluorescence microscopy was performed using a Nikon Ti-E inverted fluorescence microscope with fluorescence excitation by a Lumencor Sola light emitting diode illuminator (100% power setting). Images were taken across four fluorescence channels for GFP or YFP (same filter set, Semrock GFP-1828A) and the three encoding dyes, Alexa Fluor 555 (Semrock SpGold-B), 594 (Semrock 3FF03-575/25-25 + FF01-615/24-25), 647 (Semrock LF635-B). For the resazurin assay, Alexa 488 was imaged with Semrock GFP-1828A and resorufin with Semrock SpGold-B.

Images were collected by a Hamamatsu ORCA-Flash 4.0 CMOS camera (exposure times range 50ms – 500ms) at 4X optical magnification (with 4X pixel binning) or 2X optical magnification phase (with 2X pixel binning). Pixel resolution was 6.5 μm / pixel resolution in both cases. The exposure timing was dictated by the magnification and pixel binning. The total scanning time for 2X and 4X magnification were 12 minutes and 20 minutes, respectively.

## 4.5.7 Image analysis, fluorescence decoding, and fluorescence growth assays

All image analysis methods used for fluorescence decoding of droplets were the same as described in Section 2.6.6.

To measure the growth of a fluorescent organism or resorufin signal as a function over different biotic backgrounds and carbon sources, we computed the median fluorescence across all microwells sharing the same set of droplets.

## 4.5.8 Set of model bacterial organisms

Table 4-1 shows the set of fluorescently-labeled bacterial organisms used throughout this chapter. *H. frisingense* was provided by the laboratory of Erica Hartmann [131]. *P. syringae* and *P. fluorescens* were provided by the laboratory of Nadav Kashtan. *E. coli* and *P. aeruginosa* were provided by the laboratory of Deborah Hung. *P. putida* was provided by the laboratory of James Bryers [138], via Jeff Gore. All other organisms were provided by the laboratory of Jeff Gore, and were made by Nicole Vega. Each organism has been engineered to constitutively express GFP or YFP, either from a plasmid or chromosomal integration. Regardless of the specific fluorescent protein, we always monitored growth via the same fluorescence filter set (Semrock GFP-1828A, see Section 4.5.6).

## 4.5.9 Methods for pilot microbial interaction screen

To carry out the pilot microbial interaction screen (Section 4.3.5, and Figure 4-5), we prepared the focal microbes, unlabeled focals, and environmental isolates described in Section 4.5.2. Methods for isolation, selection of environmental isolates are described in Section 4.5.11, and taxonomic classifications are provided in Table 4-2. Single-carbon source media were prepared according to Section 4.5.1. To create library 1, we added monocultures of focal microbes to the single-carbon source media, and prepared droplets. To create library 2, we prepared droplets from monocultures of the unlabeled focals, environmental isolates, or base media. We then pooled the droplets and loaded across two replicate microwell array chips (Generation 1, operated by Chapter 2 Methods). The microwell array chips were

incubated at 30C using a temperature-controlled incubator, and timepoints were taken over the course of 48 hours.

*Derivation of liquid handling steps*

We aim to construct 960 co-cultures composed of 6 focal microbes, 5 carbon sources, and 32 environmental isolates and controls (Figure 4-5A). We assume that each method starts with (i) normalized monocultures of all bacteria, and (ii) each single-carbon source media.

To assemble these combinations by conventional methods, we first add each focal microbe (6) to each carbon source (5), requiring 60 liquid handling steps (= 6 × 5 × 2). We then add each focal-carbon mixture (30) to each environmental isolate or control (32), requiring 1,920 steps (= 30 × 32 × 2). Last, we duplicate all 960 combinations, requiring another 960 steps. In total, this requires 2,940 steps.

In comparison, our platform only requires 246 steps. As above, we first add each focal microbe (6) to each carbon source (5), requiring 60 liquid handling steps (= 6 × 5 × 2). We then add encoding dyes to all conditions (62 steps). Finally, we make droplets (62 steps), and pool droplets (62 steps).


# 4.5.10    Methods for *H. frisingense* co-cultures

Cultures of *H. frisingense* (tagged with GFP, Table 4-1) and environmental soil isolates I1, I2, I3 (Table 4-3 and Section 4.5.11) were prepared according to Section 4.5.2. Single-carbon source media were prepared according to Section 4.5.1. We prepared droplets such that each droplet received *H. frisingense*, 0 or 1 isolate, and single-carbon source media. We then pooled the droplets and loaded in a single $k=3$ microwell array chip (Generation 2, operated by Chapter 2 Methods). The microwell array chip was incubated at room temperature (in ambient air), and timepoints were taken over the course of 48 hours every 30 minutes.

*Derivation of liquid handling steps*

Following Chapter 2 Section 2.4.1, we can derive the number of liquid handling steps as follows. We assume that we start with (i) washed and normalized cultures of Hf, I1, I2, and I3 (ii) glucose, fructose, sucrose, and base media. Our goal is to assemble all 200 compositions in Figure 4-6, made up of [20 co-cultures] × [10 single and mixed carbon sources].

If using conventional methods, we first construct the 20 co-cultures each composed of four parts [1 part Hf + 1 part isolate $a$ + 1 part isolate $b$ + 1 part isolate $c$; where each part can be any isolate or base media]. This operation requires 80 (= 20 × 4) steps. Similarly, the 10 carbon source mixtures are [1 part carbon + 1 part carbon + 1 part carbon; where each carbon is either glucose, fructose, or sucrose]. This operation requires 30 (= 10 × 3) steps. Then, each of the 200 compositions requires 1 part co-culture and 1 part carbon mixture, which requires 400 (= 200 × 2) steps. Finally, if in 96-well plates we assume that all 200 compositions should be duplicated, requiring 1 additional pipetting step per composition (200 steps). Altogether, this requires 710 steps.

By using our platform, we only 68 steps, a >10-fold reduction. First, we prepared 4 co-cultures [1 part Hf + 1 part isolate or base media], requiring 8 (= 4 × 2 pipetting steps). Then we added the three carbon sources to each condition [1 part co-culture + 1 part carbon source], requiring 24 (= 4 × 3 × 2) steps. Next, we added encoding dyes (12 steps). Then we transferred to Bio-Rad QX200 cartridges to produce droplets (12 steps), and pooled droplets for all 12 conditions (12 steps).

124

**Table 4-2. Environmental bacterial isolates used in pilot microbial interaction screen.** Classifications were determined by 16S rRNA profiling via Sanger sequencing (~1000 nt in usable length). All samples were isolated and analyzed by Higgins *et al* [107]. Blank rows indicate samples where sequencing failed.

| | Phylum | Class | Order | Family | Genus | Isolation media |
|---|---|---|---|---|---|---|
| 1 | Actinobacteria | Actinobacteria | Actinobacteridae | *Micrococcineae* | *Arthrobacter* | Nutrient agar |
| 2 | Firmicutes | Bacilli | Bacillales | *Bacillaceae 1* | *Bacillus* | Nutrient agar |
| 3 | Firmicutes | Bacilli | Bacillales | *Bacillaceae 1* | *Bacillus* | Nutrient agar |
| 4 | Firmicutes | Bacilli | Bacillales | *Bacillaceae 1* | *Bacillus* | Nutrient agar |
| 5 | Firmicutes | Bacilli | Bacillales | *Bacillaceae 1* | *Bacillus* | Nutrient agar |
| 6 | Actinobacteria | Actinobacteria | Actinobacteridae | *Micrococcineae* | *Arthrobacter* | Nutrient agar |
| 7 | Firmicutes | Bacilli | Bacillales | *Bacillaceae 1* | *Bacillus* | Nutrient agar |
| 8 | Firmicutes | Bacilli | Bacillales | *Bacillaceae 1* | *Bacillus* | Nutrient agar |
| 9 | Firmicutes | Bacilli | Bacillales | *Bacillaceae 1* | *Bacillus* | Nutrient agar |
| 10 | | | | | | Nutrient agar |
| 11 | | | | | | Nutrient agar |
| 12 | Firmicutes | Bacilli | Bacillales | *Bacillaceae 1* | *Bacillus* | Nutrient agar |
| 13 | Actinobacteria | Actinobacteria | Actinobacteridae | *Micrococcineae* | *Arthrobacter* | Nutrient agar |
| 14 | Actinobacteria | Actinobacteria | Actinobacteridae | *Micrococcineae* | *Arthrobacter* | Nutrient agar |
| 15 | | | | | | Nutrient agar |
| 16 | | | | | | Nutrient agar |
| 17 | Firmicutes | Bacilli | Bacillales | *Bacillaceae 1* | *Bacillus* | Nutrient agar |
| 18 | Firmicutes | Bacilli | Bacillales | *Bacillaceae 1* | *Bacillus* | Nutrient agar |
| 19 | Firmicutes | Bacilli | Bacillales | *Paenibacillaceae 1* | *Paenibacillus* | Nutrient agar |
| 20 | Firmicutes | Bacilli | Bacillales | *Paenibacillaceae 1* | *Paenibacillus* | Nutrient agar |
| 21 | Firmicutes | Bacilli | Bacillales | *Bacillaceae 1* | *Bacillus* | Nutrient agar |
| 22 | Firmicutes | Bacilli | Bacillales | *Bacillaceae 1* | *Bacillus* | Nutrient agar |
| 23 | Actinobacteria | Actinobacteria | Actinobacteridae | *Micrococcineae* | *Arthrobacter* | Nutrient agar |
| 24 | Actinobacteria | Actinobacteria | Actinobacteridae | *Micrococcineae* | *Arthrobacter* | Nutrient agar |
| 25 | | | | | | Nutrient agar |
| 26 | Firmicutes | Bacilli | Bacillales | *Bacillaceae 1* | *Bacillus* | Nutrient agar |
| 27 | Firmicutes | Bacilli | Bacillales | *Bacillaceae 1* | *Bacillus* | Nutrient agar |

**Table 4-3. Environmental bacterial isolates used in *H. frisingense* co-cultures.** Classifications were determined by 16S rRNA profiling via Sanger sequencing (~1000 nt in usable length).

| | Phylum | Class | Order | Family | Genus | Isolation media |
|---|---|---|---|---|---|---|
| I1 | Proteobacteria | Beta Proteobacteria | Burkholderiales | *Burkholderiaceae* | *Burkholderia* | Brucella agar |
| I2 | Proteobacteria | Beta Proteobacteria | Burkholderiales | *Burkholderiaceae* | *Burkholderia* | Tryptic soy broth |
| I3 | Proteobacteria | Gammaproteobacteria | Enterobacteriales | *Enterobacteriaceae* | *Rahnella* | Streptomyces medium |

# 4.5.11    Environmental isolate collections and methods

*Environmental isolates in Section 4.3.5 – A pilot microbial interaction screen shows common facilitation*

These environmental isolates were collected by Higgins *et al.* [107]. I will briefly reproduce the methods here, and the reader can refer to [107] for more information. Strains were isolated from a single grain of soil obtained in Cambridge, MA in September 2015 on nutrient agar. Colonies were grown in liquid culture (48 hours, nutrient broth), re-plated for purity, and finally stored as glycerol stocks (-80C). For identification, the 16S rRNA was sequenced (Sanger, ~1100 nt of useable length). Isolates were selected for use in the pilot screen based on their ability to reliably revive from glycerol stocks. Table 4-2 shows the final strain set used.

*Environmental isolates in Section 4.3.6 – Our platform aids exploration of interactions within a synthetic community*

A soil sample was collected from the Middlesex Fells Reservation in Stoneham, MA in November 2017 and diluted in phosphate buffered saline (PBS) within a few hours of collection (5 g soil vortexed in 40 mL PBS). Single strains were isolated from streaking 70 µL of dilutions of this mixture ($10^{-1}$, $10^{-2}$, $10^{-3}$, and $10^{-4}$) on 20 agar media (Tryptic Soy Broth (TSB), 1% TSB, Lysogeny Broth (LB), 1% LB, Nutrient Broth (NB), 1% NB, M9 salts + 0.5% glucose, M9 salts + 0.005% glucose, M9 salts + 0.005% glucose + 0.2% casamino acids, M9 salts + 0.005% glucose + 0.002% casamino acids, M9 salts + 0.5% glucose + 0.2% casamino acids at pH = 4 and 5, M9 salts + 0.005% glucose + 0.002% casamino acids at pH = 4 and 5,

Actinomycete Isolation Agar, Brucella Agar, Streptomyces Medium, Campylobacter Medium, Blood Agar, and ATCC Medium 1111). Strains were selected based on the following criteria: growth in LB liquid media of transferred colony (25 C), frozen glycerol stock revival in LB (OD600 > 0.1) (30 C), and subsequent growth on M9 + 0.5% glucose (OD600 > 0.1) (30 C). This procedure produced 90 environmental isolate glycerol stocks (LB, 25% glycerol) organized in a 96-well plates and stored in -80 C. For the experiment in Section 4.3.6, we chose three strains based on ability to grow in sucrose, fructose, or glucose (see Figure 4-6B). Table 4-3 shows the three isolates selected.
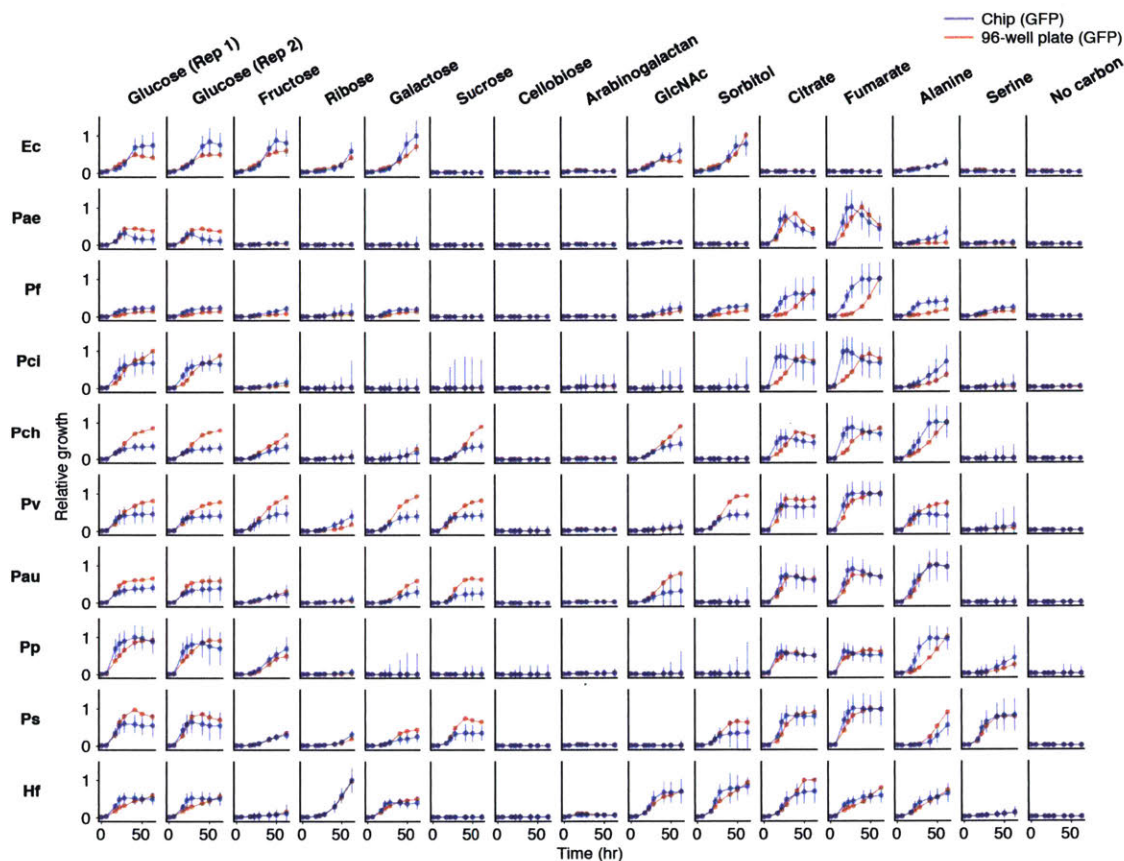
# 4.6 Supplemental Figures



**Figure 4-7. Growth curves of microbes on single-carbon source media.** At each timepoint, points represent the median, and error bars represent standard deviations of the distribution of GFP measurements across all microwells sharing the same microbe and carbon source (median number of microwells = 66.5). For each microbe, relative measurements are normalized by subtracting background and dividing by the maximum across the fifteen carbon sources and all timepoints.
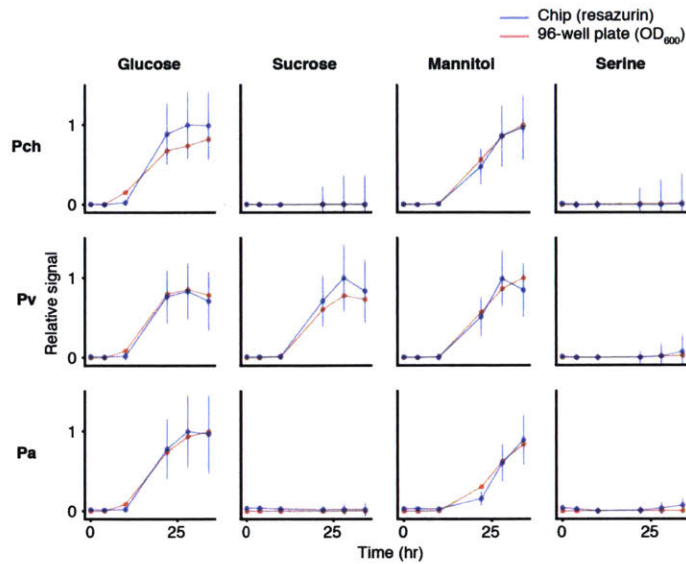
**Figure 4-8. Growth curves of microbes on single-carbon source media measured by resazurin assay**. At each timepoint, points represent the median, and error bars represent standard deviations of the distribution of resorufin measurements across all microwells sharing the same microbe and carbon source (median number of microwells = 44). Error bars represent standard deviations across microwells. For each microbe, relative measurements are normalized by subtracting background and dividing by the maximum across all carbon sources and timepoints.
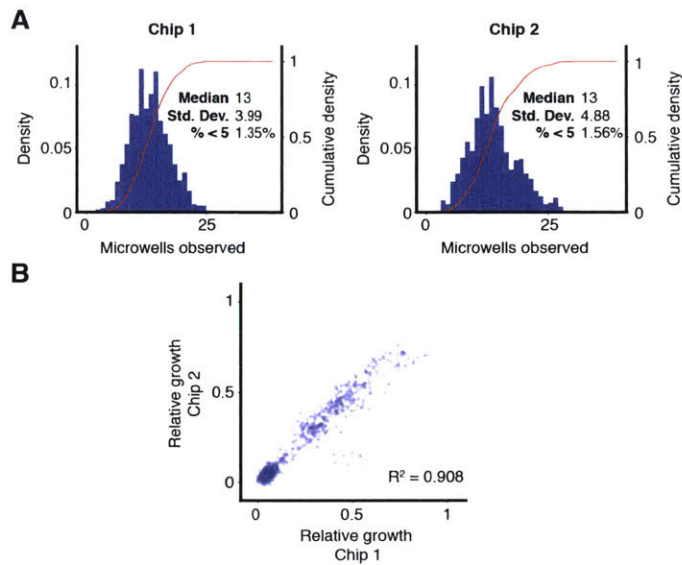
**Figure 4-9. Pilot microbial interaction screen technical performance.** The pilot microbial interaction screen constructed 960 combinations of microbes and carbon sources on two replicate microwell array chips ("Chip 1" and "Chip 2"). (**A**) The histogram (blue bars) and cumulative distribution (red line) of the number of microwells observed on each chip for each unique combination of droplets from library 1 (focal microbes + carbon sources) × library 2 (isolates and controls). (**B**) A scatterplot of relative growth values measured after 26 hours from each chip, as an assessment of technical variation. Each point corresponds to a unique combination of library 1 × library 2 (Figure 4-5B, C reports the average of values from Chip 1 and Chip 2). Points are shown at alpha = 0.25 to density. Relative growth is computed by background subtraction and normalization to the maximum GFP value on each chip.

# Chapter 5

# Future directions

*I hope that this chapter can serve as the starting point for anyone who continues the thread of work in this thesis, and includes proof of concept and discussion of new technical directions of our platform. As many of these ideas were developed in collaboration with others, I chose to highlight them individually in each section.*

## 5.1.1 Introduction

Throughout this thesis, I explained how three basic design concepts have governed the development of this technology: accessibility, generalizability, and scalability, with generalizability further divided into assay scope and input scope (Chapter 1, Section 1.3.1). Here, I will use the lens of these design principles to suggest new developments of our platform aligned with each chapter, first focusing on general technical development (Chapter 2), and then developments that can enable new directions in combinatorial drug screening (Chapter 3), or microbial ecology (Chapter 4). As future directions are also more broadly and concisely reviewed in each individual chapter, I focus discussion here on directions with supporting proof of concept.

## 5.2 Future directions for technical development of the platform

As Chapter 2 focused on the technical development of the platform, here I will review two strategies to improve scalability, including the efficiency by which combinations are constructed, and the performance of the optical encoding of droplet contents.

1. *Scalability: can undesired combinations of inputs be avoided to improve efficiency?* Although all combinations of the inputs are constructed, some might be unnecessary or undesired. For example, in screening a library of drugs across a library of cell lines, combinations of *(i)* drugs with no cells, and *(ii)* cells with no drugs will also be constructed.

2. *Scalability: can a different encoding strategy scale to larger input libraries?* The encoding strategy used throughout this thesis – distinct ratios of fluorescent dyes – does not scale to very large libraries (*e.g.* 10,000-100,000 unique inputs).
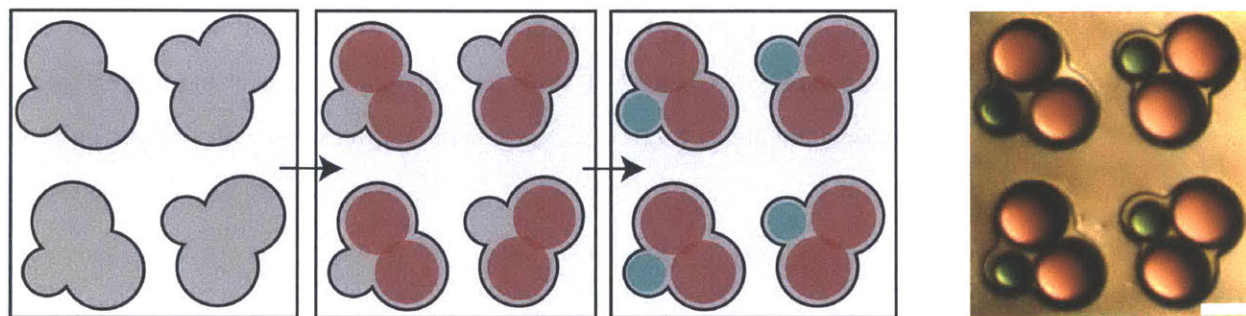


**Figure 5-1. Ordered addition by droplet size exclusion.** In the case where only certain combinations are desired, microwells can be designed to exclude droplets by size, and droplet libraries can be iteratively loaded. At right, a micrograph of droplets loaded by sequential addition, avoiding blue × blue droplet combinations. Scale bar equals 100 μm.

# 5.2.1 Scalability: improving efficiency via size-encoded droplet libraries

In its current form, the microwell array randomly captures droplets to construct all combinations of inputs. This design is advantageous if the user desires all combinations of the inputs, but many experiments can be factored into *[library 1]* × *[library 2]* × ... × *[library N]*, and *[library i]* × *[library i]* ... × *[library i]* conditions (for the same *i*) are not of interest. For example, a drug screening experiment to measure *[drugs]* × *[cell lines]* also constructs *[drugs]* × *[drugs]* and *[cell lines]* × *[cell lines]* combinations, resulting in a 50% loss in efficiency.

To solve this problem, each input library can be emulsified into droplets of different sizes. Microwells can be designed as a set of "slots," that exclude droplets larger than a given size threshold – each slot corresponding to droplets for a given library (Figure 5-1). By loading the droplet libraries in sequence from largest to smallest size, only the desired combinations will be assembled. If droplets of different sizes can be produced using a commercial instrument such as the Bio-Rad QX200 (limited to one size; used throughout this thesis), then this strategy would not sacrifice the accessibility of the platform.

To test this strategy, we designed microwells to accept two larger droplets (1-nL droplets, red) and one smaller droplet (100-pL droplets , blue) and demonstrated successful sequential loading (Figure 5-1), avoiding combinations of blue droplets.

Beyond this proof of concept, it remains to be seen how many distinctly sized droplet libraries can be produced. Microfluidic flow-focusing methods typically produce a size distribution of droplets with ~5% coefficient of variation (on diameter), and the pooling of droplets by micropipette likely increases the variance of the size distribution. The possible number of distinctly sized droplet libraries is constrained by (*i*) the total size range that can be constructed by microfluidic flow-focusing (or other droplet production methods); and (*ii*) the number of non-overlapping size "bins" that can be fit in this range.
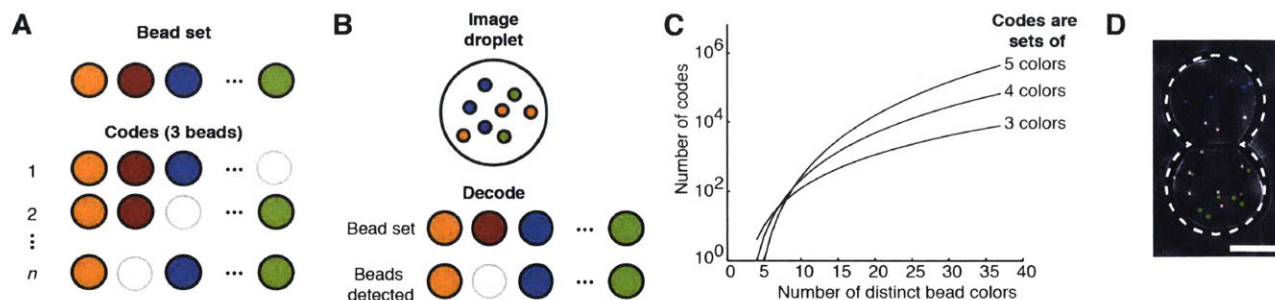
**Figure 5-2. A strategy for higher complexity optical encoding.** (**A**) Codes are created from all subsets of $k$ beads from a total set of $n$ distinguishable bead colors. (**B**) Droplet contents are decoded by the presence-absence of bead colors. (**C**) The expected encoding complexity generated by codes with subsets of 3, 4, or 5 colors, as a function of total number of distinguishable bead colors, $n$. (**D**) A fluorescence micrograph of a microwell containing two 1-nL droplets in a Generation 1 $k=2$ microwell, loaded with 3-μm fluorescent beads. The scale bar indicates 75 μm.

## 5.2.2 Scalability: an optical encoding strategy for 10,000+ inputs

*This encoding method was originally proposed by David Feldman, and we subsequently collaborated to develop it.*

While encoding reagents with distinct ratios of fluorescent dyes is simple and sufficient for the applications described in this thesis, some new applications may require a far larger number of codes than can be achieved with this method. For example, droplet-based single compound screening in $k=1$ microwells could require an optical encoding method with straightforward scaling to 10,000+ distinct compounds. In order to maintain accessibility, it is important that the encoding method be compatible with low-magnification fluorescence microscopy.

Rather than using ratios of fluorescent dyes to encode reagents, one can create 3-μm beads carrying distinct ratios of three fluorescent dyes (Figure 5-2). As it was straightforward to create 60+ distinguishable colors with free dye, we expect this can be similarly achieved with minimal technical risk. For example, one possibility is to incubate streptavidin-coated beads with ratios of biotin-labeled dye. To create codes, we can assign each reagent in the library to a unique subset of these beads. Therefore, droplets carrying different reagents can be distinguished by the presence/absence of each distinct bead color. This encoding method achieves the required complexity for libraries of 10,000-100,000 conditions (Figure 5-2C).

134

# 5.3 Future directions for combinatorial drug screening

Chapter 3 describes a combinatorial drug screen to discover compounds that potentiate the activity of antibiotics against the model Gram-negative pathogen *E. coli*. While successful in discovering novel drug combinations that may be of use in antibiotics research and development, this demonstration could be extended to improve its generalizability and scalability.

1.  *Generalizability - assay scope*: The need to engineer cells to constitutively express a fluorescent protein can hinder some applications, such as direct screening of bacteria isolated from clinical samples. Can label-less growth assays be developed?

2.  *Generalizability - input scope:* Many areas of human health could benefit from combinatorial drug treatments. While the examples in this thesis revolve around bacteria, can screening be performed on mammalian cells?

3.  *Scalability:* An alternative method for attacking the scale required for combinatorial screening involves pooling of compounds and algorithmic deconvolution of hit combinations from pools. Can these methods be adopted to our platform?
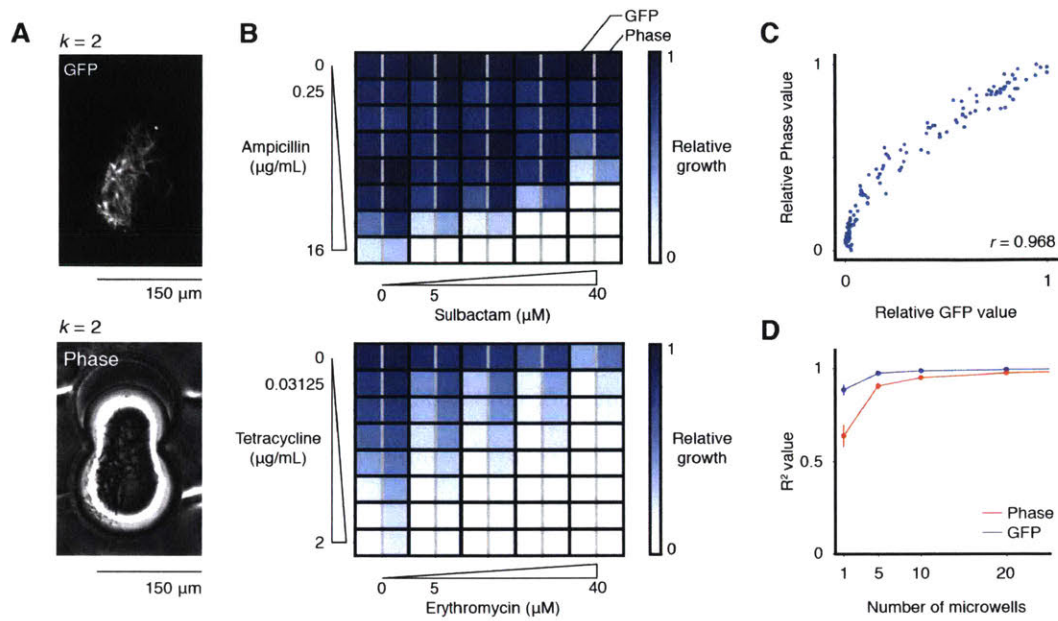
4.



**Figure 5-3. Label-less growth assay using phase contrast microscopy.** (**A**) For comparison, both GFP and phase contrast measurements can be collected from the same microwell. (*Top*) Fluorescence and (*Bottom*) phase contrast micrographs (10X magnification; all other data was collected with 4X magnification) show a *k*=2 microwell containing *E. coli* (with constitutive GFP expression) and the antibiotic ampicillin. (**B**) (*Top*) Sulbactam × ampicillin and (*Bottom*) erythromycin × tetracycline checkerboards (similar to Figure 3-4) in *E. coli* collected from the same microwell array chip. The interleaved heatmap compares responses measured by GFP (left interleaved column) and phase contrast (right interleaved column). Measurements are normalized by subtracting the minimum and dividing by the maximum across all dose combinations measured. (**C**) A scatterplot of relative growth values measured by GFP and phase contrast across all dose combination assay points, including those shown in part B. Each point shows the median signal across all microwells sharing the dose combination assay point. The Pearson correlation is denoted by *r*. (**D**) To compare the assay noise of GFP and phase contrast, we measured the relationship of between microwell-level replication and technical noise ($R^2$ value between bootstrap-resampled data in part C, as in Figure 3-1E) for each measurement method.

# 5.3.1 Assay scope: growth assays without engineering fluorescence

*This work was performed in collaboration with Gowtham Thakku and Prianca Tawde.*

While the drug screening performed in Chapter 3 required model bacterial pathogens that have been engineered to constitutively express a fluorescent protein, this presents a barrier to some applications. For example, antibiotics development can benefit from experimenting on banks of drug-resistant clinical isolates where the need to engineer fluorescence could be a significant hindrance. Moreover, some microbes may be genetically intractable. In contrast, microbiology widely uses optical density ($OD_{600}$) to measure cell growth, due to its generality.

We piloted an assay that works by a similar principle based on phase contrast microscopy (Figure 5-3). This microscopy technique amplifies the light scattered from cells, making them visible against the transparent background. Cell density can be estimated by measuring the "roughness" of the image within the droplets (Figure 5-3A).

To test our method, we created drug response checkerboards in *E. coli* using the antibiotics and potentiators used in Chapter 3, sulbactam × ampicillin and erythromycin × tetracycline (Figure 5-3B) using a $k=2$ microwell array chip. We measured GFP and phase contrast signal from each microwell (Figure 5-3A). Overall, the GFP and phase contrast measurements showed a strong correlation (Pearson correlation = 0.968), although phase contrast had more sensitivity to low relative growth values (Figure 5-3C).

To compare the technical noise of both methods, we repeated the analysis in Figure 3-1E to examine the relationship between the number of microwells observed and $R^2$ value between technical replicates (Figure 5-3D). While GFP shows less technical noise, phase contrast approaches the same technical noise levels when more than five replicate microwells are observed per condition.

Limitations of the phase contrast method compared to fluorescence include throughput and generalizability to different microbes. While optical resolution is not limiting for fluorescence assays, empirically we found that phase contrast worked best when using 1.625 μm / pixel resolution (compared to 6.5 μm / pixel resolution for GFP measurements). Higher magnification (4X) requires a smaller field-of-view and overall slower scanning. Second, different microbes likely have different morphologies, and empirically we found that image processing parameters have to be tuned for each microbe. We expect that applying supervised machine learning methods to this image processing task could alleviate this issue. However, for these

reasons, the resazurin assay developed in Chapter 4 Figure 4-4 is likely a better solution for label-less growth assay than the phase contrast method.
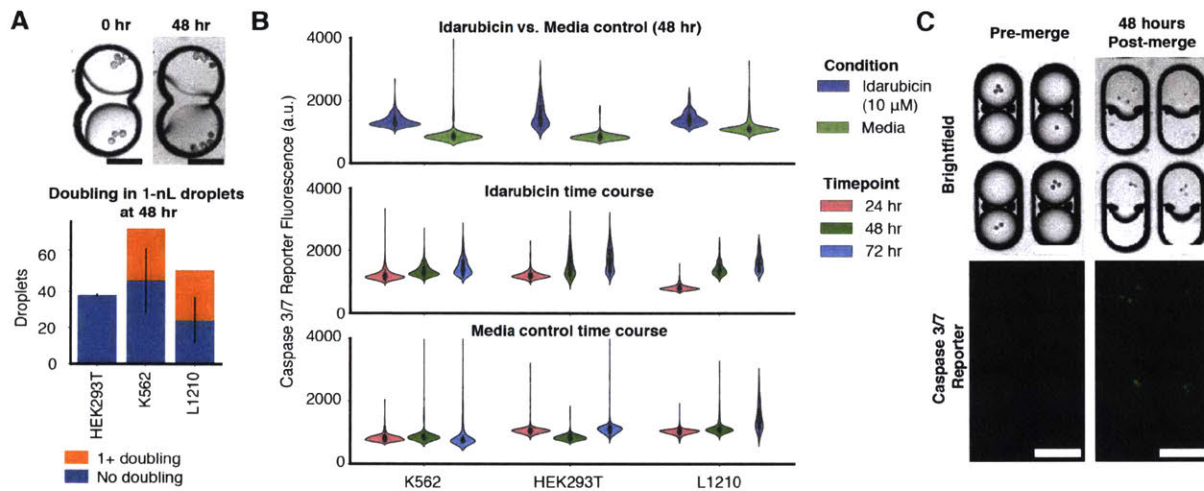


**Figure 5-4. Adapting our platform for mammalian cell culture.** (**A**) Three mammalian cell lines were tested in the droplet platform: *(i)* HEK293T derived from the human embryonic kidney; *(ii)* K562 derived from a human chronic myeloid leukemia; and *(iii)* L1210 derived from a mouse lymphocytic leukemia (1.78 × 10⁶ cells / mL in DMEM). Cell doublings in droplets were manually counted after 48 hours. Micrographs show K562 cells in droplets, with scale bars equal to 75 μm. Error bars are standard deviation estimated from a binomial model. (**B**) We developed a droplet-compatible apoptosis assay using a caspase 3/7 reporter (ThermoFisher CellEvent) that can be added to media and emulsified with cells. (Top panel) Violin plots of caspase 3/7 reporter signal from cells treated with topoisomerase II inhibitor idarubicin (10 μM) or a no-treatment control ("Media") at 48 hours in droplets. (Middle, Bottom panels). Time courses of caspase 3/7 reporter signal over 72 hours in treatment and no-treatment controls. (**C**) To construct pairwise drug combinations, droplets paired in microwells are merged by electro-coalescence. Merging droplets via electro-coalescence was toxic to all three cell lines tested. Compared to part A, where droplets are not merged, we detected no doublings of cells at 48-hours post-merge. Scale bars represent 150 μm.

# 5.3.2 Input scope: adopting platform to mammalian cell culture for applications to oncology and beyond

*This application was developed in collaboration with Juan Hurtado, who carried out the experiments presented here. It has since been further developed by FuNien Tsai, Cheri Ackerman, and Anne-Florence Blandin. Cell lines and much of the original motivation of this direction was also contributed by the labs of Mimi Bandopadhayay, Rameen Beroukhim, and Keith Ligon.*

To adapt the droplet platform to mammalian cell lines we developed a compatible cell-death assay and identified factors affecting cell viability. Building off of previous work to establish mammalian cell culture in droplets [52], [53], [61], we chose as models three mammalian cell lines in both suspension and adherent culture: HEK293T derived from human embryonic kidney (adherent); K562, derived from human myeloid leukemia (suspension); and L1210 derived from mouse lymphocytic leukemia (suspension). We found that suspensions cells (K562, L1210) continued dividing in 1-nanoliter droplets, but the adherent cell line HEK293T did not (Figure 5-4A). However, this cell line still appeared to report a drug response over 48 hours (Figure 5-4B).

In the system as currently configured, reagents cannot be added to droplets after loading into the array. Therefore all the components of a compatible cell death assay must be present in the droplets from the start of an experimental time course, and not adversely affect cell viability. We compared ethidium homodimer (a DNA intercalator that stains dead cells, regardless of death mechanism) and a caspase 3/7 reporter (ThermoFisher CellEvent) to specifically report apoptosis. We found that the required concentrations of ethidium homodimer for assay endpoints were toxic (data not shown), but the caspase 3/7 reporter successfully reported apoptosis induced by the topoisomerase inhibitor idarubicin (10 μM) compared to no-treatment controls (Figure 5-4B).

While we achieved successful droplet culture and assay readout, we identified that application of the high voltage AC electric field used to merge droplets and construct drug combinations was toxic to all three cell lines (Figure 5-4C). This result suggests merging parameters (electro-coalescence field strength and frequency) must be optimized and alternative merging strategies should be explored. Such alternatives could include chemically-induced merging (pulsed perfluorooctanol in fluorous oil continuous phase) or mechanical perturbation (acoustic waves) [37], [38]. However, there is evidence from other studies that there are parameter regimes for electro-coalescence that do not perturb mammalian cells [52].

Another foreseeable challenge is the expected screening throughput and data quality. Density limits on mammalian cell culture ($\sim 10^6$ cells / mL) suggest that droplets should not be loaded with much more than a single cell [61]. Therefore, one might expect that to measure a phenotype with enough statistical power for high throughput screening could require measuring thousands of droplets. Indeed, Baret and colleagues found that achieving equivalent statistical power to conventional microplate culture in a gene-expression reporter assay required measuring 7,500 cells [53]. Following the models in Chapter 2, Section 2.6.10 and Figure 2-7, if microwells are positioned at a density of $\sim 10^3$ microwells / cm$^2$ and a replication level of $\sim 10^3$ microwells / combination are required, one would expect to achieve at best the same imaging throughput of a 96-well plate ($\sim 1$ combination / cm$^2$; we assume fixed imaging rate per unit area). As a result, assay development for high throughput screening should focus on measuring and improving the expected assay noise or microwell density. Alternatively, our platform may be more useful for low-input drug-testing applications (*i.e.* testing on primary cells) that currently cannot be conducted in a 96-well plate format due to requirements for millions of cells.

# 5.3.3 Scalability: Improving throughput with pooled combinatorial drug screening

*This application was developed in collaboration with Jared Kehe.*

An alternative strategy to reduce the logistical complexity of pairwise combinatorial drug screening is to distribute compounds across a multiplicity of "pools," such that all pairwise interactions within a given pool can be tested simultaneously [86]–[88]. Assuming that hits are produced by sparse pairs of compounds, one can then deconvolute the active pair of compounds from a "hit" pool by deduction: pairwise interactions in any pool that do not report a "hit" signal can be eliminated from consideration. This deconvolution strategy might be further improved by statistical methods for solving underdetermined systems such as "compressed sensing."

This strategy could be applied on our platform without any further technical development, as a user could use a microwell array of $k=k_0$ to construct random pools of size $k_0$. The platform might further aid in deconvolution, as compounds can be iteratively grouped in smaller pools until the hit pairs of compounds are confirmed by constructing pairwise combinations in $k=2$ microwells. Future work to develop this should start with refining the statistical methods for deconvolution, including how to choose the appropriate pool

140

size and sampling needed [139]. These factors will determine the overall throughput increase of this method compared to brute-force screening of pairs of compounds.

# 5.4  Future directions for microbial ecology

Chapter 4 describes the use of the platform to explore interactions between strains in microbial communities. However, experiments were limited by the ability to measure only a single strain in each community. For example, by only measuring the abundance of one strain, current measurements cannot distinguish mutualistic from parasitic interactions. This property limits the generalizability (assay scope) of the platform.
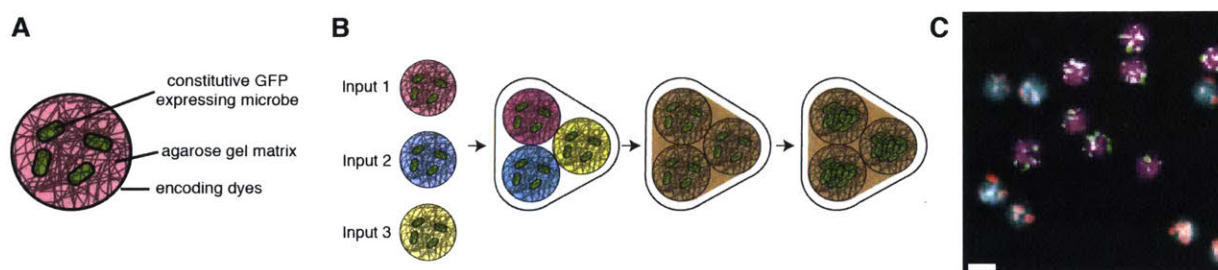


**Figure 5-5. Multiplexed growth assays by spatial confinement of cells in gel beads.** (**A**) Agarose gel beads carrying microbes that constitutively express GFP can be emulsified with encoding dyes. (**B**) Microwell arrays can be loaded with droplets carrying agarose gel beads, and droplets can be merged according to standard methods. Microbes remain confined by the agarose matrix while still consuming nutrients or secreting signaling factors into the surrounding aqueous droplet. (**C**) A fluorescence micrograph of *E. coli* confined to agarose gel beads while incubated in LB media (6 hours, 37C) in a 384-well plate. Two different sets of 0.5% w/v dye-labeled agarose gel beads (magenta or cyan) were loaded with *E. coli* that constitutively expresses GFP (green) or mCherry (red). Scale bar corresponds to 100 μm.

# 5.4.1 Assay scope: multiplexed measurements across different cellular inputs

*This concept was developed in collaboration with Navpreet Ranu and Jared Kehe.*

Many potential applications would benefit from simultaneous measurement of responses across different cellular inputs. In Chapter 4, measurements of microbial interactions are limited to the measurement of abundance a GFP-labeled strain, or to total biomass accumulation (*i.e.* across all present strains in a merged droplet) using a general label of metabolic activity such as resazurin. This means that current measurements cannot distinguish mutualism (in which both interacting strains benefit) from commensalism or parasitism (in which only one benefits, with no or negative effects on the symbiotic partner).

Currently, measuring the abundance of each strain would require labeling each with a distinguishable fluorescent protein. However, interference from the fluorescent encoding dyes limits the number of available fluorescence channels.

A different strategy could measure the same fluorescent protein (*e.g.* GFP) across all strains but use spatial information to assign the signal measured to each distinct strain (Figure 5-5). To create this spatial information, an agarose gel matrix can confine the growth of cells [140]. The ~100 nm pore size of this hydrogel would allow the exchange of signaling molecules and consumption of nutrients, but restrict cells to their original position in the microwell (Figure 5-5B) [140]. Construction of these agarose beads is straightforward and already established, and integrates well with our existing protocol. Molten 0.5% w/v ultra-low melt agarose is mixed with each sample prior to emulsification, and droplets are made according to protocols in Chapter 2. Emulsions are then stored at 4C for 1 hour to induce gelation.

As a proof of concept, we created 0.5% w/v agarose beads in 1-nL emulsions carrying *E. coli* constitutively expressing either GFP or mCherry from Cy3- or BDP-labeled ultra-low melt agarose respectively (Figure 5-5C). We then broke the emulsion by electro-coalescence and pooled the gel beads, and incubated them together in LB media in a 384-well plate for 6 hours. Both GFP and mCherry labeled *E. coli* grew to punctate colonies and remained restricted to their respective agarose beads (Figure 5-5C).

Use of agarose beads may also eliminate the need to use fluorescence to detect cell abundance. Due to confinement by the gel matrix, cells grow in punctate colonies that can be identified with low magnification brightfield microscopy [140].

Future work to develop this strategy should determine the compatibility of hydrogel chemistries such as agarose with different microbes. Many microbes may express agarase enzymes that can degrade the matrix, allowing their escape and thus losing the spatial information needed. Other gel matrices could be explored, or these microbes could be identified and excluded from experiments using this strategy.

# 5.5 Future directions for microfluidics: self-assembly of particles, cells, and fluids

While the previous sections of this chapter addressed specific improvements to our platform, how can these design principles be generalized and applied to other microfluidic platforms? More generally, where might the field of microfluidics evolve?

The core concept underlying the technology of this thesis is the self-assembly of combinations of microfluidic droplets, and this autonomous nature is the root of the accessibility and scalability of our design. Because the droplets self-assemble, the platform can be operated with conventional micropipettes improving its accessibility. Because the self-assembly easily parallelizes across more than tens of thousands microwells, the platform is robust and scalable. In Chapter 1 (Section 1.3) I reviewed how the limited accessibility, generalizability, and scalability of microfluidic platforms have hindered the adoption of these platforms across the broader life sciences community [48]. I predict that further developing self-assembly as a design paradigm will improve these necessary features in microfluidic platforms, and ultimately will dramatically strengthen our interface to molecular and cellular biological systems.

Whitesides and Grzybowski define "self-assembly" as "the autonomous organization of components into patterns or structures without human intervention ... that can be controlled by proper design of the components" [141]. While self-assembly usually describes systems of molecules and solid particles, here I extend the definition to also consider self-assembly of emulsions. There is not a concise label for systems that are not self-assembled because it should be clear that almost all systems currently designed by humans at length scales > $10^{-3}$ m do not have these properties. These systems are serially assembled component-by-component by an external instrument (a human or a robot) following a series of instructions. This is because it is easy for us to think about each component of a system in relation to the whole, but hard to picture the whole from only knowledge of each component's relationship to other components. Consider trying to build a chair using only a list of angles and distances between each pair of pieces.

Self-assembly finds its roots in chemistry and biology, and can be found at all scales of biological systems. At the biomolecular scale, proteins self-fold into functional structures, and still further self-assemble into larger complexes such as a microtubule. In multicellular organisms, cells divide from a single source cell,

144

autonomously differentiating into various functional types that assemble the larger multi-cellular tissues and organism.

Advantages offered by self-assembly are also easy to see in biological systems:

- *Parallelization:* Assembly happens simultaneously and is easily parallelized. Alternatively, non-self-assembled systems can be bottlenecked by the speed of the external instrument that operates the system (*e.g.* a robot arm or a conveyor belt).

- *Robustness:* With assembly occurring in parallel, the effect of a defect in one component is limited and does not affect the larger system. In non-self-assembled systems, a defect in the external instrument that operates the system affects all components.

- *Self-healing:* Because the components contain all necessary information to form the desired final system, the ability to repair the system is retained after assembly, *e.g.* a DNA duplex that re-assembles after melting.

Self-assembly has begun to emerge as an important design and manufacturing paradigm in unexpected fields. One example is in electronics manufacturing [142]. Conventionally, manufacturers use so-called "pick-and-place" machines: a robot that automatically places an incoming feed of circuit components into pre-designed slots on a printed circuit board. While these machines can work at very high speeds (~1-10 components / s), their serial nature means that they are limited by the throughput of the conveyor belts and robotic head and vulnerable to damage of any of these components [142]. Additionally, assembly at small scales (10-100 μm) becomes very slow and difficult to control [142]. In contrast, "fluidic self-assembly," manufactures circuits in parallel by flowing a slurry of circuit components embedded on shaped particles over a circuit substrate with correspondingly-shaped slots for each device [143]. The parallel nature of this method improves its scalability and robustness [143].
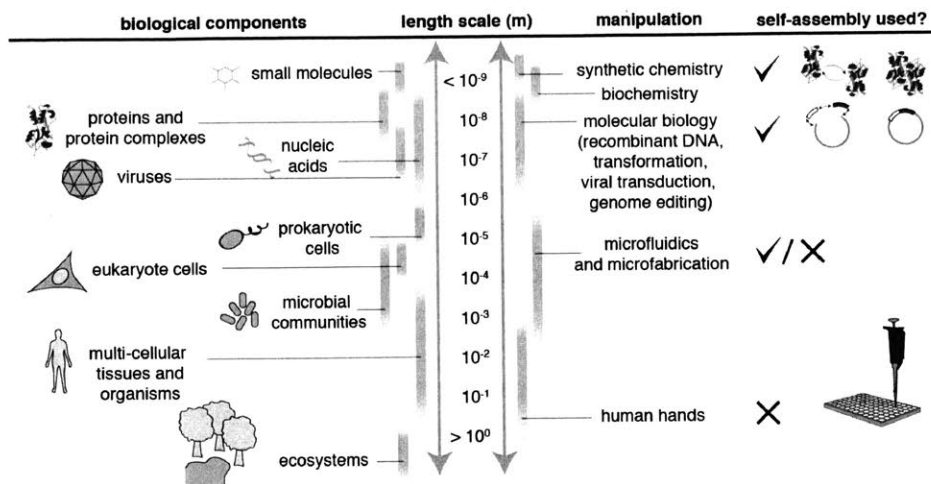
**Figure 5-6. Length scales divide the use of self-assembly approaches to manipulate biological systems.** Microfluidic platforms operate length scales between where self-assembly and non-self-assembly strategies dominate.

In the tools we use to manipulate biological systems, the use of self-assembly is divided by length scale (Figure 5-6). At length scales below ~$10^{-6}$ m, where means of manipulation are the tools of chemistry and molecular biology, we embrace self-assembly. For example, self-assembly underlies the interactions between proteins to turn on transcription of a gene, or the assembly of fragments of DNA in a plasmid. At length scales of $10^{-3}$ m and greater, the opposite is true: we use micropipettes to pick-and-place liquids between different vessels. Automation for high throughput screening requires the analog of robotic pick-and-place machines: robotic liquid handlers.

At intermediate length scales of $10^{-6}$-$10^{-2}$ m, microfluidic platforms are split in their use of self-assembly. Integrated microfluidic devices that manipulate fluids with pneumatic valves and pumps essentially miniaturize the "picking and placing" (routing) of fluids as done at larger length scales. For example, an integrated microfluidic platform to construct pairwise drug combinations as described in this Chapter 3 programmatically routes each input along rows and columns into a grid of chambers [25]. Instead, in our platform the combinations of droplets self-assemble in a microwell scaffold, gaining improved accessibility and scalability.

146

Microfluidic platforms that use a synthesis of these methods to control cells, biomolecules, small and molecules could ultimately grant experimenters with unparalleled spatial and temporal control of complex assemblies of cells, biomolecules, and small molecules. How can microwell scaffolds be modified to achieve more functionality? One can imagine that more complex control can be achieved using microwells with distinct sizes and shapes to capture matching emulsions or microparticles. As a starting point, Section 5.2.1 describes a proof of concept for assembling combinations of distinctly sized droplets. Moreover, multiple methods have been introduced to create precisely shaped, porous hydrogel microparticles [144], [145]. These particles can be patterned with small molecules, proteins, and other biomolecules, and can even carry cells. Kim and colleagues demonstrated the microwell-templated self-assembly of complex multicomponent structures, iteratively assembled from hydrogel particles of different sizes and shapes [146]. As a proof of concept, they used this technology to study human neutrophil chemotaxis by spatially patterning chemoattractant-laden microparticles. Substituting microwells for microchannel "rails" can even passively guide the movement of particles or full assemblies, suggesting a new principle for dynamic, directed transport of cells, microparticles, or even droplets [147]. Fusing these technologies with multi-phase fluids, for example by patterning surfaces to be selectively hydro-, lipo-, or fluorophilic, or inventing methods to stabilize custom-shaped emulsions, suggest generalizable strategies for assembling fluids and particles on the microscale.

An even more powerful strategy for self-assembly is afforded by the generalizability of DNA hybridization and corresponding methods to template microparticles, cells, and even oil droplets, with DNA. By tagging these components and optionally a corresponding scaffold with complementary single-stranded DNA oligomers, their interactions can be programmed to assemble complex structures. DNA-mediated self-assembly has been demonstrated to template both single-cells or hydrogel beads on surfaces, and moreover, to program interactions between single-cells to assemble into complex 3-dimensional tissues [148], [12], [149]. Other groups have also demonstrated the ability to use DNA hybridization to program interactions between oil-in-water emulsions [150], [151]. While the requirement of oil as the dispersed phase is limiting (biology is water based), this suggests that the invention of DNA-templated water-in-oil-in-water double emulsions would enable a general platform for DNA-programmed handling of microfluidic water droplets. Furthermore, DNA nanotechnologies like toe-hold switches could afford dynamic control over systems programmed by DNA-templated self-assembly [152].

In the long term, I envision that many of the basic operations of molecular and cellular biology, such as assembly and mixing, splitting, selection, and sorting might be programmed by self-assembly of cells, particles, and emulsions. In this thesis, I demonstrated how leveraging self-assembly considerably simplifies the operations of assembling combinations of reagents for applications in drug screening, microbial ecology and other applications, but this represents only a small step towards this greater vision.

# 5.6 Methods

## 5.6.1 Production of size-encoded droplet libraries

We produced two libraries of droplets of different sizes, 1-nL (~130 μm diameter; red food coloring in water) and 0.1-nL (~60 μm diameter; blue food coloring in water). As the continuous phase, we used a fluorous oil (Novec 7500, 3M) and 2% w/w fluorosurfactant (008-Fluorosurfactant, RAN Biotech).

To produce 1-nL droplets, we used Bio-Rad QX200 cartridges. These cartridges use a microfluidic flow-focusing architecture for droplet production. Since Bio-Rad QX200 cartridges only produce 1-nL droplets, to make the 0.1-nL droplets, we used a microfluidic droplet production device (PDMS, fabricated from a SU8-2050 on a silicon wafer) with a 40-μm flow-focusing nozzle.

The microwell array chip was designed and fabricated according to methods in Chapter 2.

Loading of the chip was also done as described in Chapter 2, first with the 1-nL droplets, and then after draining the droplets, we repeated with the 0.1-nL droplets.

## 5.6.2 Fluorescent beads for high-complexity optical encoding

For proof of concept, beads with distinct fluorescence profiles were made from 3-μm streptavidin-coated polystyrene beads (Bangs Labs), and biotin-labeled dyes (FAM, Cy3, and Cy5). Beads were incubated at 1 mg/ml (~0.1% w/v) in 10uM biotin-dye in "bind and wash buffer" (10 mM Tris-HCl, 1 mM EDTA, 2M NaCl, 1% Tween-20) for 1 hour at room temperature on a rotator to prevent bead settling. Beads were separated by centrifugation and washed twice in "bind and wash buffer."

Imaging of beads were performed with 10X magnification on Nikon Ti-E inverted fluorescence microscope with fluorescence excitation by a Lumencor Sola light emitting diode illuminator (100% power setting), and Hamamatsu ORCA-Flash 4.0 CMOS camera.

## 5.6.3 Mammalian cell culture

The cell lines used throughout this work were *H. sapiens* embryonic kidney cells (HEK293T, ATCC #CRL-3216), *H. sapiens* chronic myelogenous leukemia (K562, ATCC #CCL-243), and *M. musculus* lymphocytic

leukemia (L1210, ATCC #CCL-219). Cells were cultured in DMEM, high glucose + GlutaMAX + fetal bovine serum + Pen-Strep (all from Thermo Fisher Scientific). To make droplets, cells were prepared to densities of 2 million cells / mL and emulsified using the Bio-Rad QX200 cartridges (using methods as described in Chapters 2 and 3). To measure apoptosis, we used 5 μM Green Detection Reagent (Thermo Fisher Scientific) added to media. Microwell array chips were incubated at 37C, 5% $CO_2$ in a standard cell culture incubator.

## 5.6.4 Phase contrast imaging and analysis

For phase contrast imaging, we used a Nikon Ti-E inverted microscope with white-light illumination. Images were collected using a CFI Plan Fluor DL 4X objective and Hamamatsu Orca Flash 4.0 camera (no pixel binning, to achieve 1.625 μm / pixel resolution).

To measure cell density in each microwell, we use the following image processing steps. First, we used a high pass filter to amplify the signal, by difference of gaussians (with $\sigma_1 = 0.4$ μm and $\sigma_2 = 1$ μm). Then, we computed a "roughness" metric by convolution of a range filter (maximum-minimum, over a disk, radius = 3.25 μm). The final metric reported is average of the roughness metric over each microwell area (segmented by fluorescence of the encoding dyes).

## 5.6.5 Production of agarose gel beads

To form gel beads we used Ultra-low Gelling Temperature agarose (Sigma Aldrich), as it gels at a temperature below 37C (the maximum temperature we used to culture microbes in this work), but also, after gelling, it will not melt again at the culture temperature, since it exhibits exhibit hysteresis in the liquid-to-gel transition.

To make the agarose beads, we prepared *E. coli* cultures according to the same methods in Chapter 3, and added the culture to molten agarose solution (0.5% w/v; we found that higher concentrations are too viscous to make droplets) heated to 37C. We then made droplets using Bio-Rad QX200 cartridges. To gel the molten agarose, we incubated the droplets at 4C for 1 hour. These emulsified gel beads can then be handled the same as liquid droplets with the same methods used throughout the rest of this thesis.

# References

[1]     S. Brenner, "Life sentences: Detective rummage investigates," *Genome Biol.*, vol. 3, no. 9, p. comment1013-1, 2002.

[2]     C. Darwin, *On the origin of species, 1859*. Routledge, 2004.

[3]     G. Mendel, "Experiments in plant hybridization (1865)," *Verhandlungen des naturforschenden Vereins Brünn.) Available online www. mendelweb. org/Mendel. html (accessed 1 January 2013)*, 1996.

[4]     E. Buchner, "Cell-free fermentation," *Nobel Lect.*, pp. 103–120, 1907.

[5]     C. F. Cori, "James B. Sumner and the chemical nature of enzymes," *Trends Biochem. Sci.*, vol. 6, pp. 194–196, 1981.

[6]     A. D. Hershey and M. Chase, "Independent functions of viral protein and nucleic acid in growth of bacteriophage," in *Die Entdeckung der Doppelhelix*, Springer, 2017, pp. 121–139.

[7]     J. D. Watson and F. H. C. Crick, "Molecular structure of nucleic acids," *Nature*, vol. 171, no. 4356, pp. 737–738, 1953.

[8]     E. M. Lucchetta, J. H. Lee, L. A. Fu, N. H. Patel, and R. F. Ismagilov, "Dynamics of Drosophila embryonic patterning network perturbed in space and time using microfluidics," *Nature*, vol. 434, no. 7037, p. 1134, 2005.

[9]     T. Ahmed, T. S. Shimizu, and R. Stocker, "Microfluidics for bacterial chemotaxis," *Integr. Biol.*, vol. 2, no. 11–12, pp. 604–629, 2010.

[10]    C. S. Chen, M. Mrksich, S. Huang, G. M. Whitesides, and D. E. Ingber, "Geometric control of cell life and death," *Science (80-. ).*, vol. 276, no. 5317, pp. 1425–1428, 1997.

[11]    C. S. Chen, M. Mrksich, S. Huang, G. M. Whitesides, and D. E. Ingber, "Micropatterned surfaces for control of cell shape, position, and function," *Biotechnol. Prog.*, vol. 14, no. 3, pp. 356–363, 1998.

[12]    M. E. Todhunter, N. Y. Jee, A. J. Hughes, M. C. Coyle, A. Cerchiari, J. Farlow, J. C. Garbe, M. A. LaBarge, T. A. Desai, and Z. J. Gartner, "Programmed synthesis of three-dimensional tissues," *Nat. Methods*, vol. 12, no. 10, pp. 975–981, 2015.

[13] D. C. Duffy, J. C. McDonald, O. J. A. Schueller, and G. M. Whitesides, "Rapid prototyping of microfluidic systems in poly (dimethylsiloxane)," *Anal. Chem.*, vol. 70, no. 23, pp. 4974–4984, 1998.

[14] G. M. Whitesides, "The origins and the future of microfluidics," *Nature*, vol. 442, p. 368, Jul. 2006.

[15] S. K. W. Dertinger, D. T. Chiu, N. L. Jeon, and G. M. Whitesides, "Generation of gradients having complex shapes using microfluidic networks," *Anal. Chem.*, vol. 73, no. 6, pp. 1240–1246, 2001.

[16] M. D. Lazova, T. Ahmed, D. Bellomo, R. Stocker, and T. S. Shimizu, "Response rescaling in bacterial chemotaxis," *Proc. Natl. Acad. Sci.*, vol. 108, no. 33, pp. 13870–13875, 2011.

[17] P. C. Blainey, A. M. van Oijen, A. Banerjee, G. L. Verdine, and X. S. Xie, "A base-excision DNA-repair protein finds intrahelical lesion bases by fast sliding in contact with DNA.," *Proc. Natl. Acad. Sci. U. S. A.*, vol. 103, no. 15, pp. 5752–7, 2006.

[18] J. R. Rettig and A. Folch, "Large-scale single-cell trapping and imaging using microwell arrays," *Anal. Chem.*, vol. 77, no. 17, pp. 5628–5634, 2005.

[19] P. Wang, L. Robert, J. Pelletier, W. L. Dang, F. Taddei, A. Wright, and S. Jun, "Robust growth of Escherichia coli," *Curr. Biol.*, vol. 20, no. 12, pp. 1099–1103, 2010.

[20] H. C. Fan, G. K. Fu, and S. P. A. Fodor, "Combinatorial labeling of single cells for gene expression cytometry," *Science (80-. ).*, vol. 347, no. 6222, p. 1258367, 2015.

[21] T. M. Gierahn, M. H. Wadsworth II, T. K. Hughes, B. D. Bryson, A. Butler, R. Satija, S. Fortune, J. C. Love, and A. K. Shalek, "Seq-Well: portable, low-cost RNA sequencing of single cells at high throughput," *Nat. Methods*, vol. 14, no. 4, p. 395, 2017.

[22] M. A. Unger, M. A. Unger, H. Chou, T. Thorsen, A. Scherer, and S. R. Quake, "Monolithic Microfabricated Valves and Pumps by Multilayer Soft Lithography," vol. 288, no. 5463, pp. 113–116, 2000.

[23] T. Thorsen, S. J. Maerkl, and S. R. Quake, "Microfluidic large-scale integration," *Science (80-. ).*, vol. 298, no. 5593, pp. 580–584, 2002.

[24] C. L. Hansen, E. Skordalakes, J. M. Berger, and S. R. Quake, "A robust and scalable microfluidic metering method that allows protein crystal growth by free interface diffusion," *Proc. Natl. Acad.*

*Sci.*, vol. 99, no. 26, pp. 16531–16536, 2002.

[25]    J. Liu, C. Hansen, and S. R. Quake, "Solving the 'world-to-chip' interface problem with a microfluidic matrix," *Anal. Chem.*, vol. 75, no. 18, pp. 4718–4723, 2003.

[26]    J. W. Hong, V. Studer, G. Hang, W. F. Anderson, and S. R. Quake, "A nanoliter-scale nucleic acid processor with parallel architecture," *Nat. Biotechnol.*, vol. 22, no. 4, p. 435, 2004.

[27]    S. Kim, J. De Jonghe, A. B. Kulesa, D. Feldman, T. Vatanen, R. P. Bhattacharyya, B. Berdy, J. Gomez, J. Nolan, S. Epstein, and P. C. Blainey, "High-throughput automated microfluidic sample preparation for accurate microbial genomics," *Nat. Commun.*, vol. 8, p. 13919, 2017.

[28]    R. J. Taylor, D. Falconnet, A. Niemistö, S. A. Ramsey, S. Prinz, I. Shmulevich, T. Galitski, and C. L. Hansen, "Dynamic analysis of MAPK signaling using a high-throughput microfluidic single-cell imaging platform," *Proc. Natl. Acad. Sci.*, vol. 106, no. 10, pp. 3758–3763, 2009.

[29]    T. Thorsen, R. W. Roberts, F. H. Arnold, and S. R. Quake, "Dynamic pattern formation in a vesicle-generating microfluidic device," *Phys. Rev. Lett.*, vol. 86, no. 18, pp. 4163–4166, 2001.

[30]    S. L. Anna, N. Bontoux, and H. A. Stone, "Formation of dispersions using 'flow focusing' in microchannels," *Appl. Phys. Lett.*, vol. 82, no. 3, pp. 364–366, 2003.

[31]    C. A. Lipinski, F. Lombardo, B. W. Dominy, and P. J. Feeney, "Experimental and computational approaches to estimate solubility and permeability in drug discovery and development settings," *Adv. Drug Deliv. Rev.*, vol. 64, pp. 4–17, 2012.

[32]    R. L. Scott, "The Solubility of Fluorocarbons1," *J. Am. Chem. Soc.*, vol. 70, no. 12, pp. 4090–4093, 1948.

[33]    C. Holtze, A. C. Rowat, J. J. Agresti, J. B. Hutchison, F. E. Angilè, C. H. J. Schmitz, S. Köster, H. Duan, K. J. Humphry, R. A. Scanga, J. S. Johnson, D. Pisignano, and D. A. Weitz, "Biocompatible surfactants for water-in-fluorocarbon emulsions," *Lab Chip*, vol. 8, no. 10, p. 1632, 2008.

[34]    X. Niu, S. Gulati, and J. B. Edel, "Pillar-induced droplet merging in microfluidic circuits," *Lab Chip*, vol. 8, no. 11, pp. 1837–1841, 2008.

[35]    M. Pan, F. Lyu, and S. K. Y. Tang, "Methods to coalesce fluorinated Pickering emulsions," *Anal. Methods*, vol. 9, no. 31, pp. 4622–4629, 2017.

[36]    C. N. Baroud, M. R. de Saint Vincent, and J.-P. Delville, "An optical toolbox for total control of

droplet microfluidics," *Lab Chip*, vol. 7, no. 8, pp. 1029–1033, 2007.

[37] M. Sesen, T. Alan, and A. Neild, "Microfluidic on-demand droplet merging using surface acoustic waves," *Lab Chip*, vol. 14, no. 17, pp. 3325–3333, 2014.

[38] I. Akartuna, D. M. Aubrecht, T. E. Kodger, and D. A. Weitz, "Chemically induced coalescence in droplet-based microfluidics," *Lab Chip*, vol. 15, no. 4, pp. 1140–1144, 2015.

[39] K. Ahn, C. Kerbage, T. P. Hunt, R. M. Westervelt, D. R. Link, and D. A. Weitz, "Dielectrophoretic manipulation of drops for high-speed microfluidic sorting devices," *Appl. Phys. Lett.*, vol. 88, no. 2, pp. 1–3, 2006.

[40] T. Franke, A. R. Abate, D. A. Weitz, and A. Wixforth, "Surface acoustic wave (SAW) directed droplet flow in microfluidics for PDMS devices," *Lab Chip*, vol. 9, no. 18, pp. 2625–2627, 2009.

[41] A. R. Abate and D. A. Weitz, "Faster multiple emulsification with drop splitting," *Lab Chip*, vol. 11, no. 11, pp. 1911–1915, 2011.

[42] J. Q. Boedicker, L. Li, T. R. Kline, and R. F. Ismagilov, "Detecting bacteria and determining their susceptibility to antibiotics by stochastic confinement in nanoliter droplets using plug-based microfluidics.," *Lab Chip*, vol. 8, no. 8, pp. 1265–1272, 2008.

[43] O. J. Miller, A. E. Harrak, T. Mangeat, J.-C. Baret, L. Frenz, B. E. Debs, E. Mayot, M. L. Samuels, E. K. Rooney, P. Dieu, M. Galvan, D. R. Link, and A. D. Griffiths, "High-resolution dose-response screening using droplet-based microfluidics," *Proc. Natl. Acad. Sci.*, vol. 109, no. 2, pp. 378–383, 2012.

[44] J. J. Agresti, E. Antipov, A. R. Abate, K. Ahn, A. C. Rowat, J.-C. J.-C. Baret, M. Marquez, A. M. Klibanov, A. D. Griffiths, and D. a. Weitz, "Ultrahigh-throughput screening in drop-based microfluidics for directed evolution," *Proc. Natl. Acad. Sci.*, vol. 107, no. 9, pp. 4004–4009, 2010.

[45] B. L. Wang, A. Ghaderi, H. Zhou, J. Agresti, D. A. Weitz, G. R. Fink, and G. Stephanopoulos, "Microfluidic high-throughput culturing of single cells for selection based on extracellular metabolite production or consumption," *Nat. Biotechnol.*, vol. 32, no. 5, p. 473, 2014.

[46] B. El Debs, R. Utharala, I. V Balyasnikova, A. D. Griffiths, and C. A. Merten, "Functional single-cell hybridoma screening using droplet-based microfluidics," *Proc. Natl. Acad. Sci.*, vol. 109, no. 29, pp. 11570–11575, 2012.

154

[47]  E. Z. Macosko, A. Basu, R. Satija, J. Nemesh, K. Shekhar, M. Goldman, I. Tirosh, A. R. Bialas, N. Kamitaki, E. M. Martersteck, J. J. Trombetta, D. A. Weitz, J. R. Sanes, A. K. Shalek, A. Regev, and S. A. McCarroll, "Highly parallel genome-wide expression profiling of individual cells using nanoliter droplets," *Cell*, vol. 161, no. 5, pp. 1202–1214, 2015.

[48]  E. K. Sackmann, A. L. Fulton, and D. J. Beebe, "The present and future role of microfluidics in biomedical research," *Nature*, vol. 507, no. 7491, pp. 181–189, 2014.

[49]  S. H. Yun, L. M. Cabrera, J. W. Song, N. Futai, Y. C. Tung, G. D. Smith, and S. Takayama, "Characterization and resolution of evaporation-mediated osmolality shifts that constrain microfluidic cell culture in poly(dimethylsiloxane) devices," *Anal. Chem.*, vol. 79, no. 3, pp. 1126–1134, 2007.

[50]  M. W. Toepke and D. J. Beebe, "PDMS absorption of small molecules and consequences in microfluidic applications," *Lab Chip*, vol. 6, no. 12, pp. 1484–1486, 2006.

[51]  K. J. Regehr, M. Domenech, J. T. Koepsel, K. C. Carver, S. J. Ellison-Zelski, W. L. Murphy, L. A. Schuler, E. T. Alarid, and D. J. Beebe, "Biological implications of polydimethylsiloxane-based microfluidic cell culture," *Lab Chip*, vol. 9, no. 15, pp. 2132–2139, 2009.

[52]  E. Brouzes, M. Medkova, N. Savenelli, D. Marran, M. Twardowski, J. B. Hutchison, J. M. Rothberg, D. R. Link, N. Perrimon, and M. L. Samuels, "Droplet microfluidic technology for single-cell high-throughput screening.," *Proc. Natl. Acad. Sci. U. S. A.*, vol. 106, no. 34, pp. 14195–14200, 2009.

[53]  J. C. Baret, Y. Beck, I. Billas-Massobrio, D. Moras, and A. D. Griffiths, "Quantitative cell-based reporter gene assays using droplet-based microfluidics," *Chem. Biol.*, vol. 17, no. 5, pp. 528–536, 2010.

[54]  T. Konry, A. Golberg, and M. Yarmush, "Live single cell functional phenotyping in droplet nano-liter reactors," *Sci. Rep.*, vol. 3, 2013.

[55]  J. Park, A. Kerner, M. A. Burns, and X. N. Lin, "Microdroplet-enabled highly parallel co-cultivation of microbial communities," *PLoS One*, vol. 6, no. 2, p. e17019, 2011.

[56]  M. T. Guo, A. Rotem, J. A. Heyman, and D. A. Weitz, "Droplet microfluidics for high-throughput biological assays," *Lab Chip*, vol. 12, no. 12, p. 2146, 2012.

[57]  L. Mahler, M. Tovar, T. Weber, S. Brandes, M. M. Rudolph, J. Ehgartner, T. Mayr, M. T. Figge, M. Roth, and E. Zang, "Enhanced and homogeneous oxygen availability during incubation of microfluidic droplets," *RSC Adv.*, vol. 5, no. 123, pp. 101871–101878, 2015.

[58]  S. S. Terekhov, I. V Smirnov, A. V Stepanova, T. V Bobik, Y. A. Mokrushina, N. A. Ponomarenko, A. A. Belogurov, M. P. Rubtsova, O. V Kartseva, and M. O. Gomzikova, "Microfluidic droplet platform for ultrahigh-throughput single-cell screening of biodiversity," *Proc. Natl. Acad. Sci.*, p. 201621226, 2017.

[59]  Y. Skhiri, P. Gruner, B. Semin, Q. Brosseau, D. Pekin, L. Mazutis, V. Goust, F. Kleinschmidt, A. El Harrak, J. B. Hutchison, E. Mayot, J.-F. Bartolo, A. D. Griffiths, V. Taly, and J.-C. Baret, "Dynamics of molecular transport by surfactants in emulsions," *Soft Matter*, vol. 8, no. 41, p. 10618, 2012.

[60]  M. Pan, L. Rosenfeld, M. Kim, M. Xu, E. Lin, R. Derda, and S. K. Y. Tang, "Fluorinated pickering emulsions impede interfacial transport and form rigid interface for the growth of anchorage-dependent cells," *ACS Appl. Mater. Interfaces*, vol. 6, no. 23, pp. 21446–21453, 2014.

[61]  J. Clausell-Tormos, D. Lieber, J. C. Baret, A. El-Harrak, O. J. Miller, L. Frenz, J. Blouwolff, K. J. Humphry, S. Köster, H. Duan, C. Holtze, D. A. Weitz, A. D. Griffiths, and C. A. Merten, "Droplet-Based Microfluidic Platforms for the Encapsulation and Screening of Mammalian Cells and Multicellular Organisms," *Chem. Biol.*, vol. 15, no. 5, pp. 427–437, 2008.

[62]  L. Baraban, F. Bertholle, M. L. M. Salverda, N. Bremond, P. Panizza, J. Baudry, J. A. G. M. de Visser, and J. Bibette, "Millifluidic droplet analyser for microbiology," *Lab Chip*, vol. 11, no. 23, p. 4057, 2011.

[63]  D. S. Kong, T. A. Thorsen, J. Babb, S. T. Wick, J. J. Gam, R. Weiss, and P. A. Carr, "Open-source, community-driven microfluidics with Metafluidics," *Nat. Biotechnol.*, vol. 35, no. 6, p. 523, 2017.

[64]  S. L. Schreiber, "Target-oriented and diversity-oriented organic synthesis in drug discovery," *Science (80-. ).*, vol. 287, no. 5460, pp. 1964–1969, 2000.

[65]  R. B. Merrifield, "Solid phase peptide synthesis. I. The synthesis of a tetrapeptide," *J. Am. Chem. Soc.*, vol. 85, no. 14, pp. 2149–2154, 1963.

[66]  A. S. L. Wong, G. C. G. Choi, A. A. Cheng, O. Purcell, and T. K. Lu, "Massively parallel high-

order combinatorial genetics in human cells," *Nat. Biotechnol.*, vol. 33, no. 9, p. 952, 2015.

[67]    E. Weber, C. Engler, R. Gruetzner, S. Werner, and S. Marillonnet, "A modular cloning system for standardized assembly of multigene constructs," *PLoS One*, vol. 6, no. 2, p. e16765, 2011.

[68]    A. Kulesa, J. Kehe, J. E. Hurtado, P. Tawde, and P. C. Blainey, "Combinatorial drug discovery in nanoliter droplets.," *Proc. Natl. Acad. Sci. U. S. A.*, p. 201802233, 2018.

[69]    J. B. Fitzgerald, B. Schoeberl, U. B. Nielsen, and P. K. Sorger, "Systems biology and combination therapy in the quest for clinical efficacy," *Nat. Chem. Biol.*, vol. 2, no. 9, pp. 458–466, 2006.

[70]    A. L. Hopkins, "Network pharmacology: the next paradigm in drug discovery," *Nat. Chem. Biol.*, vol. 4, no. 11, pp. 682–690, 2008.

[71]    C. T. Keith, A. A. Borisy, and B. R. Stockwell, "Multicomponent therapeutics for networked systems.," *Nat. Rev. Drug Discov.*, vol. 4, no. 1, pp. 71–78, 2005.

[72]    T. Roemer and C. Boone, "Systems-level antimicrobial drug and drug synergy discovery," *Nat. Chem. Biol.*, vol. 9, no. 4, pp. 222–231, 2013.

[73]    J. Lehár, A. S. Krueger, W. Avery, A. M. Heilbut, L. M. Johansen, E. R. Price, R. J. Rickles, G. F. Short III, J. E. Staunton, X. Jin, M. S. Lee, G. R. Zimmermann, and A. A. Borisy, "Synergistic drug combinations tend to improve therapeutically relevant selectivity," *Nat. Biotechnol.*, vol. 27, no. 7, pp. 659–666, 2009.

[74]    X. Sun, S. Vilar, and N. P. Tatonetti, "High-throughput methods for combinatorial drug discovery.," *Sci. Transl. Med.*, vol. 5, no. 205, p. 205rv1, 2013.

[75]    B. Momeni, L. Xie, and W. Shou, "Lotka-Volterra pairwise modeling fails to capture diverse pairwise microbial interactions," *Elife*, vol. 6, 2017.

[76]    S. Mitri and K. Richard Foster, "The genotypic view of social interactions in microbial communities," *Annu. Rev. Genet.*, vol. 47, pp. 247–273, 2013.

[77]    A. Konopka, S. Lindemann, and J. Fredrickson, "Dynamics in microbial communities: unraveling mechanisms to identify principles," *ISME J.*, vol. 9, no. 7, p. 1488, 2015.

[78]    M. M. Mayfield and D. B. Stouffer, "Higher-order interactions capture unexplained complexity in diverse communities," *Nat. Ecol. Evol.*, vol. 1, no. 3, p. 62, 2017.

[79]    M. Zagnoni and J. M. Cooper, "On-chip electrocoalescence of microdroplets as a function of

voltage, frequency and droplet size," *Lab Chip*, vol. 9, no. 18, p. 2652, 2009.

[80] P. Gruner, B. Riechers, B. Semin, J. Lim, A. Johnston, K. Short, J.-C. Baret, K. S. & P. Gruner, B. Riechers, B. Semin, J. Lim, A. Johnston, and JC. Baret, "Controlling molecular transport in minimal emulsions," *Nat. Commun.*, vol. 7, p. 9, 2016.

[81] P. Abbyad, R. Dangla, A. Alexandrou, and C. N. Baroud, "Rails and anchors: guiding and trapping droplet microreactors in two dimensions," *Lab Chip*, vol. 11, no. 5, pp. 813–821, 2011.

[82] E. Fradet, P. Abbyad, M. H. Vos, and C. N. Baroud, "Parallel measurements of reaction kinetics using ultralow-volumes," *Lab Chip*, vol. 13, no. 22, pp. 4326–4330, 2013.

[83] L. Mazutis, J. Gilbert, W. L. Ung, D. A. Weitz, A. D. Griffiths, and J. A. Heyman, "Single-cell analysis and sorting using droplet-based microfluidics," *Nat. Protoc.*, vol. 8, no. 5, p. 870, 2013.

[84] K. Strebhardt and A. Ullrich, "Paul Ehrlich's magic bullet concept: 100 years of progress," *Nat. Rev. Cancer*, vol. 8, no. 6, pp. 473–480, 2008.

[85] L. L. Silver, "Challenges of antibacterial discovery.," *Clin. Microbiol. Rev.*, vol. 24, no. 1, pp. 71–109, 2011.

[86] A. A. Borisy, P. J. Elliott, N. W. Hurst, M. S. Lee, J. Lehar, E. R. Price, G. Serbedzija, G. R. Zimmermann, M. A. Foley, B. R. Stockwell, and C. T. Keith, "Systematic discovery of multicomponent therapeutics," *Proc. Natl. Acad. Sci.*, vol. 100, no. 13, pp. 7977–7982, 2003.

[87] X. Tan, L. Hu, L. J. Luquette, G. Gao, Y. Liu, H. Qu, R. Xi, Z. J. Lu, P. J. Park, and S. J. Elledge, "Systematic identification of synergistic drug pairs targeting HIV," *Nat. Biotechnol.*, vol. 30, no. 11, pp. 1125–1130, 2012.

[88] B. Severyn, R. A. Liehr, A. Wolicki, K. H. Nguyen, E. M. Hudak, M. Ferrer, J. S. Caldwell, J. D. Hermes, J. Li, and M. Tudor, "Parsimonious discovery of synergistic drug combinations," *ACS Chem. Biol.*, vol. 6, no. 12, pp. 1391–8, 2011.

[89] K. Churski, T. S. Kaminski, S. Jakiela, W. Kamysz, W. Baranska-Rybak, D. B. Weibel, and P. Garstecki, "Rapid screening of antibiotic toxicity in an automated microdroplet system," *Lab Chip*, vol. 12, no. 9, p. 1629, 2012.

[90] G. MacBeath, A. N. Koehler, and S. L. Schreiber, "Printing small molecules as microarrays and detecting protein-ligand interactions en masse [19]," *Journal of the American Chemical Society*,

158

vol. 121, no. 34. pp. 7967–7968, 1999.

[91] D. N. Gosalia and S. L. Diamond, "Printing chemical libraries on microarrays for fluid phase nanoliter reactions.," *Proc. Natl. Acad. Sci. U. S. A.*, vol. 100, no. 15, pp. 8721–8726, 2003.

[92] R. F. Ismagilov, J. M. K. Ng, P. J. A. Kenis, and G. M. Whitesides, "Microfluidic arrays of fluid-fluid diffusional contacts as detection elements and combinatorial tools," *Anal. Chem.*, vol. 73, no. 21, pp. 5207–5213, 2001.

[93] E. Fradet, C. Bayer, F. Hollfelder, and C. N. Baroud, "Measuring Fast and Slow Enzyme Kinetics in Stationary Droplets," *Anal. Chem.*, vol. 87, no. 23, pp. 11915–11922, 2015.

[94] G. Woronoff, A. El Harrak, E. Mayot, O. Schicke, O. J. Miller, P. Soumillion, A. D. Griffiths, and M. Ryckelynck, "New generation of amino coumarin methyl sulfonate-based fluorogenic substrates for amidase assays in droplet-based microfluidic applications," *Anal. Chem.*, vol. 83, no. 8, pp. 2852–2857, 2011.

[95] C. I. Bliss, "The calculation of microbial assays," *Bacteriol Rev*, vol. 20, no. 4, pp. 243–258, 1956.

[96] F. C. Odds, "Synergy, antagonism, and what the chequerboard puts between them," *J. Antimicrob. Chemother.*, vol. 52, no. 1, pp. 1–1, 2003.

[97] D. J. Payne, M. N. Gwynn, D. J. Holmes, and D. L. Pompliano, "Drugs for bad bugs: confronting the challenges of antibacterial discovery.," *Nat. Rev. Drug Discov.*, vol. 6, no. 1, pp. 29–40, 2007.

[98] R. Tommasi, D. G. Brown, G. K. Walkup, J. I. Manchester, and A. A. Miller, "ESKAPEing the labyrinth of antibacterial discovery," *Nat. Rev. Drug Discov.*, vol. 14, no. 8, pp. 529–542, 2015.

[99] L. Ejim, M. A. Farha, S. B. Falconer, J. Wildenhain, B. K. Coombes, M. Tyers, E. D. Brown, and G. D. Wright, "Combinations of antibiotics and nonantibiotic drugs enhance antimicrobial efficacy," *Nat. Chem. Biol.*, vol. 7, no. 6, pp. 348–350, 2011.

[100] M. A. Farha and E. D. Brown, "Chemical probes of escherichia coli uncovered through chemical-chemical interaction profiling with compounds of known biological activity," *Chem. Biol.*, vol. 17, no. 8, pp. 852–862, 2010.

[101] J. M. Stokes, C. R. MacNair, B. Ilyas, S. French, J.-P. Côté, C. Bouwman, M. A. Farha, A. O. Sieron, C. Whitfield, B. K. Coombes, and E. D. Brown, "Pentamidine sensitizes Gram-negative pathogens to antibiotics and overcomes acquired colistin resistance," *Nat. Microbiol.*, vol. 2, p.

17028, 2017.

[102] S. M. Corsello, J. A. Bittker, Z. Liu, J. Gould, P. McCarren, J. E. Hirschman, S. E. Johnston, A. Vrcic, B. Wong, M. Khan, J. Asiedu, R. Narayan, C. C. Mader, A. Subramanian, and T. R. Golub, "The Drug Repurposing Hub: a next-generation drug library and information resource," *Nat. Med.*, vol. 23, no. 4, pp. 405–408, 2017.

[103] T. T. Ashburn and K. B. Thor, "Drug repositioning: identifying and developing new uses for existing drugs," *Nat. Rev. Drug Discov.*, vol. 3, no. 8, pp. 673–683, 2004.

[104] S. M. Corsello, J. A. Bittker, Z. Liu, J. Gould, P. McCarren, J. E. Hirschman, S. E. Johnston, A. Vrcic, B. Wong, M. Khan, J. Asiedu, R. Narayan, C. C. Mader, A. Subramanian, and T. R. Golub, "The Drug Repurposing Hub: a next-generation drug library and information resource," *Nat. Med.*, vol. 23, no. 4, pp. 405–408, 2017.

[105] J. Zhang, T. Chung, and K. Oldenburg, "A Simple Statistical Parameter for Use in Evaluation and Validation of High Throughput Screening Assays," *J. Biomol. Screen.*, vol. 4, no. 2, pp. 67–73, 1999.

[106] J. J. Filliben, "The probability plot correlation coefficient test for normality," *Technometrics*, vol. 17, no. 1, pp. 111–117, 1975.

[107] L. M. Higgins, J. Friedman, H. Shen, and J. Gore, "Co-occurring soil bacteria exhibit a robust competitive hierarchy and lack of non-transitive interactions," *bioRxiv*, p. 175737, 2017.

[108] J. K. Fredrickson, "Ecological communities by design," *Science (80-. ).*, vol. 348, no. 6242, pp. 1425–1427, 2015.

[109] S. G. Hays, W. G. Patrick, M. Ziesack, N. Oxman, and P. A. Silver, "Better together: engineering and application of microbial symbioses," *Curr. Opin. Biotechnol.*, vol. 36, pp. 40–49, 2015.

[110] M. Cavaliere, S. Feng, O. S. Soyer, and J. I. Jiménez, "Cooperation in microbial communities and their biotechnological applications," *Environ. Microbiol.*, vol. 19, no. 8, pp. 2949–2963, 2017.

[111] S. R. Lindemann, H. C. Bernstein, H.-S. Song, J. K. Fredrickson, M. W. Fields, W. Shou, D. R. Johnson, and A. S. Beliaev, "Engineering microbial consortia for controllable outputs," *ISME J.*, vol. 10, no. 9, p. 2077, 2016.

[112] M. R. Seyedsayamdost, M. F. Traxler, J. Clardy, and R. Kolter, "Old meets new: using

interspecies interactions to detect secondary metabolite production in actinomycetes," in *Methods in enzymology*, vol. 517, Elsevier, 2012, pp. 89–109.

[113] J. J. Minty, M. E. Singer, S. A. Scholz, C.-H. Bae, J.-H. Ahn, C. E. Foster, J. C. Liao, and X. N. Lin, "Design and characterization of synthetic fungal-bacterial consortia for direct production of isobutanol from cellulosic biomass," *Proc. Natl. Acad. Sci.*, vol. 110, no. 36, pp. 14592–14597, 2013.

[114] T. R. Zuroff, S. B. Xiques, and W. R. Curtis, "Consortia-mediated bioprocessing of cellulose to ethanol with a symbiotic Clostridium phytofermentans/yeast co-culture," *Biotechnol. Biofuels*, vol. 6, no. 1, p. 59, 2013.

[115] K. Zhou, K. Qiao, S. Edgar, and G. Stephanopoulos, "Distributing a metabolic pathway among a microbial consortium enhances production of natural products," *Nat. Biotechnol.*, vol. 33, no. 4, p. 377, 2015.

[116] L. Li, C. Yang, W. Lan, S. Xie, C. Qiao, and J. Liu, "Removal of methyl parathion from artificial off-gas using a bioreactor containing a constructed microbial consortium," *Environ. Sci. Technol.*, vol. 42, no. 6, pp. 2136–2141, 2008.

[117] H. Zhang, C. Yang, C. Li, L. Li, Q. Zhao, and C. Qiao, "Functional assembly of a microbial consortium with autofluorescent and mineralizing activity for the biodegradation of organophosphates," *J. Agric. Food Chem.*, vol. 56, no. 17, pp. 7897–7902, 2008.

[118] T. D. Lawley, S. Clare, A. W. Walker, M. D. Stares, T. R. Connor, C. Raisen, D. Goulding, R. Rad, F. Schreiber, and C. Brandt, "Targeted restoration of the intestinal microbiota with a simple, defined bacteriotherapy resolves relapsing Clostridium difficile disease in mice," *PLoS Pathog.*, vol. 8, no. 10, p. e1002995, 2012.

[119] S. Brugiroux, M. Beutler, C. Pfann, D. Garzetti, H.-J. Ruscheweyh, D. Ring, M. Diehl, S. Herp, Y. Lötscher, and S. Hussain, "Genome-guided design of a defined mouse microbiota that confers colonization resistance against Salmonella enterica serovar Typhimurium," *Nat. Microbiol.*, vol. 2, no. 2, p. 16215, 2017.

[120] S. Caballero, S. Kim, R. A. Carter, I. M. Leiner, B. Sušac, L. Miller, G. J. Kim, L. Ling, and E. G. Pamer, "Cooperating commensals restore colonization resistance to vancomycin-resistant Enterococcus faecium," *Cell Host Microbe*, vol. 21, no. 5, pp. 592–602, 2017.

[121] J. Shong, M. R. J. Diaz, and C. H. Collins, "Towards synthetic microbial consortia for bioprocessing," *Curr. Opin. Biotechnol.*, vol. 23, no. 5, pp. 798–802, 2012.

[122] W. R. Harcombe, W. J. Riehl, I. Dukovski, B. R. Granger, A. Betts, A. H. Lang, G. Bonilla, A. Kar, N. Leiby, and P. Mehta, "Metabolic resource allocation in individual microbes determines ecosystem interactions and spatial dynamics," *Cell Rep.*, vol. 7, no. 4, pp. 1104–1115, 2014.

[123] A. R. Zomorrodi and D. Segrè, "Synthetic ecology of microbes: mathematical models and applications," *J. Mol. Biol.*, vol. 428, no. 5, pp. 837–861, 2016.

[124] M. Embree, J. K. Liu, M. M. Al-Bassam, and K. Zengler, "Networks of energetic and metabolic interactions define dynamics in microbial communities," *Proc. Natl. Acad. Sci.*, vol. 112, no. 50, pp. 15450–15455, 2015.

[125] J. Friedman, L. M. Higgins, and J. Gore, "Community structure follows simple assembly rules in microbial microcosms," *Nat. Ecol. Evol.*, vol. 1, no. 5, p. 109, 2017.

[126] O. X. Cordero, H. Wildschutte, B. Kirkup, S. Proehl, L. Ngo, F. Hussain, F. Le Roux, T. Mincer, and M. F. Polz, "Ecological populations of bacteria act as socially cohesive units of antibiotic production and resistance," *Science (80-. ).*, vol. 337, no. 6099, pp. 1228–1231, 2012.

[127] K. R. Foster and T. Bell, "Competition, not cooperation, dominates interactions among culturable microbial species," *Curr. Biol.*, vol. 22, no. 19, pp. 1845–1850, 2012.

[128] K. Vetsigian, R. Jajoo, and R. Kishony, "Structure and evolution of Streptomyces interaction networks in soil and in silico," *PLoS Biol.*, vol. 9, no. 10, p. e1001184, 2011.

[129] R. R. H. Hansen, A. C. Timm, C. M. Timm, A. N. Bible, J. L. Morrell-Falvey, D. A. Pelletier, M. L. Simpson, M. J. Doktycz, and S. T. Retterer, "Stochastic assembly of bacteria in microwell arrays reveals the importance of confinement in community development," *PLoS One*, vol. 11, no. 5, p. e0155080, 2016.

[130] C. J. Ingham, A. Sprenkels, J. Bomer, D. Molenaar, A. van den Berg, J. E. T. van Hylckama Vlieg, and W. M. de Vos, "The micro-Petri dish, a million-well growth chip for the culture and high-throughput screening of microorganisms," *Proc. Natl. Acad. Sci.*, vol. 104, no. 46, pp. 18217–18222, 2007.

[131] M. Rothballer, B. Eckert, M. Schmid, A. Fekete, M. Schloter, A. Lehner, S. Pollmann, and A.

Hartmann, "Endophytic root colonization of gramineous plants by Herbaspirillum frisingense," *FEMS Microbiol. Ecol.*, vol. 66, no. 1, pp. 85–95, 2008.

[132] X. Yu, S. P. Lund, R. A. Scott, J. W. Greenwald, A. H. Records, D. Nettleton, S. E. Lindow, D. C. Gross, and G. A. Beattie, "Transcriptional responses of Pseudomonas syringae to growth in epiphytic versus apoplastic leaf sites," *Proc. Natl. Acad. Sci.*, vol. 110, no. 5, pp. E425–E434, 2013.

[133] J. E. Goldford, N. Lu, D. Bajic, S. Estrela, M. Tikhonov, A. Sanchez-Gorostiaga, D. Segre, P. Mehta, and A. Sanchez, "Emergent simplicity in microbial community assembly," *bioRxiv*, p. 205831, 2017.

[134] T. A. Hoek, K. Axelrod, T. Biancalani, E. A. Yurtsev, J. Liu, and J. Gore, "Resource availability modulates the cooperative and competitive nature of a microbial cross-feeding mutualism," *PLoS Biol.*, vol. 14, no. 8, p. e1002540, 2016.

[135] S. N. Rampersad, "Multiple applications of alamar blue as an indicator of metabolic function and cellular health in cell viability bioassays," *Sensors (Switzerland)*, vol. 12, no. 9, pp. 12347–12360, 2012.

[136] J. Heinemann, K. Deng, S. C. C. Shih, J. Gao, P. D. Adams, A. K. Singh, and T. R. Northen, "On-chip integration of droplet microfluidics and nanostructure-initiator mass spectrometry for enzyme screening," *Lab Chip*, vol. 17, no. 2, pp. 323–331, 2017.

[137] A. G. Beyene, G. S. Demirer, and M. P. Landry, "Nanoparticle-Templated Molecular Recognition Platforms for Detection of Biological Analytes," *Curr. Protoc. Chem. Biol.*, pp. 197–223, 2016.

[138] H. Ma and J. D. Bryers, "Non-invasive determination of conjugative transfer of plasmids bearing antibiotic-resistance genes in biofilm-bound bacteria: effects of substrate loading and antibiotic selection," *Appl. Microbiol. Biotechnol.*, vol. 97, no. 1, pp. 317–328, 2013.

[139] K. Li, D. Precup, and T. J. Perkins, "Pooled Screening for Synergistic Interactions Subject to Blocking and Noise," *PLoS One*, vol. 9, no. 1, p. e85864, 2014.

[140] Y.-J. J. Eun, A. S. Utada, M. F. Copeland, S. Takeuchi, D. B. Weibel, R. R. H. Hansen, A. C. Timm, C. M. Timm, A. N. Bible, J. L. Morrell-Falvey, D. A. Pelletier, M. L. Simpson, M. J. Doktycz, and S. T. Retterer, "Encapsulating bacteria in agarose microparticles using microfluidics for high-throughput cell analysis and isolation," *ACS Chem. Biol.*, vol. 6, no. 3, pp. 260–266,

2010.

[141]  G. M. Whitesides and B. Grzybowski, "Self-Assembly at All Scales," *Science (80-. ).*, vol. 295, no. 5564, p. 2418 LP-2421, Mar. 2002.

[142]  C. J. Morris, S. A. Stauth, and B. A. Parviz, "Self-assembly for microscale and nanoscale packaging: Steps toward self-packaging," *IEEE Trans. Adv. Packag.*, vol. 28, no. 4, pp. 600–611, 2005.

[143]  H. O. Jacobs, A. R. Tao, A. Schwartz, D. H. Gracias, and G. M. Whitesides, "Fabrication of a cylindrical display by patterned assembly," *Science (80-. ).*, vol. 296, no. 5566, pp. 323–325, 2002.

[144]  D. Dendukuri, S. S. Gu, D. C. Pregibon, T. A. Hatton, and P. S. Doyle, "Stop-flow lithography in a microfluidic device," *Lab Chip*, vol. 7, no. 7, pp. 818–828, 2007.

[145]  H. C. Shum, A. R. Abate, D. Lee, A. R. Studart, B. Wang, C. H. Chen, J. Thiele, R. K. Shah, A. Krummel, and D. A. Weitz, "Droplet microfluidics for fabrication of non-spherical particles," *Macromol. Rapid Commun.*, vol. 31, no. 2, pp. 108–118, 2010.

[146]  J. J. Kim, K. W. Bong, E. Reátegui, D. Irimia, and P. S. Doyle, "Porous microwells for geometry-selective, large-scale microparticle arrays," *Nat. Mater.*, vol. 16, no. 1, pp. 139–146, 2017.

[147]  S. E. Chung, W. Park, S. Shin, S. A. Lee, and S. Kwon, "Guided and fluidic self-assembly of microstructures using railed microfluidicchannels," *Nat. Mater.*, vol. 7, no. 7, pp. 581–587, 2008.

[148]  Z. J. Gartner and C. R. Bertozzi, "Programmed assembly of 3-dimensional microtissues," no. 17, pp. 1–5, 2009.

[149]  C. Y. Li, D. K. Wood, C. M. Hsu, and S. N. Bhatia, "DNA-templated assembly of droplet-derived PEG microtissues," *Lab Chip*, vol. 11, no. 17, p. 2967, 2011.

[150]  M. Hadorn, E. Boenzli, K. T. Sørensen, H. Fellermann, P. Eggenberger Hotz, and M. M. Hanczyc, "Specific and reversible DNA-directed self-assembly of oil-in-water emulsion droplets," *Proc. Natl. Acad. Sci.*, vol. 109, no. 50, p. 20320 LP-20325, Dec. 2012.

[151]  L. Feng, L.-L. Pontani, R. Dreyfus, P. Chaikin, and J. Brujic, "Specificity, flexibility and valence of DNA bonds guide emulsion architecture," *Soft Matter*, vol. 9, no. 41, pp. 9816–9823, 2013.

[152]  D. Y. Zhang and E. Winfree, "Control of DNA strand displacement kinetics using toehold exchange," *J. Am. Chem. Soc.*, vol. 131, no. 47, pp. 17303–17314, 2009.